Hydrodynamics, Mass Transfer and Phase Transition in Bubbly Flows

Citation for published version (APA):
Battistella, A. (2021). *Hydrodynamics, Mass Transfer and Phase Transition in Bubbly Flows*. [Phd Thesis 1 (Research TU/e / Graduation TU/e), Chemical Engineering and Chemistry]. Technische Universiteit Eindhoven.

Document status and date:
Published: 04/11/2021

Document Version:
Publisher's PDF, also known as Version of Record (includes final page, issue and volume numbers)

Please check the document version of this publication:

• A submitted manuscript is the version of the article upon submission and before peer-review. There can be important differences between the submitted version and the official published version of record. People interested in the research are advised to contact the author for the final version of the publication, or visit the DOI to the publisher's website.
• The final author version and the galley proof are versions of the publication after peer review.
• The final published version features the final layout of the paper including the volume, issue and page numbers.

Link to publication

General rights
Copyright and moral rights for the publications made accessible in the public portal are retained by the authors and/or other copyright owners and it is a condition of accessing publications that users recognise and abide by the legal requirements associated with these rights.

- Users may download and print one copy of any publication from the public portal for the purpose of private study or research.
- You may not further distribute the material or use it for any profit-making activity or commercial gain
- You may freely distribute the URL identifying the publication in the public portal.

If the publication is distributed under the terms of Article 25fa of the Dutch Copyright Act, indicated by the "Taverne" license above, please follow below link for the End User Agreement:

www.tue.nl/taverne

Take down policy
If you believe that this document breaches copyright please contact us at:

openaccess@tue.nl

providing details and we will investigate your claim.

Download date: 04. Oct. 2023

HYDRODYNAMICS, MASS TRANSFER AND PHASE TRANSITION IN BUBBLY FLOWS

PROEFSCHRIFT

ter verkrijging van de graad van doctor aan de Technische Universiteit
Eindhoven, op gezag van de rector magnificus, prof.dr.ir. F.P.T. Baaijens,
voor een commissie aangewezen door het College voor Promoties, in het
openbaar te verdedigen op donderdag 4 november 2021 om 16.00 uur

door

Alessandro Battistella

geboren te Merate, Italië

Dit proefschrift is goedgekeurd door de promotoren en de samenstelling van de promotie commissie is als volgt:

voorzitter:	prof.dr.ir. F. Gallucci	
promotor:	prof.dr.ir. M. van Sint Annaland	
copromotor:	dr.ir. I. Roghair	
leden:	prof.dr.-Ing. M. Sommerfeld	Otto von Guericke University of Magdeburg
	prof.dr.ir N.G. Deen	
	prof.dr. D. Marchisio	Politecnico di Torino
	prof.dr. R.M. van der Meer	Universiteit Twente
	dr.ir. C. Haringa	Technische Universiteit Delft

Het onderzoek dat in dit proefschrift wordt beschreven is uitgevoerd in overeenstemming met de TU/e Gedragscode Wetenschapsbeoefening.

This work is part of the Industrial Partnership Programme i36 Dense Bubbly Flows that is carried out under an agreement between Akzo Nobel Chemicals International B.V., DSM Innovation Center B.V., Sabic Global Technologies B.V., Shell Global Solutions B.V., Tata Steel Nederland Technology B.V. and the Netherlands Organisation for Scientific Research (NWO).

Nederlandse titel: “Hydrodynamica, massaoverdracht en faseovergang in bellenstromen.”

Printed by: Gildeprint Drukkerijen, Enschede

Typeset using LaTeX

A catalogue record is available from the Eindhoven University of Technology Library
ISBN: 978-90-386-5398-3
Author email: `alessandro.battistella@yahoo.com`

Front cover designed by Caterina Zen

A papá,

TABLE OF CONTENTS

SUMMARY

Hydrodynamics, Mass Transfer and Phase Transition in Bubbly Flows

Bubbly flows are present ubiquitously in everyday life: everyone has experienced the formation of bubbles when opening alcoholic beverages such as beer or Champagne wine or carbonated drinks as soda. Many applications of bubbly flows can be found in industry, where bubble column reactors are used for, for example, Fischer-Tropsch synthesis, hydrogenations and oxidations. Moreover, bubbles can be found on the electrodes of electrolytic processes or injected in fermentors to supply oxygen to the microbial cells responsible for the production of antibiotics, bioethanol or for wastewater treatment.

Although simple to visualize, bubbly flows are challenging to understand at a fundamental level due to the complex interactions between a large number of relevant physical and chemical phenomena happing at different length scales. On the other hand, fundamental knowledge is required in order to better understand, model, design and optimize processes where bubbles are present. For instance, detailed knowledge on bubble sizes (and distribution) is important in order to improve the mass and heat transfer characteristics and bubble residence time (distribution) and determine the yield of processes which use gas as a reactant. Another example is represented by the unwanted hindering of the surface when gas bubbles form on the electrodes of electrolytic processes: a rapid removal of bubbles ensures that an optimal electrode surface area is exposed for the reaction.

Traditionally, empirical correlations obtained from experimental observations are employed in order to capture the relevant physics: it is common to find correlations for the drag coefficient of rising bubbles or for their formation (nucleation) rates on a surface. In recent years, Computational Fluid Dynamics (CFD) has attracted much attention as a tool to simulate complex bubbly flows and gain fundamental knowledge, at different scales. A multi-scale approach has shown the potential of capturing the detailed physics of bubbly flows with lower-scale detailed models and implement these in larger-scale coarser models. From the range of different types of CFD models that have been developed for multiphase gas-liquid flows, Euler-Lagrange models are particularly suited to gain insights on bubble motion at relatively large scales. In Euler-Lagrange models, each bubble is tracked individually with Newton's laws of motion while accounting for bubble encounters deterministically and using empirical closure relations to take sub-grid phenomena into account.

Despite the great results of Euler-Lagrange models to this day, several challenges are still left to engage. Three particular gaps are identified in this thesis and solutions towards bridging these gaps are proposed and demonstrated: i) the non-Newtonian rheology of the fluid phase when dealing with complex fluids, as for instance in a fermentor, is often neglected; ii) the influence of the free surface on bubbly flows is often approximated with fictitious or diffused boundary conditions; iii) the formation of bubbles as a consequence of local supersaturation effects is usually included with an empirical nucleation rate.

The first step addressed in this thesis is the inclusion of a complex fluid rheology rather than Newtonian. Indeed, in many industrial applications, often the liquid exhibits non-Newtonian behaviour. Such behaviour has an influence not only on the apparent liquid viscosity, but also on the bubble shape and terminal rise velocity, influencing the bubble drag coefficient and thus residence time. For Euler-Lagrange models, accurate closures for the drag force are of utmost importance for an accurate prediction of the behaviour of the bubbles. General drag closures for (deformable) bubbles rising in non-Newtonian liquids are not available in the literature. Therefore, Direct Numerical Simulations (DNS) using a Front-Tracking model have been carried out to study the behaviour of single bubbles rising in a wide range of power-law non-Newtonian fluids. The simulations show that the power-law rheology of the fluid alters the bubble shape, rising pattern and terminal velocity as a consequence of the developed apparent viscosity profiles. Indeed, the results show that large non-spherical bubbles become more spherical in shear-thickening fluids and rise in a straight pattern rather than in a meandering motion. Moreover, the computational results demonstrate that excellent predictions of the bubble rise velocity in non-Newtonian fluids can be obtained by applying existing drag coefficient correlations that were originally derived for Newtonian fluids when using a generalized Reynolds number, thus accounting for the power-law rheology, within 20% accuracy in most cases, for realistic viscosity (shear) parameters.

For the second gap, the Euler-Lagrange Discrete Bubble Model (DBM) is extended to account for the presence of a top free gas-liquid surface. A novel approach is employed, modeling the free surface with a dedicated Front-Tracking technique with special care to the numerical implementation of the sharp interface (hybrid DBM-FT model). This technique allows bubbles to rise till they touch the free surface, which alleviates the necessity to remove bubbles at several Eulerian grid cells distance from the free surface as required by other implementations reported in the literature. A special treatment of the fluid density is necessary to maintain stability: instead of using linear interpolation the density is calculated at the cell faces by shifting the reference frame for the calculation of the phase fraction, thus calculating it exactly also for the staggered grids used to solve the momentum equations. The novel hybrid DBM-FT model has been thoroughly validated with benchmark cases, showing excellent stability even at high surface deformations, and a good agreement with synthetic cases and with experimental results. The DBM-FT model has then been used to investigate the effect of the free surface: a detailed description of the top gas-liquid interface has been shown to be necessary to accurately estimate bubble breakage rates close to the free surface by avoiding excessive shear at the free interface resulting from the often applied artificial boundary condition used to mimic the free surface. On the other hand, the effect of the free surface for the experimental case under consideration is limited to the vicinity of the surface.

The third piece missing in Euler-Lagrange models is the modeling of the formation of bubbles through the process of heterogeneous nucleation. Phase transition occurs often when a gas-forming reaction is present. An important example is represented by electrolytic processes: gas is formed as a consequence of the reaction and bubbles grow on the surface of the electrodes. To account for this phenomenon, the DBM has been expanded with an innovative detailed heterogeneous bubble nucleation algorithm, which accounts for bubbles formation on Lagrangian nucleation sites, initialized as conical cavities, as a consequence of supersaturation. The model accounts for the nucleation, growth and detachment of gas bubbles, as for instance required for the modeling of CO_2 bubbles forming during the fermentation process. The model results show a clear first wave of growing bubbles attached to the nucleation surface, with the formation of a depletion layer. With the continuation of the nucleation process, the bubble size distribution widens and flattens as soon as the bubbles start detaching, and grow and coalesce with each other while rising in the column. The number of bubbles is clearly increased at higher supersaturations, associated with faster bubble growth. To conclude, a sensitivity analysis shows that the density of nucleation sites influences the number of bubbles and the bubble size distribution: fewer nucleation sites result in fewer bubbles, reducing the mixing of the system and slowing the phase transition process. Additionally, decreasing the radius of the nucleation sites leads to an increase in the number of bubbles as a consequence of the smaller bubble detachment radius.

A dedicated experimental setup has been constructed to measure the influence of the supersaturation and the surface properties of a solid substrate on the overall heterogeneous bubble nucleation rates. The experimental setup consists of two interconnected tanks, where CO_2 is first dissolved in water under pressure in one tank and the resulting solution is consequently depressurized in a controlled manner, generating a supersaturated liquid, in order to allow bubble formation on a selected substrate. A similar procedure for single or very few bubbles, was already reported in the literature and has been extended in this study to measure the formation and growth of a relatively large number of bubbles. A dedicated Digital Image Analysis technique is presented and validated, in order to detect the experimental images of growing bubbles attached to the steel substrate. A clear wave is initially visible from the experiments, with bubbles growing together attached to the surface, but as time proceeds the distribution widens and flattens and fewer bubbles nucleate. This is found to be associated to local differences in the mass transfer rates due to competition between bubbles and (local) depletion effects. The correct theoretical dependency on the square root of time is retained but with a much lower mass transfer coefficient than expected. The results from the experiments have been compared with the nucleation model developed in this thesis, and it has been shown that the model is able to qualitatively predict the experimental bubble size distribution with a limited influence of surface properties other than the site radius, which determines the detachment radius. In order to capture the widening and flattening of the distribution, a variance of the Sherwood number between different sites (meaning each site experiences a different mass transfer coefficient) is required in order to mimic depletion/competition effects slowing the growth of some of the bubbles. It is also observed that the total number of bubbles reduces over time: many nucleation sites after a bubble is detached do not immediately allow the nucleation of another bubble, probably as a consequence of local depletion effects.

To conclude, developments reported in this thesis have extended the frontier of bubbly flow modeling and knowledge with specific simulations including non-Newtonian fluid rheology, free surface and bubble nucleation due to phase transition.

CHAPTER 1

INTRODUCTION

In this chapter, an introduction to bubbly flows and their modeling is provided. Despite the widespread application of bubbly flows in industrial equipment, detailed fundamental knowledge is still lacking due to the complexity associated with the intricate interlink between hydrodynamics, mass and heat transport, phase transfer and chemistry. Computational Fluid Dynamics (CFD) at various scales with a multi-scale modeling approach, has proven to be a valuable tool to investigate the relevant phenomena and gain fundamental understanding in order to improve the design and optimization of these processes. Nonetheless, continuous efforts are ongoing to further understand the physics of bubbly flows and further develop models to apply to an increasing number of application fields. In this thesis, three main topics are found to be lacking coverage in the literature regarding the meso-scale modeling of bubbly flows: the non-Newtonian rheology of the fluid, the modeling of the free surface and the formation of bubbles due to supersaturation. This chapter presents a short introduction to the research objectives of this thesis and provides an outline of the thesis.

1.1 Bubbly flows

Bubbly flows are widely encountered in a variety of natural phenomena as well as in many industrial applications thanks to their simplicity of operation and excellent mass and heat transport characteristics. Primary examples are bubble column reactors in processes such as Fischer-Tropsch synthesis, hydrogenation, oxidation and fermentation [1]. In addition, bubbly flows are encountered in electrolytic processes, where gas bubbles are formed on the electrodes.

In order to better design and optimize such processes, fundamental understanding of the underlying physical and chemical phenomena is of outmost importance. As an example, the formation of gas bubbles on the electrodes in electrolytic processes covers partially the surface of the electrode, reducing the available electrode surface area for the reaction. In this respect, an optimal design aims at removing bubbles quickly from the electrode to improve the energy requirements, reduce volumes and optimize the yield of the desired products, which can only be performed when appropriate knowledge and simulation tools are available. This concept is not restricted to electrolytic processes, because for any process involving bubbly flows fundamental knowledge of the behaviour of bubbles is of great importance to understand the evolution of the bubble size distribution and gas residence time (distribution), the mixing in the system and all other relevant parameters required in order to improve the design and optimization of such processes.

Although simple to visualize and operate, bubbly flows present a challenge to understand at a fundamental level, due to the complexity of the interactions between the hydrodynamics, mass and heat transport, phase transfer and chemical reactions, each interlinked with the other. In addition, the flow is rarely in the *homogeneous regime*, where a uniform bubble size distribution and a relatively gentle mixing are present, giving low turbulence, low break-up and coalescence rates and low overall gas holdups. Indeed, industrial bubble columns usually have a high throughput of gas (thus higher superficial gas velocities) which results in the *heterogeneous regime*. In such a situation, the bubble size distribution is wider, with large and small bubbles, due to the increased breakup and coalescence rates. Higher turbulence is also attained and the flow becomes much more unsteady [2], making the system much more complex by nature.

Fundamental understanding regarding these complex flows is thus difficult. Often, experimental techniques are difficult to be implemented, as for instance with high temperatures, opaque liquids, heterogeneous bubbly flows with numerous bubbles covering the others, *etc*. For this reason, with the increasing computational power, numerical simulations have been more and more widespread in order to aid the understanding, the design and the optimization of bubbly flows.

1.1.1 Multi-scale modeling

In the framework of detailed 3D simulations, Computational Fluid Dynamics (CFD) has been widely applied to bubbly flows at different scales. Indeed, a multi-scale modeling approach has proven to be a very effective strategy to capture different levels of details with different techniques [3, 4]. The principle of this approach is simple: very detailed and computationally expensive simulations are used to develop simpler to solve closures for higher scale and unresolved models, with a decreasing level of detail but at a larger scale. Figure 1.1 and

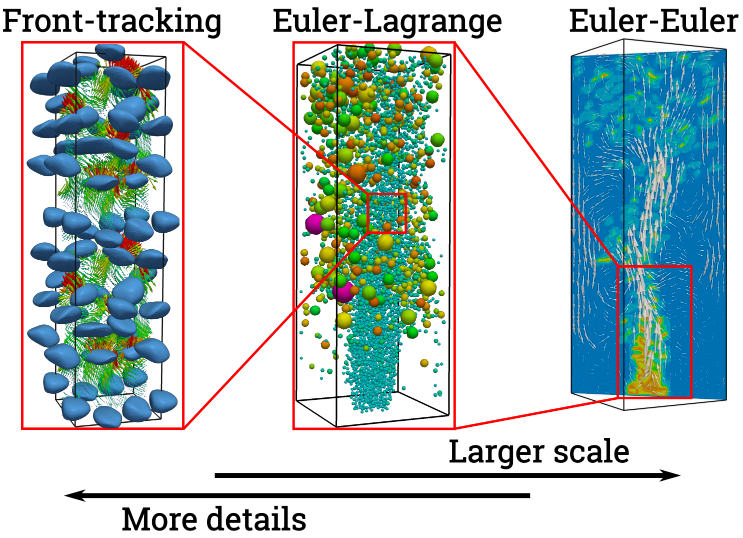

Figure 1.1: Multi-scale modeling approach for bubbly flows, depicting a Front-Tracking model (Direct Numerical Simulations), a Discrete Bubble Model (Euler-Lagrange) and a Two-Fluid model (Euler-Euler) (adapted from Lau et al. [5]).

Table 1.1 show an overview of the different models and strategies applied.

At the smallest scale, Direct Numerical Simulations (DNS) with the highest level of detail are applied. In such models, the (sharp) interface between the bubble and the surrounding liquid is captured with advanced interface tracking methods, such as the Volume-of-Fluid (VOF) or the Front-Tracking (FT) methods. Such methods require an intensive computational

Table 1.1: Multi-scale modeling of bubbly flows: overview of models. Adapted from Darmana [1].

Model	**Description**	**Resolution**	**Applicability**
Two Fluid Model (Euler-Euler)	Averaged mass- and momentum equations for both phases (with or without population balances for bubble size)	Low $\Delta \gg d_b$	Industrial scale $> \mathcal{O}(10^5)$ bubbles
Discrete Bubble Model (Euler-Lagrange)	Volume averaged mass- and momentum equations for the liquid phase, Lagrangian tracking of bubbles	Medium $\Delta \approx d_b$	Meso scale $\approx \mathcal{O}(10^4 - 10^5)$ bubbles
Interface Tracking (Volume of Fluid, Front-Tracking)	Navier-Stokes equations for both phases with advanced (sharp) interface tracking	High $\Delta \ll d_b$	Small scale $\approx \mathcal{O}(10^2)$ bubbles

Δ Grid size, d_b bubble diameter.

effort, because of the resolution required in order to accurately capture the interface. For this reason, they are limited in the size they can reach ($\approx \mathcal{O}(10^2)$ bubbles) but have been extensively used in order to capture detailed physics and develop closure relations for larger scale models, such as for the drag coefficient developed by Dijkhuizen et al. [6] and Roghair et al. [7].

At the meso-scale and the main focus of this thesis, the Euler-Lagrange model (Discrete Bubble Model, or DBM) has been employed to simulate lab-scale columns, as for instance in the case of Darmana et al. [8], Lau et al. [5] and Jain et al. [9], with a high level of detail. Indeed, these models employ a Lagrangian tracking of bubbles, usually assumed spherical, with (binary) interactions such as collisions, coalescence and breakup. Several subgrid phenomena are included in the form of closure relations (either empirical or from DNS), in order to include the relevant physics while employing a grid resolution of the order of the bubble diameter. The advantage of this model is the retain of information of bubbles (such as their size and position) at a much larger scale than the DNS allows.

However, also the Euler-Lagrange model is limited by the number of bubbles that can be simulated in large industrial scale columns. For this reason, often in industry and academia Two Fluid Models (Euler-Euler) are employed, in order to capture the overall averaged flow of both the liquid and gas phases. Indeed, in such models the discrete bubbles are averaged into a continuous phase, losing detailed information on the bubbles, but allowing for scale up to much larger systems. At this level, the importance of correct closure relations is even higher, because much of the underlying physics is lumped into closures. An example of the use of an Euler-Euler model is found in Deen et al. [10].

In addition, several intermediate and hybrid forms have been developed between the described models. For instance, the implementation of a VOF scheme in a DBM (hybrid VOF-DBM) to capture the free surface is found in Jain et al. [9]. A stochastic approach can be used to reduce the number of bubbles in DBM, simulating parcels of bubbles, such as in the approach of Kamath et al. [11]. On the reverse, a population balance modeling technique, which is a statistical representation of bubble sizes and its transport, can be included in Euler-Euler model to recover lost information and improve their predictions, as found in the works by Sanyal et al. [12] or Marchisio and Fox [13].

1.1.2 The Discrete Bubble Model

The Discrete Bubble Model (DBM) has the advantage of reaching a relatively large scales while accounting for bubble interactions, obtaining information on individual bubbles. Thus, it represents a valuable tool in order to investigate phenomena involving groups of bubbles with a certain level of detail, aiding the development of larger scale models such as the Euler-Euler model by providing closures or improved understanding by validated model assumptions.

The basic principle of the Euler-Lagrange DBM is the deterministic treatment of bubbles: while the liquid is treated as a continuum and its mass and momentum conservation equations are discretized and solved on a Cartesian grid, each of the bubble is tracked individually using Newton's laws of motion. By coupling it with mass transfer, it is possible to track the evolution of interphase mass transfer and the growth/shrinking of bubbles. Since details in the positioning of the bubbles is known, accurate account of collisions (and eventually easy addition of coalescence) is an outcome of the model, rather than an input through an empirical correlation. The bubble size, the rise velocity and residence time, can be obtained directly as a result.

As indicated above, the DBM offers several advantages. In the literature, there has been a continuous effort in order to develop and further improve the performance of Euler-Lagrange models for bubbly flows, both including more physics and improving the computational efficiency (*e.g.* parallelization). For example, the model used in this thesis, that will be further explained and developed in the following chapters, has seen various stages of development: from the early transition to a 3D algorithm proposed by Delnoij et al. [14], to the inclusion of coalescence, interphase mass transfer and parallel computing by Darmana [1] to conclude with bubble breakup by Lau et al. [15].

In the literature Euler-Lagrange models have been applied for different purposes. Earlier appearances of this type of models have been around since the 90s, usually with 2D simulations [16, 17]. Several developments were dedicated to the scale-up and the inclusion of physics such as turbulence, collisions, coalescence and breakups in the early 2000s [18, 19, 8, 20, 21]. In recent years, development of stochastic Euler-Lagrange models has seen attempts to reduce the computational cost associated with classic DBM and expand their application to the industrial scales [11]. Nowadays, Euler-Lagrange models are commonly included in commercial software as well, for instance in ANSYS Fluent and OpenFOAM. Euler-Lagrange models have also been applied by Haringa et al. [22] to the simulation of an industrial fermentor, where the discrete Lagrangian phase is represented by microbial cells tracked in a Euler-Euler simulation framework for the gas-liquid flow.

1.2 Challenges

Euler-Lagrange models such as the Discrete Bubble Model show a considerable potential for the simulation of bubbly flows, being able to capture bubble-bubble interactions, their interaction with the fluid as well as a relatively large level of detail of the flow-field. In addition, it is forseeable that in the future the computational power will allow for the further scale-up of such models, even replacing some of the applications where nowadays the Euler-Euler model is commonly employed.

Despite the promising future, there is still a considerable effort ahead in order to improve all existing CFD models to account for different physical and chemical phenomena and to be able to expand their applicability to an increasing number of processes. In particular, several assumptions are still widely applied because limited information is present in the literature. Examples of these are the assumption that the rheology liquid is Newtonian, the numerical treatment of the top free surface as an artificial boundary condition and empirical bubble formation rates (nucleation rates).

These three topics represent relatively *unexplored territories* in the state-of-the-art. Keeping in mind their potential applicability to processes that are becoming increasingly more important, they are analyzed and investigated in this thesis.

1.2.1 Non-Newtonian fluid rheology

Fermentation is a very well known natural process where microbial cells (often referred to as *yeast*) digest nutrients, as for instance sugar. This process, which is very well known and observable in everyday life, is tightly connected with bubbly flows. Often, fermentation processes produce gas bubbles, which are for instance responsible for the taste of alcoholic drinks (*e.g.* in Champagne or beer) or for the leavening of bread, making it soft and easier to chew.

Fermentation is not only found in natural processes, but is also very well-known in industrial applications. Due to the increased demand of sustainability that industry is facing in the last decades, applications of fermentation in bioreactors are increasingly found in the production of chemicals or pharmaceuticals, such as antibiotics [23], bio-ethanol [24], hydrogen and fatty acids [25] and in wastewater treatment [26].

As mentioned, the process of fermentation is entangled with the formation of bubbles as a consequence of the reaction and with the injection of bubbles to aerate the system, providing oxygen to the microbial cells and aiding the removal of the produced gaseous CO_2. The presence of gas bubbles has an influence on the overall dynamics of the fermentor, and has strong interconnections with the mass and heat transport in the column, with the mixing induced by the bubbles and in turn on the performance of the fermentation.

The fermentation broth is often approximated as a Newtonian fluid. However, often the broth rheology is actually non-Newtonian by nature [27], which impacts the general flow circulation patterns in the fermentor as well as the terminal bubble velocity of gas bubbles and their shape. The terminal velocity is one of the most important parameters to consider, because it influences the hydrodynamics as well as the mass and heat transfer in the fermentor, determining the process performance.

The terminal velocity is a direct consequence of the drag force experienced by the rising bubble: a balance between drag and buoyancy determines the bubble rise velocity. It is common in practice to use a drag coefficient, as for instance a closure derived from experiments, in order to estimate the bubble drag and thus its terminal velocity. On the other hand, in the literature a comprehensive description of the drag force for bubbles rising in non-Newtonian fluids is not found.

This presents a first challenge addressed in this thesis: in order to capture the gas bubbles residence time and understand the process performance, an accurate depiction of the drag force is necessary for non-Newtonian liquids, but a comprehensive drag force closure relation for Euler-Lagrange and Euler-Euler models is not available in the literature for non-Newtonian fluids.

1.2.2 Free surface

When modeling the hydrodynamics of a general bubble column, the free surface between the liquid and the top gas freeboard is often neglected or approximated with a fictitious boundary condition or a buffer zone technique. In the Euler-Lagrange model of Darmana [1] the free surface dynamics is neglected and the boundary condition at the top of the column is a degassing condition for the discrete bubbles and a free-slip wall for the liquid. Due to the unsteady nature of the flow and associated variations in bubble hold-up, four openings at the top of the column serve as inflow/outflow channels to account for volume changes due to the injection of bubbles in the system, to ensure stability of the system. On the other hand, such a treatment of the top gas-liquid interface may present unphysical liquid circulations and ignores the free surface dynamics [9]. Moreover, the accounting of the free surface is not only important in Euler-Lagrange models, as Miao et al. [28] found that including a proper treatment of the top gas-liquid interface in Euler-Euler models results in an improvement of the model predictions compared to a degassing condition.

One of the most often selected ways to include the free surface in Euler-Euler and Euler-Lagrange models is through a Volume of Fluid method. This is the preferred method and applied in many commercial CFD packages, such as in the OpenFOAM's *interFoam* solver [29]. This method, however, comes with a few downsides. For instance, plain VOF usually shows a diffuse interface, which spans across several computational cells, or employs interface compression techniques to reduce the numerical smearing of the interface. On the other hand, Deshpande et al. [29] showed for *interFoam* that the performance is worse compared to other methods which track the sharp interface, at the advantage of faster computational times. Reduction of the smearing of the interface resulting from numerical diffusion can be reduced with finer grids, at the cost of higher computational efforts, or by employing surface reconstruction or surface tracking methods.

Interface reconstruction methods, such as the Piecewise-Linear Interface Construction (PLIC) method introduced by Youngs [30], result in a sharp interface, avoiding the problem of numerical diffusion. While their implementation is somewhat straightforward in Euler-Euler models, as it is done in the commercial software ANSYS Fluent which includes VOF with PLIC, in Euler-Lagrange models it presents stability issues when coupled with the Lagrangian bubbles. For instance, Jain et al. [9] require the removal of bubbles two computational cells below the interface of their hybrid Discrete Bubble Model - Volume of Fluid model, causing a mismatch in the volume balance over time and losing the dynamics of bubbles reaching the free surface. One solution to this problem is represented by the model of Li et al. [31], Li and Li [32] and Li et al. [33]: they used ANSYS Fluent employing a transition algorithm for discrete bubbles to transfer them from the Lagrangian to the VOF framework when they become large. However, they discarded small bubbles in the transition, which represents a problem when bubbles do not become extremely large such as in the case simulated by Jain et al. [9]. Moreover, a fine grid is required to accurately simulate bubbles with VOF, increasing the computational cost of this method. An accurate, sharp, grid independent and stable description for the modeling of the free surface is thus challenging to simulate and is investigated in this thesis.

1.2.3 Bubble nucleation

Phase transition and bubble formation is widely found in natural and industrial processes: when opening a bottle of Champagne the change in pressure alters the equilibrium, making the liquid supersaturated with gas which escapes through the formation of bubbles on the surface of the bottle or on the glass. Not limited to natural processes, bubble formation and phase transition are found in several applications in industry, as for instance in fermentation described in Section 1.2.1, and in electrochemical applications where bubbles are formed on the electrodes (*e.g.* water splitting) [34, 35].

CFD simulations of these processes have to include phase transition in order to properly describe the physics of the system. Euler-Euler models typically introduce a gas generation term as a boundary condition on the surface, and in addition a, usually empirical, nucleation rate in terms of bubbles generated per unit time and area is usually employed for Population Balance Models (PBM) [36]. This means that the accuracy of the predictions heavily relies on the accuracy of the closure selected to model phase transition.

On the other side of the scale, Direct Numerical Simulations (DNS) models are limited to few bubbles. Several cases are found in the literature where accurate predictions of the contact angle dynamics, the growth and the shape of the bubbles are recovered with detailed models, such as by Liu et al. [37] which used a Volume of Fluid (VOF) model. Despite their accuracy, such models miss the large scale interactions of multiple bubbles, which cannot be simulated due to the computational cost.

The meso-scale Euler-Lagrange model is thus again a good balance between the two worlds, closing the gap and obtaining information on the behaviour of multiple bubbles growing simultaneously on a surface. Although promising, in the literature a comprehensive Euler-Lagrange model accounting for bubble nucleation on a surface is not present. This has to do with the complexity of the system: bubbles form on crevices and holes on a surface, grow and then detach. This process is influenced by the surface properties (*e.g.* site density and radius), by the supersaturation level, by the flow itself *etc.* In turn, it has an influence on the bubble sizes, the bubble numbers and the induced mixing by the bubbles. An accurate description of the nucleation process for a large number of bubbles is challenging both from the numerical and from the experimental point of view. This is the third challenge addressed in this thesis.

1.3 Research Objectives

This thesis investigates some of the challenges associated with the CFD modeling of bubbly flows and shows the development of a deterministic Euler-Lagrange framework capable of simulating different phenomena prevailing in important processes involving bubbly flows, specifically:

- **Liquid rheology**: in many processes, the fluid rheology is often non-Newtonian [27]. Simulations have been performed either not accounting for such rheology or with simplified power-law formulations. However, the impact of the rheology is not limited to the (apparent) viscosity, but influences the bubble terminal velocity and thus its residence time and the flow patterns. A comprehensive closure for the drag force of gas bubbles rising in non-Newtonian liquids is required in order to simulate such flows.

- **Free surface**: detailed understanding cannot be derived without information on the free surface dynamics and their interaction with the flow and the rising bubbles, which adds layers of complexity. A sharp, stable, accurate description of the surface which allows for bubbles to reach the surface is required in Euler-Lagrange models.

- **Bubble nucleation**: as a consequence of phase transition, local bubble formation (nucleation) is expected to happen at surfaces or impurities in the liquid bulk. A model accounting for the formation of large groups of bubbles on the surface, including the surface physics is missing in the literature.

The objective of this thesis is thus to provide the basis for the inclusion of relevant physical phenomena (*i.e.* the three aforementioned concepts) in the Discrete Bubble Model (DBM) in order to gain better fundamental understanding of these phenomena and expand the range of applicability of the DBM.

1.4 Thesis Outline

This thesis is organized as follows:

- Chapter 2 investigates the drag coefficient of single bubbles rising in different non-Newtonian power-law fluids using a Front-Tracking model. Particular focus is put on the use of a modified Reynolds number to have an accurate prediction of the drag coefficient accounting for the power-law rheology.

- Chapter 3 presents the development of a hybrid DBM-FT model to include an accurate representation of the top gas-liquid interface in a bubble column. The model is then thoroughly validated and compared to the classic DBM approach, especially considering bubble breakup rates close to the interface.

- Chapter 4 is dedicated to the implementation of a bubble nucleation model in the DBM to simulate phase transition as a consequence of supersaturation on a heterogeneous substrate. The model is then used to simulate bubble formation at different supersaturation ratios and with different surface properties.

- Chapter 5 follows the steps of the previous chapter, presenting an experimental study using a dedicated setup to perform bubble nucleation experiments on a given substrate material. The evolution of the measured bubble size distribution at different substrates and supersaturation ratios is compared to the model results and to theoretical expectations.

- Chapter 6 is finally presenting the conclusions and an outlook for further development of the DBM and possible research lines.

CHAPTER 2

DRAG ON SINGLE RISING BUBBLES IN NON-NEWTONIAN FLUIDS *

A Front-Tracking Computational Fluid Dynamics model is used to investigate the behaviour of a single bubble rising in a power-law fluid. A very wide range of viscosities is considered, covering both shear-thinning and shear-thickening behaviour. The power-law exponent n is varied between 0.5 *to* 1.5*, for three different bubble diameters (viz.* 0.5 mm*,* 2 mm *and* 4 mm*). The results show that the non-Newtonian behaviour of the continuous phase strongly influences the shape of the single rising bubbles, as a consequence of the viscosity profiles that develop in the flow field. Hence, large non-spherical bubbles become more spherical in shear-thickening fluids (in comparison to the same bubble in a Newtonian liquid), whereas small spherical bubbles display much more flexible/mobile interface dynamics rising in shear-thinning fluids. To determine the velocity of bubbles in non-Newtonian fluids with a power-law behaviour, the drag closure derived for bubbles rising in Newtonian liquids proposed by Dijkhuizen et al. (2010), which combines viscous drag and shape-induced drag in a single correlation, is adapted using a modified Reynolds number. To conclude, this chapter shows that this adapted correlation is able to predict the terminal rise velocity of single bubbles rising in non-Newtonian power-law fluids within 20% accuracy for the majority of the investigated cases, provided that the drag regime does not change.*

---

[*] This chapter is based on: Battistella, van Schijndel, Baltussen, Roghair and van Sint Annaland (2020) [38]

2.1 Introduction

Bubbly flows represent a widespread class of unit operations in several industrial applications. The continuous phase often exhibits non-Newtonian behaviour, e.g. in bioreactors [39] or polymers production (e.g. polycondensation or polymer devolatilization) [40].

For the design and optimization of process equipment involving bubbly flows it is crucial to accurately predict the bubble rise velocity, since this will largely determine the column hydrodynamics and mass/heat transfer characteristics, and consequently the performance of the equipment. In the pseudo steady-state, the balance between the drag force and the buoyancy forces determines the terminal rise velocity. Although non-Newtonian fluids are common in industry, a complete description of the drag coefficient for a bubble rising in such fluids is still not available [41]. In most cases, the provided closures are empirical and usually limited in their applicability.

With the increase in computational power, numerical simulation has proven to be an effective tool in gaining fundamental understanding of multi-phase gas-liquid flows. In the framework of Computational Fluid Dynamics (CFD), a multi-scale modeling strategy has been applied [3, 4, 5], where micro-scale detailed models are used to develop closure relations for unresolved, higher scale models, such as Euler-Lagrange and Euler-Euler models (see Figure 2.1). The latter treats both phases as a continuum, basically averaging bubble properties on the Eulerian grid, while the former includes more details by tracking each bubble in a Lagrangian manner. Despite the loss of details compared to lower scale models, these methods are computationally favorable, allowing simulations up to industrial scale. On the other hand, the accuracy of the applied closures, for instance to describe phase interactions (hydrodynamic forces, mass and heat transfer), strongly influences the quality of the simulation results of these unresolved models.

Direct Numerical Simulations (DNS) represents a viable option to study phase interactions, to gain fundamental understanding of the physics of bubbly flows and to obtain closures for higher scale models. This approach has been demonstrated in the past for Newtonian fluids [6, 7, 42], where it has been applied for the study of the drag and lift forces on single bubbles and bubbles rising in swarms.

Previously, bubbles in non-Newtonian fluids have been studied using different CFD models. Wu [43] used *Fluent 12.0* to perform Euler-Euler simulations of bubbles rising in shear-thinning fluids in anaerobic digesters, although using a drag law derived for Newtonian fluids. Lattice Boltzmann methods have been successfully employed in the past for simulations of bubbles rising in complex fluids. For instance, Frank and Li [44] simulated a sixth-order Maxwell fluid and were able to capture the negative wake and the bubble teardrop shape, which corresponded to their experimental data. In addition, Liu et al. [45] employed a Volume of Fluid (VOF) method to study the behaviour of multiple bubbles (couples and triplets) rising in shear-thinning fluids. This study focused mostly on collisions and coalescence. Radl et al. [46] investigated the rise of bubbles in different viscous and viscoelastic fluids, with the inclusion of mass transfer, with a hybrid 2D Front-Tracking/Front-Capturing model. Their simulations were limited to 2D, due to the high grid resolution needed by the species solver. Zhang et al. [47] adopted a level-set method to investigate the velocity and viscosity distribution around a single bubble rising in a shear-thinning fluid, described by a Carreau viscosity model. Some attempts have been done in the past to adapt existing drag

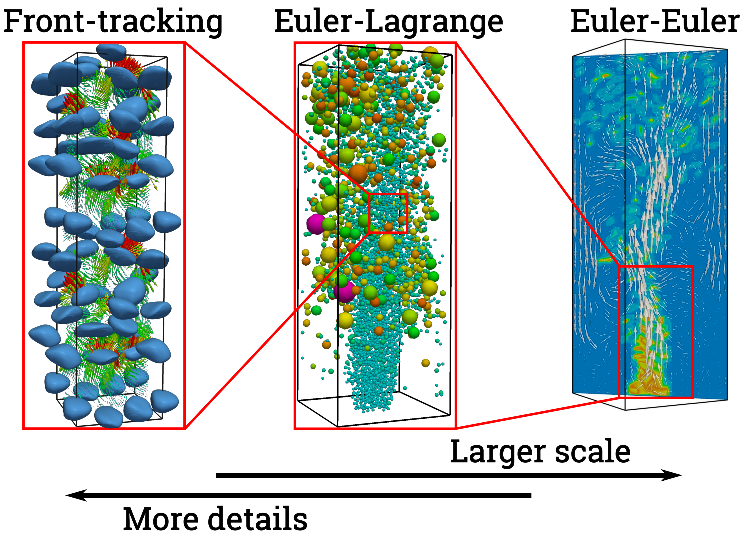

Figure 2.1: Multi-scale modeling strategy for bubbly flows, depicting a Front-Tracking model (Direct Numerical Simulations), a Discrete Bubble Model (Euler-Lagrange) and a Two-Fluid model (Euler-Euler) (adapted from Lau et al. [5]).

correlations to non-Newtonian power-law fluids, such as by Rodrigue [48], who considered shear-thinning polymers at low to moderate Reynolds numbers. The proposed correlation is not suitable for high Reynolds numbers, where it does not converge to a constant as has been well-established in recent years [6].

More recently, Ohta et al. [49, 50] developed a Coupled Level Set-Volume of Fluid model, which they used to study the shape and velocity of bubbles rising in both shear-thinning and shear-thickening power-law fluids, and compared it with experimental data. Premlata et al. [51, 52] also used a VOF method with adaptive grid refinement to study the behaviour of bubbles rising in Carreau-Yasuda fluids. Their study focused on the three-dimensional rising behaviour of single bubbles, and they were able to qualitatively compare their experimentally obtained images of the bubbles to simulation results. The same model has been applied to study viscosity-stratified fluids and viscoplastic materials [53, 54, 55]. An extensive analysis of bubbles rising in viscoplastic fluids has been provided by Tsamopoulos et al. [56], where the bubble rise velocity and the drag coefficient are determined assuming axial symmetry and steady flow. Perhaps the most relevant work related to this chapter is the one by Chhabra [57], where it has been found that standard Newtonian correlations can be adapted to well predict the drag coefficient of non-deformable, solid spheres in shear-thinning power-law fluids, as demonstrated by experimental results.

A comprehensive quantitative description of the drag coefficient for bubbles rising in non-Newtonian fluids has not yet been reported in literature, to the knowledge of the author. The aim of this work is thus to fill this gap and give a description of the drag coefficient for power-law non-Newtonian fluids (both shear-thickening and shear-thinning), following the approach of Dijkhuizen et al. [6] and starting from single bubbles. The starting hypothesis is that it is possible to correct an existing correlation for Newtonian fluids, as for instance the one of Dijkhuizen et al. [6], to account for the non-Newtonian behaviour of the liquid using a generalized Reynolds number [57], as will be explained later.

The chapter is organized as follows: first, the Front-Tracking model used in this work is described and verified. Subsequently, the bubble shapes and viscosity profiles for non-Newtonian fluids will be investigated. To conclude, an outline of the drag coefficient for different power-law fluids will be proposed.

2.2 Model description

The Front-Tracking model used in this work has previously been developed, validated and applied for simulations of bubbles rising in Newtonian liquids. A comprehensive description of the model and its extensive validation for bubbles rising in a liquid can be found in Dijkhuizen et al. [6], Baltussen et al. [58, 59] and Roghair et al. [60, 61]. In this chapter, the model will only be shortly introduced with particular focus on the implementation of the non-Newtonian viscosity model. For further details the reader is referred to the aforementioned papers.

2.2.1 Hydrodynamics modeling

In the Front Tracking model the surface of the bubbles is represented by a triangulated mesh, where the fluid flow (both in the dispersed and continuous phase) is described by the incompressible Navier-Stokes equations and continuity equation using a one-field approximation:

$$\rho \frac{\partial \mathbf{u}}{\partial t} + \rho \nabla \cdot (\mathbf{u}\mathbf{u}) = -\nabla p + \rho \mathbf{g} + \nabla \cdot \boldsymbol{\tau} + \mathbf{F}_{\sigma} \tag{2.1a}$$

$$\nabla \cdot \mathbf{u} = 0 \tag{2.1b}$$

where $\mathbf{u}$ is the fluid velocity, ρ is the fluid density, $\mathbf{g}$ the gravitational acceleration, $\boldsymbol{\tau}$ is the stress tensor, which will be described in more detail in the next sections, and $\mathbf{F}_{\sigma}$ represents a singular source-term for the surface tension force at the interface.

The equations are discretized with a finite-difference technique on a staggered Eulerian grid. The convection terms and the off-diagonal terms of the stress tensor are discretized explicitly, while the diagonal terms of the stress tensor are discretized implicitly resulting in a semi-implicit treatment of the stress tensor enhancing the numerical stability. The flow field is solved using a two-stage projection-correction method, where a pressure-correction step based on the continuity equation is taken iteratively after solving the three momentum balance equations. Both the implicit part of the stress tensor and the pressure correction are solved with an incomplete Cholesky conjugate gradient (ICCG) method [62, 7]. To approximate an infinite quiescent liquid medium, a free-slip boundary condition is applied at the domain walls. The window shifting technique [3] is used to keep the bubble at approximately the same position relative to the domain, which reduces the computational costs.

2.2.2 Surface mesh

The gas-liquid interface is composed of Lagrangian tracking points, connected to form a triangular mesh, where each of the triangular cells is called a surface marker. The Lagrangian points are moved with the local liquid velocity, which is interpolated from the fluid velocity field to the Lagrangian tracking points using cubic splines, using a 4$^{\text{th}}$ order Runge-Kutta time stepping scheme. As a consequence of the separate movement of each marker point, the triangular markers change their relative position at every time step, which will eventually lead to a decrease in the mesh quality and therefore a decrease in the overall accuracy of the surface tension force calculation. Moreover, the bubble volume may no longer be conserved due to non-conservative velocity interpolation. To maintain good interface mesh quality, ensure bubble volume conservation and enhance model performance, (volume conservative) remeshing is an important step in the Front-Tracking technique.

Remeshing operations

Since each marker point is advected individually, the configuration of the mesh changes over time, which will lead to a decrease in the mesh quality and resulting in overall stability and accuracy problems. The marker edges will grow too large or too short, or become otherwise unbalanced. To maintain a good interface mesh quality, to ensure conservation of the liquid volume and to enhance the model performance, (volume conservative) remeshing is an essential part of the Front-Tracking technique. The most basic routines in remeshing are marker point addition (when an edge becomes too long) and marker point removal (when an edge becomes too short). Moreover, we have implemented an edge swapping routine (when it is more favorable to connect points perpendicularly), and a mesh smoothing routine [63] which relocates all the interior points on the interface such that the marker cells become more equilateral while maintaining the intrinsic shape of the interface. A detailed description of the applied remeshing procedures can be found in Roghair et al. [60, 61]. The parameters controlling the remeshing operations are the minimum and maximum edge length, which are respectively 0.2 and 0.5 times the grid size.

Surface tension force

In Equation 2.1a, $\mathbf{F}_\sigma$ represents a force vector describing surface tension acting on the interface markers. It is possible to calculate the individual pull-force of marker i acting on marker m, based on their normal and joint tangent vectors [3], as shown Equation 2.2 and visible in Figure 2.2:

$$\mathbf{F}_{\sigma,i\rightarrow m} = \sigma\left(\mathbf{t}_{mi} \times \mathbf{n}_{mi}\right) \tag{2.2}$$

The total surface tension force on each marker m is thus obtained by summing Equation 2.2 on all the neighboring markers (a, b and c), leading to a net inward force which opposes the pressure jump:

$$\mathbf{F}_{\sigma,m} = \frac{1}{2}\sum_{i=a,b,c} \mathbf{F}_{\sigma,i\rightarrow m} \tag{2.3}$$

The force is then mapped to the Eulerian grid using a mass-weighing stencil as described by Deen et al. [3], modified to account for the local bubble fraction.

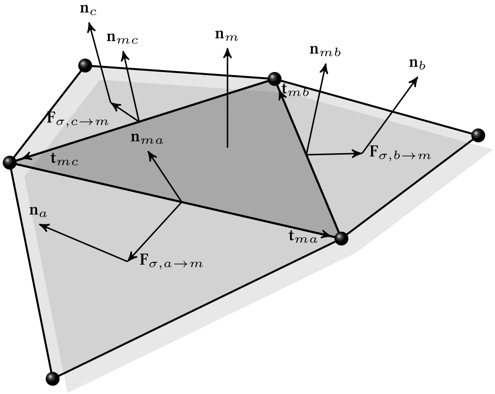

Figure 2.2: Schematic depiction of the calculation of the surface tension force on the triangulated mesh. The figure indicates a marker m and its direct neighbors $i \in \{a, b, c\}$ with their respective normals $\mathbf{n}_m, \mathbf{n}_i$ $i \in \{a, b, c\}$ and their shared tangents $\mathbf{t}_{m,i}$ $i \in \{a, b, c\}$. Adapted from Roghair et al. [61].

2.2.3 Viscosity model

In (inelastic) non-Newtonian fluids, the apparent shear viscosity is not constant, as in Newtonian fluids, but is a function of the shear rate. For a Newtonian fluid, the stress tensor $\boldsymbol{\tau}$ is given by:

$$\boldsymbol{\tau} = -\mu \left(\nabla \mathbf{u} + (\nabla \mathbf{u})^T \right) \equiv -\mu \dot{\boldsymbol{\gamma}} \tag{2.4}$$

in which $\dot{\boldsymbol{\gamma}}$ represents the rate of strain tensor. A frequently applied model to describe the rheology of non-Newtonian fluids, excluding viscoelastic behaviour, is the *generalized Newtonian model*, which simply replaces the viscosity μ in Equation 2.4 with an apparent viscosity η as a function of the shear rate [64]. The shear rate can be written as the magnitude of the rate of strain tensor $\dot{\gamma}$:

$$\dot{\gamma} = \sqrt{\frac{1}{2}(\dot{\boldsymbol{\gamma}} : \dot{\boldsymbol{\gamma}})} \tag{2.5}$$

With the generalized Newtonian model, the stress tensor is calculated as:

$$\begin{gathered} \boldsymbol{\tau} = -\eta \left(\nabla \mathbf{u} + (\nabla \mathbf{u})^T \right) \equiv -\eta \dot{\boldsymbol{\gamma}} \\ \text{with} \quad \eta = \eta(\dot{\gamma}) \end{gathered} \tag{2.6}$$

Several empirical models have been proposed in the literature to describe the relation between the (apparent) viscosity and the shear rate, and the simplest and most widely used correlation is the power-law model (or Ostwald - de Waele relationship):

$$\eta = K \dot{\gamma}^{n-1} \tag{2.7}$$

In Equation 2.7, K represents the consistency index, while n is the flow behaviour index, a constant characterizing the fluid: for $n = 1$ the relation reduces to a Newtonian fluid, for $n < 1$

the fluid is shear-thinning (viscosity reduces with the shear rate) and for $n > 1$ the fluid is shear-thickening (viscosity increases with the shear rate). Although often applied, this model contains a very important physical and numerical shortcoming, as discussed by Gabbanelli et al. [65]. When the fluid is quiescent, or in general in a zero-shear situation, the viscosity becomes infinite for a shear-thinning rheology, while it becomes zero for shear-thickening fluids. Moreover, most non-Newtonian fluids present even more complex behaviour than what is captured with a power-law expression: for instance, they often show Newtonian plateaus around a limited non-Newtonian region. More complex models have been developed to overcome this problem, such as the Carreau model, but these models are usually only valid for a limited type of behaviour (e.g. shear-thinning). A simple but effective solution is to use a *truncated power-law* model [65]:

$$\eta = \eta(\dot{\gamma}) = \begin{cases} \eta_0, & \dot{\gamma} < \dot{\gamma}_0 \\ K\dot{\gamma}^{n-1}, & \dot{\gamma}_0 \leq \dot{\gamma} \leq \dot{\gamma}_\infty \\ \eta_\infty, & \dot{\gamma} > \dot{\gamma}_\infty \end{cases} \tag{2.8}$$

where η_0 and η_∞ are the viscosities calculated with the respective limiting shear rates. To keep consistency between the different cases, it has been chosen to express the limits in terms of η, as described in Table 2.1. Note that the + or − subscripts in Table 2.1 represent 0 or ∞, according to the rheology of the selected fluid, *i.e.* for shear-thinning liquids + and − represent 0 and ∞, respectively, while for shear-thickening liquids + and − represent ∞ and 0. Although these limits guarantee numerical stability especially during the first time step, when the fluid is quiescent and there is no shear, the limits are selected wide enough to maintain a power-law rheology in the whole domain for the remaining of the simulations and thus the selected limits do not affect the terminal rise velocity of the bubbles.

Table 2.1: Truncation limits for the power-law model for each consistency index K.

$K\,[\mathrm{Pa\,s}^n]$	$\eta_-\,[\mathrm{Pa\,s}]$	$\eta_+\,[\mathrm{Pa\,s}]$
10^{-3}	10^{-5}	10^{19}
10^{-2}	10^{-4}	10^{20}
10^{-1}	10^{-3}	10^{21}

2.2.4 Physical properties

Since the interface position is exactly known, the phase fraction ϕ in each Eulerian cell can be computed exactly through geometrical analysis [62]. If a cell contains both liquid and gas, the physical properties density and viscosity need to be scaled accordingly into a macroscopic property. The density of the fluid cell is calculated by weighted averaging with the phase fraction, while the viscosity (or the non-Newtonian apparent viscosity) is calculated via harmonic averaging of the kinematic viscosities following the work of Prosperetti [66]:

$$\rho\left(\mathbf{x}\right) = \sum_{p=0}^{n_{\text{phase}}-1} \phi_p\left(\mathbf{x}\right)\rho_p \tag{2.9a}$$

$$\frac{\rho\left(\mathbf{x}\right)}{\mu\left(\mathbf{x}\right)} = \sum_{p=0}^{n_{\text{phase}}-1} \phi_p\left(\mathbf{x}\right)\frac{\rho_p}{\mu_p} \tag{2.9b}$$

2.2.5 Drag Coefficient

In previous works, the Front-Tracking model has been used to derive a drag correlation for both a single bubble [6] and bubbles rising in a swarm [7]. The terminal velocity of a bubble is determined by a force balance between buoyancy and drag, as described by Roghair et al. [7]. Assuming that the liquid is infinite with zero bulk velocity, the drag coefficient can be expressed as:

$$C_D = \frac{4}{3}\frac{d_b\left(\rho_l - \rho_g\right)g}{\rho_l\left|\mathbf{u}_\infty\right|^2} \tag{2.10}$$

The aim of this chapter is to give a comprehensive description of the drag coefficient of single bubbles rising in non-Newtonian power-law fluids. Thus, the starting point is the adoption of the drag correlation obtained by Dijkhuizen et al. [6]. In particular, Dijkhuizen et al. [6] described the drag coefficient as:

$$C_D = \sqrt{C_D(\text{Re})^2 + C_D(\text{Eo})^2} \tag{2.11}$$

where the Reynolds dependent part, as described by a correlation developed by Mei et al. [67], is used to model the frictional stress (for smaller spherical bubbles):

$$C_D(\text{Re}) = \frac{16}{\text{Re}}\left(1 + \frac{2}{1 + \frac{16}{\text{Re}} + \frac{3.315}{\text{Re}}}\right) \tag{2.12}$$

and the Eötvös dependent part, fitted by Dijkhuizen et al. [6], is used to model the form-drag (i.e. shape-induced, for large deformable bubbles):

$$C_D(\text{Eo}) = \frac{4\text{Eo}}{9.5 + \text{Eo}} \tag{2.13}$$

This correlation achieves a smooth transition when shifting from spherical to deformed bubbles [6].

The Eötvös number can be easily calculated a priori, using physical properties and the bubble diameter:

$$\text{Eo} = \frac{g\Delta\rho d_b^2}{\sigma} \tag{2.14}$$

However, the Reynolds number in Equation 2.12 depends amongst other parameters on the fluid viscosity (which depends on the local shear rate) and the bubble rise velocity u_b. The latter is obtained from the simulation as the time-averaged rate of displacement of the bubble center of mass. The viscosity, in contrast, cannot be directly taken from the simulation results, as it is represented by a field, not by a single, well-defined value as in Newtonian fluids. Instead, the definition for the generalized Reynolds number for power-law fluids, as introduced by Chhabra [68], is used in this work:

$$\mathrm{Re}^* = \frac{\rho u_b^{2-n} d_b^n}{K} \tag{2.15}$$

The rationale behind this choice is that the physics determining the drag coefficient is not altered by the fluid rheology (as for instance with contaminated fluids) but can rather be captured by the changing apparent viscosity in a similar way as for Newtonian liquids, thus using the modified Reynolds number given in Equation 2.15. This has been demonstrated for spheres in shear-thinning liquids by Chhabra [57].

2.3 Verification

The used Front-Tracking model has been thoroughly validated before by Dijkhuizen et al. [6] and Roghair et al. [7] for a wide range of Newtonian liquids and bubble sizes. In this chapter the model verification focuses on the implementation of the non-Newtonian truncated power-law viscosity model and on the grid convergence study.

To verify the correct implementation of the viscosity model, a simple test case is represented by a single phase unidirectional pressure-driven flow between two parallel plates, separated by a distance $2L$ in the y direction, orthogonal to the flow direction x. Assuming that the only non-zero velocity component is $u_x(y)$, it is possible to analytically solve the Navier-Stokes equations (see Equations 2.1a and 2.1b) and obtain the stationary fully developed velocity profile as:

$$\begin{aligned} u_x(y) &= L\frac{n}{n+1}\left(\frac{L}{K}\frac{\partial p}{\partial x}\right)^{1/n}\left(1-\left|\frac{y}{L}\right|^{\frac{n+1}{n}}\right) \\ &= u_{in}\frac{2n+1}{n+1}\left(1-\left|\frac{y}{L}\right|^{\frac{n+1}{n}}\right) \end{aligned} \tag{2.16}$$

where u_{in} represents the inlet velocity, and y the distance from the center of the channel in the positive or negative direction, as it is symmetric. For a liquid described with the truncated power-law viscosity model (Equation 2.8) three distinct regions can be identified:

- a Newtonian region close to the walls (maximum shear)
- a power-law region in between
- a Newtonian region close to the center (no shear)

Since the $\dot{\gamma}$ limits are selected as broad as possible, the two Newtonian regions are reduced to a very small region of the domain, so that it is possible to assume that the power-law model holds throughout the entire domain.

The simulations have been carried out with a rectangular domain where the distance between the plates (12 mm) is much smaller than in both other directions (50 cm). In the

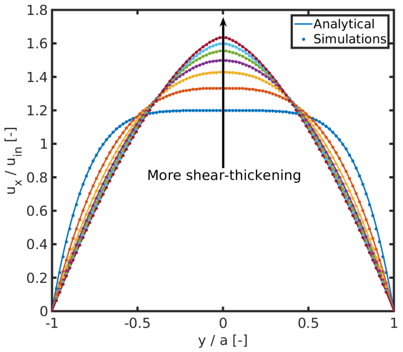

Figure 2.3: Comparison of simulation results with their analytical solutions for the steady-state fully developed velocity profile of a 2D single phase non-Newtonian flow between two parallel plates for different power-law exponents (following the direction of the arrow: $n = 0.2; 0.5; 0.8; 1; 1.2; 1.5; 1.8$).

Table 2.2: Relative error between the numerical and analytical solutions of the velocity profile for a 2D single phase, non-Newtonian flow between two parallel plates.

n	ϵ_{rel}
0.2	0.36%
0.5	0.13%
0.8	0.11%
1	0.10%
1.2	0.10%
1.5	0.10%
1.8	0.10%

y-direction (perpendicular to the direction of the flow) a number of 100 grid cells has been used. The two plates have a no slip boundary condition, while for the depth (the z-direction) a free slip boundary is applied. The other simulations parameters are: a time step of 10^{-2} s, an inlet velocity of $u_{in} = 0.01\,\mathrm{m\,s^{-1}}$, a fluid density of 1000 kg/m^3 and a consistency index $K = 10^{-3}\,\mathrm{Pa\,s}^n$).

Several flow behaviour indices have been tested, including a fully Newtonian case for completeness. The results of the validation are shown in Figure 2.3. The relative error has been calculated as in Equation 2.17 for all the cases, and is given in Table 2.2.

$$\epsilon_{rel} = \frac{||\mathbf{u}_x - \mathbf{u}_x^{\text{analytical}}||_2}{||\mathbf{u}_x^{\text{analytical}}||_2} \tag{2.17}$$

Note that the relative error here is always a positive value, while the relative error in the next sections is calculated without the norm to show the sign of the deviations. The simulation results match very well with the analytical solutions, with a maximal error of only 0.36%, thus confirming the correct implementation of the viscosity model and the validity of the power-

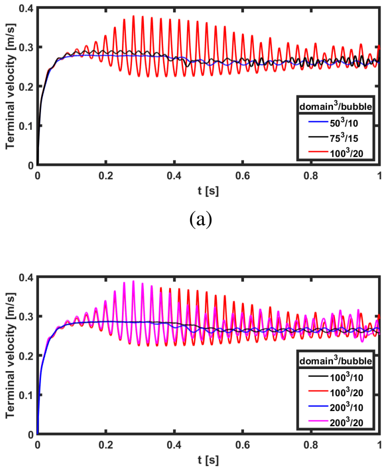

(a)

(b)

Figure 2.4: Rising velocity of a 4 mm bubble rising in a shear-thinning $n = 0.5$ fluid. (a) Constant bubble to domain ratio (1:5) and (b) Varying domain and bubble size

law regime in the whole domain. It is important to mention that the grid used for the actual rising bubble simulations is twice as refined in all directions, in order to accurately capture all dynamic fluctuations in shear rates in the domain, which is one of the main outcomes of the grid dependency study presented below.

2.3.1 Grid dependency

The dependency of the terminal rise velocity of a bubble on the resolution of both the computational domain and the bubble itself has been studied. In the grid-dependency investigation by Dijkhuizen et al. [6] for bubbles rising in viscous liquids, the minimally required domain-to-bubble ratio was determined to be 10, in order to adequately resolve both the bubble motion and the profiles in the domain with sufficient detail; in smaller domain sizes the hydrodynamics is not adequately captured.

To show the effect of the grid resolution, a grid convergence study has been performed using a 4 mm bubble in a Newtonian, a shear-thinning and a shear-thickening liquid with a consistency index $K = 10^{-3}\,\mathrm{Pa\,s}^n$. The bubble is wobbling in both the Newtonian and shear-thinning liquids and thus indicates the minimum number of grid cells required in a bubble diameter to fully capture the dynamic motion of the gas-liquid interface. For the shear-thickening case, the bubble interface is much less dynamic, as the bubble interface remains nearly or completely spherical while rising, and shows strong similarities to the high-viscosity simulations by Dijkhuizen et al. [6], giving information on the domain-to-bubble ratio.

In such case, both the shear-thinning and the Newtonian bubbles show oscillations in the rise velocity, as a consequence of the wobbling behaviour. In Figure 2.4a, an increasing bubble resolution shows a large difference in the rising velocity profile of the bubble. Indeed,

Table 2.3: Terminal velocity for a 4 mm bubble for different flow behaviour indices n at different grid resolutions.

n	d_b	domain^3	$u_{t,\text{simulated}}$ [m s^{-1}]
0.5	10	50	0.2647
	10	100	0.2709
	20	100	0.2744
	20	200	0.2757
1	10	50	0.2743
	10	100	0.2770
	20	100	0.2784
	20	200	0.2818
1.5	10	50	0.2405
	10	100	0.2456
	20	100	0.2460
	20	200	0.2509

a bubble resolution of at least 20 grid nodes is required to adequately capture the amplitude of the oscillations.

Moreover, from Figure 2.4b it is visible that the domain size influences the simulation as well. Indeed, the 100 × 100 × 100 grid cells case is not enough to accurately represent the system, especially for more viscous cases where Dijkhuizen et al. [6] showed that a bubble-to-domain ratio of 10 is required. Despite the differences, Table 2.3 shows that the average terminal velocities are, in all cases, similar with minor deviations between all the different cases, even with a relatively low resolution.

To conclude, to be able to capture both the bubble dynamics and the domain profiles with sufficient detail, a grid of 200 × 200 × 200 with a bubble diameter of 20 grid elements has been selected. A further refinement to the grid has been deemed unnecessary in view of the extensive computational effort already required compared to the expected gain in resolution.

2.4 Results

With the verified Front-Tracking model, single bubbles rising in various shear-thinning and shear-thickening fluids showing a power-law rheology have been simulated. First, the analysis focuses on the effects of the non-Newtonian viscosity profiles on the bubble shape, while the second part will discuss their rise velocity and drag coefficient.

2.4.1 Numerical setup

As mentioned before, the simulation domain is a cube with 200 × 200 × 200 grid cells. A triangulated mesh of a spherical bubble (with a bubble diameter-to-grid ratio of 20) is placed inside the domain, initialized with zero velocity, with its center at a vertical position of 60% of the domain height. This position allows the bubble wake to be completely resolved, while the velocity field at the top of the domain above the bubble remains quiescent.

With the selected time step of 1×10^{-5} s sufficient temporal resolution is achieved and the simulation is continued for 1 s simulation time, in order to obtain a pseudo-steady state, also for the larger bubbles that are known to oscillate during their rise. An initial transient period of 0.2 s is discarded for the time-averaging to determine the terminal velocity of the bubble and the drag coefficient, as described in more detail in Section 2.2.5. An overview of the selected numerical settings is provided in Table 2.5.

The default physical properties are chosen to represent the air-water system for the Newtonian cases (see Table 2.4), while the apparent viscosity is described with the power-law model given by Equation 2.8. Simulations have been performed for different values for the exponent n and for different bubble diameters, as detailed in Table 2.6, while for all the selected bubble diameters three different consistency indices K (1, 10 and 100 times the one of water) have been chosen. For these cases, also the viscosity limits, described in Equation 2.8, have been increased by one or two orders of magnitude, accordingly. For all the cases, simulations with $n = 0.5, 0.8, 1, 1.2$ and 1.5 have been performed.

Table 2.4: Physical properties of the air-water system.

Property	Symbol	Value
Gas density	ρ_g	$1.25\,\mathrm{kg\,m^{-3}}$
Gas viscosity	μ_g	$1.8 \times 10^{-5}\,\mathrm{Pa\,s}$
Liquid density	ρ_l	$1000\,\mathrm{kg\,m^{-3}}$
Surface tension	σ	$0.073\,\mathrm{N\,m^{-1}}$

Table 2.5: Overview of the numerical setup.

Setting	Value
Eulerian grid	$200 \times 200 \times 200$
Domain size/bubble diameter	10
Bubble diameter/grid ratio	20
Time step	1×10^{-5} s
Total simulation time	1 s

Table 2.6: Settings used in the different simulation cases.

Case	d_b [mm]	K [mPa s^n]*	Eo[−]	n [-]
1	4.0	1; 10; 100	2.15	0.5; 0.8; 1; 1.2; 1.5
2	0.5		3.35×10^{-2}	
3	2.0		0.54	

* *Different viscosity limits, see Table 2.1*

2.4.2 Viscosity profiles and bubble shape

The non-Newtonian behaviour of the continuous phase has a large influence on the bubble shape, as well as on the bubble behaviour. In Figure 2.5 and Figure 2.6, snapshots of the bubble for the different cases are shown together with the apparent viscosity profiles and shear rate profiles (namely $\dot{\gamma}$). It is possible to immediately recognize the direct correspondence

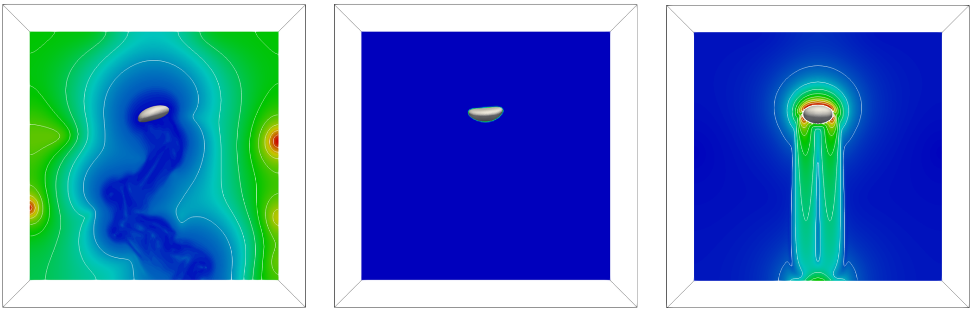

(a) $n = 0.5$ (b) $n = 1$ (c) $n = 1.5$

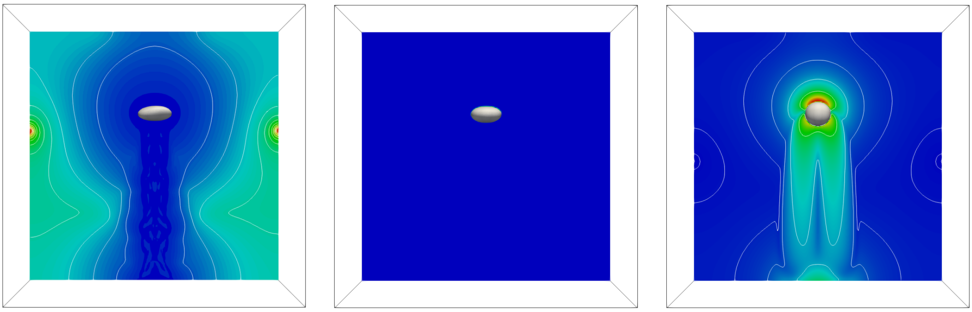

(d) $n = 0.5$ (e) $n = 1$ (f) $n = 1.5$

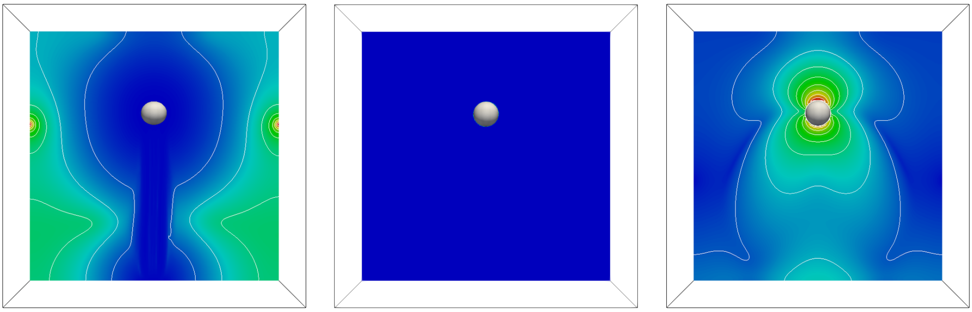

(g) $n = 0.5$ (h) $n = 1$ (i) $n = 1.5$

Figure 2.5: Apparent viscosity profiles at 1s of simulation time around a (a,b,c) 4 mm; (d,e,f) 2 mm; (g,h,i) 0.5 mm bubble in three different fluids: *left* shear-thinning, *middle* Newtonian and *right* shear-thickening. The colors range from lower (blue) to higher viscosity (red).

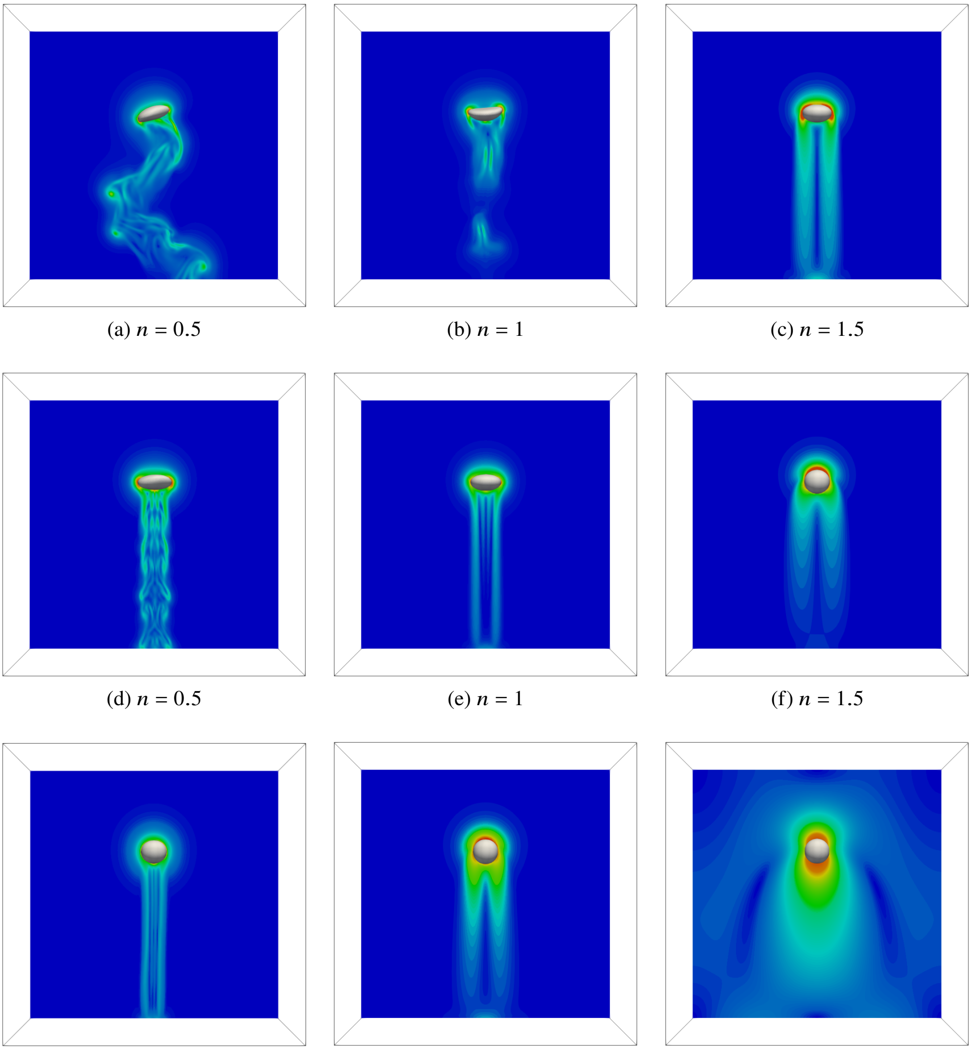

(a) $n = 0.5$ (b) $n = 1$ (c) $n = 1.5$

(d) $n = 0.5$ (e) $n = 1$ (f) $n = 1.5$

(g) $n = 0.5$ (h) $n = 1$ (i) $n = 1.5$

Figure 2.6: Profiles of the shear rate ($\dot{\gamma}$) at 1s of simulation time around a (a,b,c) 4 mm; (d,e,f) 2 mm; (g,h,i) 0.5 mm bubble in three different fluids: *left* shear-thinning, *middle* Newtonian and *right* shear-thickening. The colors range from lower (blue) to higher shear rates (red).

between the magnitude of the shear rate and the apparent viscosity. For instance, Figure 2.5a and Figure 2.6a show a complementary image of the shear rate profiles and the apparent viscosity. The bubble is clearly rising in a meandering motion, as noticeable from the wake. In all cases, the front and wake of the bubble are the regions of higher shear, meaning lower or higher viscosity depending on the type of fluid. Interestingly, the 2 mm bubble of Figure 2.6d is wobbling, as clearly visible from the wake shape, but does not meander as much as the 4 mm bubble.

To characterize the shape of the bubble, it is possible to use the bubble aspect ratio E:

$$E = \frac{d_z}{\sqrt{d_x d_y}} \tag{2.18}$$

The bubble aspect ratio for all the different cases is shown in Figure 2.7. As expected, in all the shear-thickening cases the bubble shape becomes more spherical as a consequence of the increased viscosity in the fluid immediately surrounding the bubble.

The bubble trajectory is strongly affected by the non-Newtonian behaviour of the fluid: for the 4 mm case, the Newtonian fluid exhibits a meandering and wobbling bubble, whereas for the shear-thickening non-Newtonian cases the same bubble is rising in a straight line, as shown in Figure 2.8. This is similar to a bubble rising in a more viscous fluid. The viscosity is mainly affected at the bubble front (where there is a highly shear-thickening region) and then the liquid passes the bubble forming a higher viscosity tail in the wake. Since the larger bubble rises faster, the viscosity reaches a higher maximum value in front of the bubble, while the viscosity is affected in a larger part of the domain for the smaller 0.5 mm bubble.

When inspecting the shear-thinning cases, it is possible to observe that the bubble sphericity has somewhat decreased (see Figure 2.7). The meandering 4 mm bubble maintains this

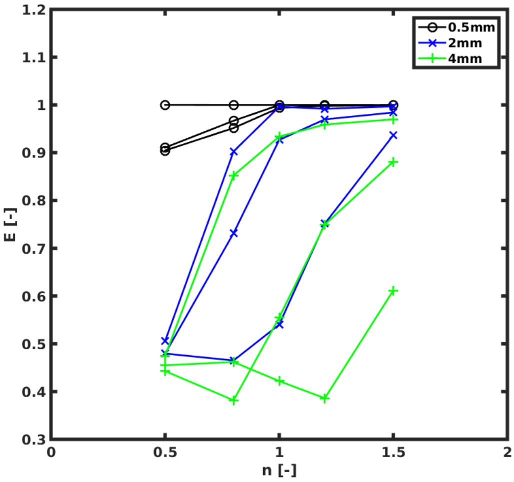

Figure 2.7: Bubble aspect ratio E as a function of the exponent n for all the different cases performed.

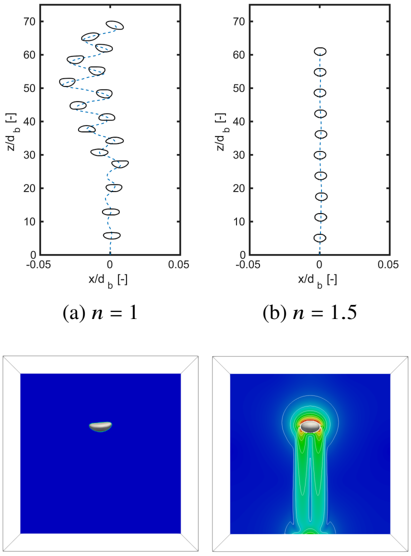

(a) $n = 1$ (b) $n = 1.5$

(c) $n = 1$ (d) $n = 1.5$

Figure 2.8: Comparison of the Newtonian and shear-thickening cases for a 4 mm bubble. (a,b), rising patterns. (c,d), viscosity profiles. The colors range from lower viscosity (blue) to higher viscosity (red).

behaviour and this is also visible in the viscosity profile which follows the bubble pattern. In all three shear-thinning cases displayed in Figure 2.5, two higher viscosity regions can be observed at the walls (as also observed before by Ohta et al. [49]). Interestingly, unlike the shear-thickening case, the regions with a higher viscosity are located at the walls, while regions of lower viscosity are in front of the bubble and in the wake, which follows the meandering path of the bubble for the 4 mm case. Same as before, the 4 mm bubble rises faster, and therefore the viscosity reaches higher (and lower) values due to larger velocity gradients.

The quantification of these effects on the drag coefficient is discussed in the next section.

2.4.3 Drag coefficient

From the Front-Tracking simulations, the time-averaged terminal rise velocity (and thus the drag coefficient) of a single rising bubble is directly available as part of the solution. The computed time-averaged terminal rise velocity is compared with the terminal velocity $u_t(\mathrm{Re}^*, \mathrm{Eo})$ calculated using the drag coefficient detailed in Section 2.2.5, which is a function of the modified Reynolds number (Re^*) given by Equation 2.15. In Figure 2.9, the terminal velocity of a 4 mm bubble rising in fluids with different flow behaviour index n and consistency index $K = 10^{-3}$ Pa s^n is shown. For this case with a relatively large Eo number (Eo = 2.15), the terminal velocity (directly related with the drag coefficient) does not significantly depend on the power-law exponent, because form-drag (viscosity independent) dominates. Only for the case with the highest value for the power-law exponent investigated, viz. $n = 1.5$, the

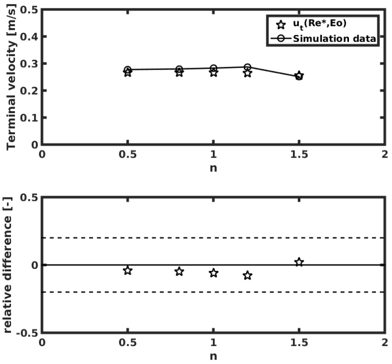

Figure 2.9: Terminal velocity of a 4 mm bubble as a function of the non-Newtonian exponent n for a consistency index $K = 10^{-3}$ Pa s^n.

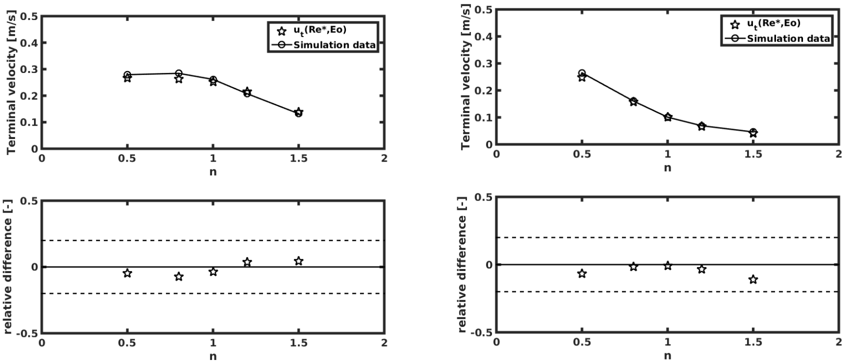

(a) (b)

Figure 2.10: Terminal velocity of a 4 mm bubble as a function of the non-Newtonian exponent n for different consistency indices: (a) $K = 10^{-2}$ Pa s^n and (b) $K = 10^{-1}$ Pa s^n.

terminal velocity slightly decreases, corresponding to the results of a very shear-thickening liquid. This is due to the higher viscosity, which reduces the Re number slightly and increases the bubble sphericity, causing a small deviation from the drag coefficient expected for a Newtonian fluid, also shown in the figure. Clearly, the correlation is able to predict the terminal rise velocity well and matches the computed Front-Tracking terminal velocity within a 20% deviation margin. When the consistency index K is increased by one or two orders of magnitude (see Figure 2.10a and Figure 2.10b), the effect of the highly shear-thickening regime becomes much more pronounced, starting to decrease the terminal velocity of the bubble even more as a consequence of the high viscosity around the bubble itself. The correlation using the modified Reynolds number is still able to predict the bubble terminal velocity reasonably well, with deviations within 20%.

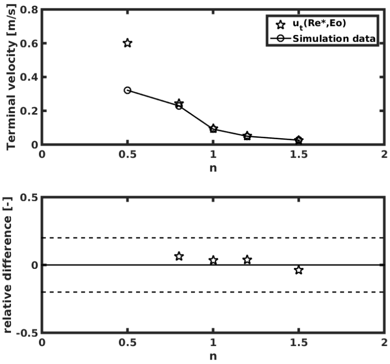

Figure 2.11: Terminal velocity of a 0.5 mm bubble as a function of the non-Newtonian exponent n for consistency index $K = 10^{-3}$ Pa s^n.

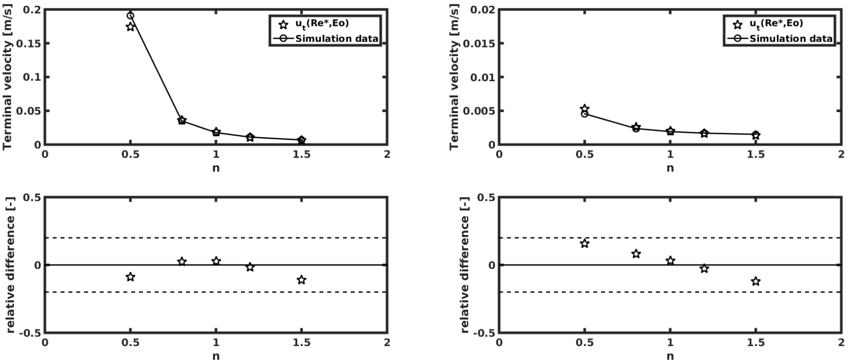

(a) (b)

Figure 2.12: Terminal velocity of a 0.5 mm bubble as a function of the non-Newtonian exponent n for different consistency indices: (a) $K = 10^{-2}$ Pa s^n and (b) $K = 10^{-1}$ Pa s^n.

For smaller bubbles, the Reynolds number decreases, increasing the contribution of the Reynolds dependent part of the drag on the total drag coefficient. For a 0.5 mm bubble a similar dependency of the terminal velocities on the flow behaviour index is found, as shown in Figure 2.11: for exponent values above $n = 1$, the drag coefficient increases drastically, decreasing the terminal velocity of the bubble.

However, despite the similarities in the overall behaviour, there is a large deviation observed between the simulation result and the prediction by the drag correlation based on the modified Reynolds number for the shear-thinning region for small bubbles, where for

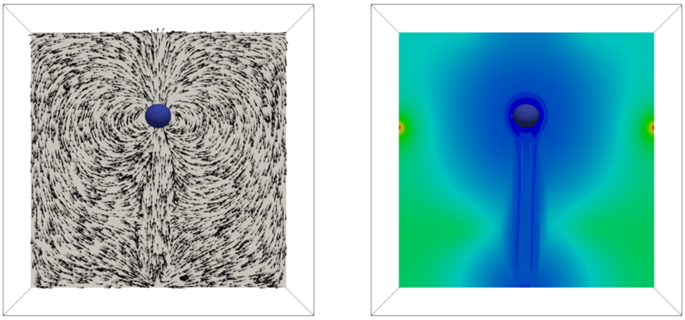

Figure 2.13: Highlight of a 0.5 mm bubble rising in a fluids with a non-Newtonian exponent $n = 0.5$ and a consistency index $K = 10^{-3}\,\mathrm{Pa\,s}^n$. On the left, velocity profile. On the right, viscosity profile.

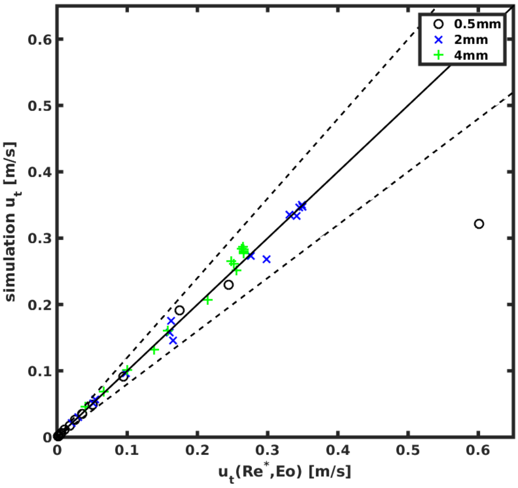

Figure 2.14: Parity plot of all simulation cases showing the calculated vs simulated terminal velocities. The dashed lines represent the ±20% deviation margin.

$n = 0.5$ the error is approximately 87%. This indicates that the correlation is not able to fully describe the drag force in this regime.

First of all, the shape of the bubble is changing from spherical (aspect ratio of 1 for $n = 1$) to slightly ellipsoidal (aspect ratio of 0.9, see Figure 2.5g). In addition to the shape change, the bubble starts to slightly rise in a meandering motion, as visible in Figure 2.13. The cause for the large deviation between the terminal velocity computed with the Front-Tracking model and the velocity predicted by the drag closure is that for a bubble of this size rising in

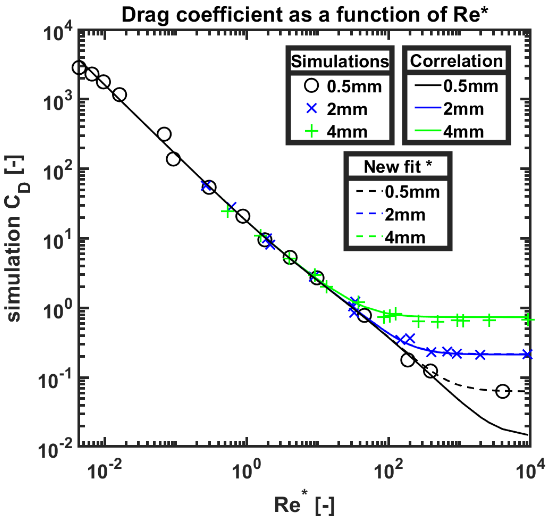

Figure 2.15: Drag coefficient as a function of Re* for different bubble sizes. Comparison of simulation results and correlation.
* The new fit corresponds to $C_D(\mathrm{Eo}) = \frac{4\mathrm{Eo}}{9.5+\mathrm{Eo}} + \frac{1.65\times10^{-3}}{\mathrm{Eo}}$, as suggestion for a better fit.

a Newtonian fluid, the drag on the bubble is dominated by frictional stresses. For the case of a Newtonian fluid, the bubble shape is spherical in this regime and the drag coefficient is dominated by the Reynolds-depending part, which is given by the correlation of Mei et al. [67]. This means that the Eo-dependent part of Equation 2.11 is completely negligible, but in the simulation it is not. Indeed, the correlation from Mei et al. [67] does not account for wake dynamics and shape deformations, and the Eo-dependent part (Equation 2.13) was never fitted for bubbles of this size. Because also small bubbles in shear-thinning fluids experience large shape deformations, the application of the closure from Dijkhuizen et al. [6], based on the correlation by Mei et al. [67] for the Reynolds-depending part, will result in a large deviation in the estimation of the terminal velocity. Indeed, for the same bubble diameter rising in more viscous fluids (with a consistency index K higher by one and two order of magnitudes) a much better agreement with the correlation (see Figure 2.12) is obtained, where the deviation is again within 20% of deviation. This is consistent with the retained sphericity of the bubble in a more viscous environment. On the other hand, with a lower exponent $n = 0.2$ for $K = 10^{-2}\,\mathrm{Pa\,s}^n$, the strong shear-thinning behaviour results again in large deviations in the estimation of the terminal velocity with a deviation of about 74% with an aspect ratio of the bubble of 0.91. As a final remark, it needs to be underlined that this specific case describes an extreme type of power-law liquid. Indeed the fluid viscosity reached around the bubble is in the order of the gas viscosity, which would be extremely improbable in nature. More often, shear-thinning fluids present a higher K value, see for instance Venneker et al. [69].

To conclude, a summary of the results is presented in Figure 2.14 and in Figure 2.15, where all the cases described in Table 2.6 are compared with the terminal velocity and drag coefficient obtained from the correlation of Dijkhuizen et al. [6] using the modified

Reynolds number. Here, is noticeable that the case with a bubble diameter of 0.5 mm falls outside the 20% deviation margin, while all the other cases, including the 2 mm bubble, are within 20% of deviation and the majority of occurrences (80% of the cases) lie within 10% of accuracy. The drag coefficient curve shows this as well, where the transition between frictional (Equation 2.12) and form-drag (Equation 2.13) is visible. This is captured very well for the higher Eo number bubbles (i.e. 2 mm and 4 mm), while the transition is not captured well for the 0.5 mm bubble with $n = 0.5$ and $K = 10^{-3}\,\mathrm{Pa\,s}^n$, as previously discussed. The Eötvös-dependent part of the drag correlation, given in Equation 2.13, can be easily adjusted to account for this case, for instance by adding $1.65 \times 10^{-3}/\mathrm{Eo}$. This will result in a better fit for the transition while marginally affecting higher Eo cases, as shown in Figure 2.15. It needs to be stressed to the reader that this is merely a suggestion on how to improve the fitting to include the missing point, because for a proper correction of the drag correlation many more points at different Eo numbers should be included.

2.5 Conclusions

With a simulation study using a Front-Tracking model, it is shown that non-Newtonian fluids drastically alter the bubble shape and rise velocity as a consequence of the developed viscosity profiles. Especially, large non-spherical bubbles become more spherical in shear-thickening fluids, while the opposite is true for small spherical bubbles in shear-thinning fluids. The drag relation proposed by Dijkhuizen et al. [6], and hereby adapted to use the modified Reynolds number (Re^*), is able to predict the drag coefficient and hence the terminal velocity for moderately non-Newtonian fluids (e.g. $0.5 \leq n \leq 1.5$) within 20% accuracy in most cases, excluding the case for very small bubbles rising in a strongly shear-thinning fluid with very low viscosity, viz. $d_b = 0.5\,\mathrm{mm}$, $K = 10^{-3}\,\mathrm{Pa\,s}^n$ and $n = 0.5$. In this case, the bubble aspect ratio differs strongly from unity and the bubble starts meandering. This behaviour is not accounted for in the drag correlation, as the Newtonian bubble is perfectly spherical and wake dynamics do not play a role. The rise velocity of the same bubble in more viscous fluids with a higher consistency index K do retain their sphericity and do not meander, and the rise velocity is well predicted by the correlation within the 20% deviation margin.

Finally, this work should be further extended to investigate more complex types of fluids, including viscoelasticity and memory effects, and to include swarm effects, ultimately giving the possibility to develop a complete drag closure for unresolved models for all types of fluids.

CHAPTER 3

HYBRID DBM-FT APPROACH FOR BUBBLY FLOWS WITH A FREE SURFACE [*]

The Discrete Bubble Model (DBM), a meso-scale Computational Fluid Dynamics model, allows describing the motion of relatively large swarms of bubbles and can be used to obtain relevant information on the effect of bubble interactions on the large-scale motion of bubbly flows. In such models, the free surface dynamics are rarely accurately tracked, ranging from being neglected in most in-house codes to being described with a diffuse interface in available commercial software. Generally, the inherent assumption is that the interface dynamics does not influence the flow field, except for the close vicinity of the free surface. However, in particular cases, as for instance when dealing with flat columns or shallow volumes, an accurate description of the free surface is needed to avoid instabilities. For these reasons, a Front-Tracking-based free surface has been implemented in an in-house Euler-Lagrange model. The free surface consists of tracer points connected in a triangular mesh. Remeshing procedures have been implemented to maintain a high mesh quality. In this work, the free surface has been carefully validated with synthetic and benchmark test cases, as the filling of a tank, lid driven cavity flow and Rayleigh-Taylor instabilities. In addition, the free surface has been validated with multiphase experimental results of Deen (2001) and with an Euler-Lagrange model without the free surface, to understand the influence of the free surface on the bubble column dynamics.

---

[*] This chapter is based on: Battistella, Kooijman, Roghair and van Sint Annaland, in preparation. [70]

3.1 Introduction

In the past decades, Computational Fluid Dynamics (CFD) have been extensively applied as a tool to complement experiments in the investigation of the complex interactions between hydrodynamics, mass and heat transfer in bubbly flows and gain better fundamental insights (see recent advancements for instance in Shi and Rzehak [72], Kannan et al. [73] and Gemello et al. [74]). The multi-scale modeling framework has often been applied in literature [3, 4, 5] (see Figure 3.1). In such framework, detailed numerical models (often extremely limited by long computational times) are used to improve higher scale, coarser models (suited for larger scale) such as the meso-scale Euler-Lagrange or the large-scale Euler-Euler model. Euler-Lagrange models, although limited to the meso-scale, have the advantage of providing details on bubbles as part of their solution, rather than average properties as in Euler-Euler models.

Often, the top gas-liquid interface of such models is approximated with a fictitious boundary condition or a buffer zone technique [75, 76, 77, 78]. More recently, Darmana et al. [8, 79] used an Euler-Lagrange Discrete Bubble Model (DBM) to simulate chemisorption of carbon dioxide in a sodium hydroxide aqueous solution. In their model, the applied boundary condition at the top of the domain consisted of a free-slip surface for the liquid and degassing for the discrete bubbles. In addition, four symmetrical openings on the side of the column, close to the top surface, were used as inflow/outflow channels for the liquid in order to compensate for volume changes due to the bubble injection guaranteeing stability of the system. Such treatments of the top gas-liquid interface may present unphysical liquid circulations and ignores the free surface dynamics [9].

For Euler-Euler models, Miao et al. [28] found that including a proper treatment of the top gas-liquid interface results in an improvement of the model predictions compared to a degassing condition. Their work relied on a two-fluid model included in the commercial software package CFX.

The top free surface is thus an, often neglected, important boundary condition to be considered. Perhaps the easiest way to include it in Euler-Euler and Euler-Lagrange models is through a Volume of Fluid (VOF) method [80] or its variations. Many commercially available CFD packages include a VOF model, as for instance shown by OpenFOAM's interFoam solver [29]. Deshpande et al. [29] analyzed the performance of this software, which uses an interfacial compression term to reduce numerical diffusion at the interface, showing an acceptable advection error and good capturing of the physics, but a rather worse performance compared to interface reconstruction methods, with the net advantage of faster computational times. Asad et al. [81] coupled a Discrete Bubble Model with VOF in OpenFOAM as well, again using interface compression to reduce the smearing of the interface.

While diffuse and compressed interfaces represent a computationally advantageous choice, they suffer from numerical diffusion resulting in the smearing of the interface over the computational cells, which can be reduced with better numerical methods or finer grids [82]. Interface reconstruction methods, for instance the Piecewise-Linear Interface Construction (PLIC) method presented in Youngs [30], result in a sharper description of the interface but at the cost of higher computational times and more complex three-dimensional algorithms. The commercial package ANSYS FLUENT includes a version of the PLIC method to simulate a sharp interface integrated with the Euler-Euler or Euler-Lagrange models. Li et al. [31], Li

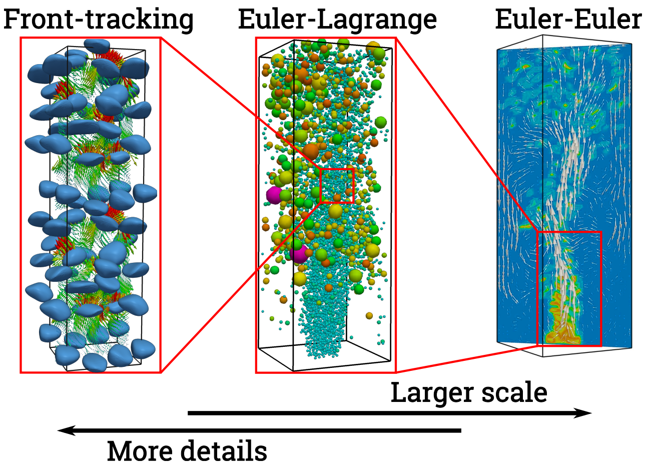

Figure 3.1: Multi-scale modeling strategy for bubbly flows, depicting a Front-Tracking model (Direct Numerical Simulations), a Discrete Bubble Model (Euler-Lagrange) and a Two-Fluid model (Euler-Euler). Adapted from Lau et al. [5].

and Li [32] and Li et al. [33] used it to simulate the bubble-liquid-slag-air four-phase flow in ladle for metallurgy processes. Their model uses a discrete-continuum transition algorithm for large bubbles, to transition DBM bubbles to the VOF framework when they become large. Outside commercial software packages, Jain et al. [9] implemented the VOF model of van Sint Annaland et al. [83] in the in-house Discrete Bubble Model of Darmana et al. [8], with good predictions of the overall liquid and bubble dynamics but with the drawback of numerical instabilities requiring the removal of bubbles two computational cells before the interface, causing a small volume loss. Such loss has limited impact on the hydrodynamics and was considered negligible. Their method, however, dismisses the bubble's arrival at the free surface, arguably the most dynamic part of the process.

In this chapter, a novel approach to the description of the top free surface is presented. A Front-Tracking method [62, 61] is applied for the first time to capture the sharp gas-liquid top interface of the Euler-Lagrange Discrete Bubble Model of Darmana et al. [8]. This hybrid Discrete Bubble Model–Front-Tracking (DBM-FT) method presents several advantages: i) a sharp interface without numerical diffusion at any grid resolution ii) a special treatment of the density allows for the removal of bubbles when they reach the surface without instabilities and iii) does not present numerical coalescence, allowing for possible inclusion of more complex bubble-surface interactions (*e.g.* foaming) in the future.

The chapter is structured as follows: first the hybrid DBM-FT model is described. Subsequently, a comprehensive validation with a variety of test cases is presented. To conclude, the model is validated with experimental data by Deen [71].

3.2 Model description

The hybrid Discrete Bubble Model–Front-Tracking (DBM-FT) consists of an Euler-Lagrange type of model (DBM) where the top gas-liquid free surface is described using a Front-Tracking

(FT) technique. The fundamentals of both models can be found in the works of Delnoij et al. [14], Darmana et al. [8], Lau et al. [15] and Battistella et al. [84] for the DBM and in Dijkhuizen et al. [62], Baltussen et al. [58, 59] and Roghair et al. [7, 60, 61] for the FT.

In the following sections, the model will be described with a particular focus on the integration of the Discrete Bubble Model and Front-Tracking. The reader is referred to the aforementioned papers for additional details on the individual models.

3.2.1 Continuous phase hydrodynamics

The liquid phase and the top gas cap are treated as a single phase, hereby referred to as the *continuous phase* (hereafter found with subscript *c*), using a one-fluid approach. With this approach, a three-phase system (*viz.* liquid, gas cap and discrete gas bubbles) can be reduced to a two-phase Euler-Lagrangian system. The continuous phase hydrodynamics is thus described by the incompressible volume-averaged Navier-Stokes equations:

$$\frac{\partial \alpha_c}{\partial t} + \nabla \cdot \alpha_c \mathbf{u} = 0 \tag{3.1a}$$

$$\rho_c \left[\frac{\partial}{\partial t} (\alpha_c \mathbf{u}) + \nabla \cdot (\alpha_c \mathbf{u}\mathbf{u}) \right] = -\alpha_c \nabla p + \alpha_c \rho_c \mathbf{g} + \nabla \cdot \alpha_c \boldsymbol{\tau}_c + \boldsymbol{\Phi} + \mathbf{F}_\sigma \tag{3.1b}$$

where $\mathbf{u}$ is the continuous phase velocity, α_c represents the continuous phase fraction $(1 - \alpha_b$ where α_b is the discrete bubble fraction), p is the pressure field, $\boldsymbol{\tau}_c$ stands for the stress tensor, $\boldsymbol{\Phi}$ denotes the momentum coupling between the fluid and the discrete bubbles and, to conclude, $\mathbf{F}_\sigma$ is a force representing surface tension at the gas-liquid interface. This set of equations is discretized using finite differences and solved on a three dimensional staggered Eulerian grid.

While the velocity field is continuous across the gas-liquid interface, the shear stresses and pressure are not, and a *jump condition* has to be provided, to properly couple the pressure jump with surface tension at the interface [62]:

$$[-p\mathbf{I} - \boldsymbol{\tau}_c] \cdot \mathbf{n} = \mathbf{F}_\sigma \cdot \mathbf{n} \tag{3.2}$$

where $\mathbf{n}$ represents the normal vector to the interface. It is important to note that the phase properties, such as density and viscosity, are also discontinuous at the interface. The pressure jump condition and phase properties will be described further in the following sections.

In Equation 3.1b and 3.2, the stress tensor, for a Newtonian fluid, is described as:

$$\boldsymbol{\tau}_c = -\mu_{c,\text{eff}} \left[\nabla \mathbf{u} + (\nabla \mathbf{u})^T - \frac{2}{3} \mathbf{I} (\nabla \cdot \mathbf{u}) \right] \tag{3.3}$$

The effective viscosity $\mu_{c,\text{eff}}$ is calculated using the LES sub-grid scale turbulent viscosity model of Vreman [85]:

$$\mu_{c,\text{eff}} = \mu_c + \mu_T \tag{3.4a}$$

$$\mu_T = 2.5 \rho_c C_S^2 \sqrt{\frac{B_\beta}{\alpha_{ij} \alpha_{ij}}} \tag{3.4b}$$

where $\alpha_{ij} = \partial u_j / \partial x_i$, $B_\beta = \beta_{11}\beta_{22} - \beta_{12}^2 + \beta_{11}\beta_{33} - \beta_{13}^2 + \beta_{22}\beta_{33} - \beta_{23}^2$ and $\beta_{ij} = \Delta_m^2 \alpha_{mi}\alpha_{mj}$. The constant C_S represents the Smagorinsky constant and is set to a value of 0.1, while Δ_i is the filter width in the i direction [84].

3.2.2 Free surface

The Front-Tracking method is used to model the gas-liquid free surface between the liquid bulk and the gas cap. The free surface is described as an unstructured mesh consisting of Lagrangian marker points, connected to form triangular marker cells. Upon initialization, the marker points are distributed over the entire free surface, while imposing that the points at the outer edges of the mesh are exactly on the domain boundaries, which will act as anchor points. A description of the movement of wall markers will follow below. Each of the interior points is advected with a 4th order Runge-Kutta time stepping scheme in accordance with the local fluid velocity, interpolated using cubic splines [61].

Remeshing operations

Since each marker point is advected individually, the configuration of the mesh changes over time, which will lead to a decrease in the mesh quality and resulting in overall stability and accuracy problems. The marker edges will grow too large or too short, or become otherwise unbalanced. To maintain a good interface mesh quality, to ensure conservation of the liquid volume and to enhance the model performance, (volume conservative) remeshing is an essential routine of the Front-Tracking technique. The most basic routines in remeshing are marker point addition (when an edge becomes too long) and marker point removal (when an edge becomes too short). Moreover, we have implemented an edge swapping routine (when it is more favorable to connect points perpendicularly), and a mesh smoothing routine [63] (simultaneous underrelaxed weighted Laplacian volume-conservative smoothing) which relocates all the interior points on the interface such that the marker cells become more equilateral while maintaining the intrinsic shape of the interface. A detailed description of the applied remeshing procedures can be found in Roghair et al. [60, 61]. The parameters controlling the remeshing operations are the minimum and maximum edge length, which are respectively 0.2 and 0.5 times the grid size.

Wall markers

As mentioned before, the surface needs to be anchored at the walls. By definition, the interface cannot detach or cross the boundary walls. This, in combination with the no-slip boundary condition commonly employed at the walls for the continuos phase, leads to completely immobile points at the walls. As it is clear that this is non-physical as the interface could move along the wall, for instance in case of liquid filling or drainage of the column. To avoid the implementation of contact angle dynamics, considered as a subgrid scale phenomenon for the considered resolution, the smoothing operation described before takes care of the flattening of the interface at the walls, while keeping such points anchored at the wall.

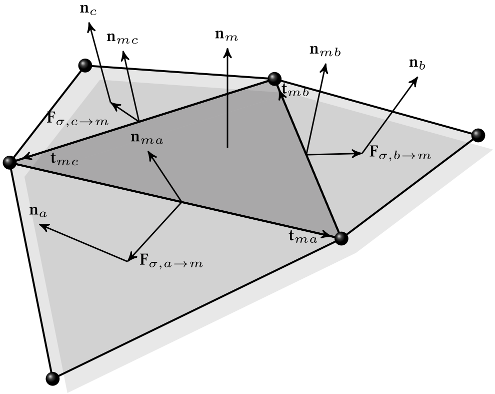

Figure 3.2: Schematic depiction of the calculation of the surface tension force on the triangulated mesh. The figure indicates a marker m and its direct neighbors $i \in \{a, b, c\}$ with their respective normals $\mathbf{n}_m, \mathbf{n}_i$ $i \in \{a, b, c\}$ and their shared tangents $\mathbf{t}_{m,i}$ $i \in \{a, b, c\}$. Adapted from Roghair et al. [61].

Surface tension force

In Equation 3.1b, $\mathbf{F}_\sigma$ represents a force vector describing surface tension acting on the interface markers. It is possible to calculate the individual pull-force of marker i acting on marker m, based on their normal and joint tangent vectors [3], as done in Equation 3.5 and shown in Figure 3.2:

$$\mathbf{F}_{\sigma,i\rightarrow m} = \sigma\left(\mathbf{t}_{mi} \times \mathbf{n}_{mi}\right) \tag{3.5}$$

The total surface tension force on each marker m is thus obtained by summing Equation 3.5 over all the neighboring markers (a, b and c), leading to a net inward force which opposes the pressure jump:

$$\mathbf{F}_{\sigma,m} = \frac{1}{2}\sum_{i=a,b,c} \mathbf{F}_{\sigma,i\rightarrow m} \tag{3.6}$$

The force is then mapped to the Eulerian grid using a mass-weighing stencil as described by Deen et al. [3], modified to account for the local discrete phase bubble fraction:

$$\mathbf{F}_\sigma = \frac{\sum_m \alpha_c \rho_c D\left(\boldsymbol{x} - \boldsymbol{x}_m\right)\mathbf{F}_{\sigma,m}}{\sum_m \alpha_c \rho_c D\left(\boldsymbol{x} - \boldsymbol{x}_m\right)} \tag{3.7a}$$

$$D(\mathbf{r}) = d_x(r_x) d_y(r_y) d_z(r_z) \tag{3.7b}$$

$$d_x(r_x) = \begin{cases} 1 - \frac{|r_x|}{h} & \text{if } |r_x| \leq h \\ 0 & \text{if } |r_x| \leq h \end{cases} \tag{3.7c}$$

Phase fraction and physical properties

The one-fluid approach uses a phase fraction, hereby referred to as H_c, which varies between 0 (continuous gas phase, or in other words the gas on top of the surface) or 1 (continuous liquid phase), to calculate macroscopic physical properties such as density and viscosity in a Eulerian cell. The position of the interface is known exactly, by means of the markers, thus allowing to compute geometrically the phase fraction in each computational cell, following the procedure depicted in Dijkhuizen et al. [62].

Once the phase fraction is known, we calculate the density by weighted averaging and the kinematic viscosity by harmonic averaging [66] in each cell:

$$\rho_c = H_c \rho_l + (1 - H_c)\,\rho_g \tag{3.8a}$$

$$\frac{\rho_c}{\mu_c} = H_c \frac{\rho_l}{\mu_l} + (1 - H_c)\,\frac{\rho_g}{\mu_g} \tag{3.8b}$$

One particular problem arises with the interpolation of the continuous phase density at the cell phases. Indeed, due to the staggered grid, in the discretization of convective fluxes it is necessary to interpolate cell-centered macroscopic properties (including density) to the computational cell faces. Standard CFD algorithms make typically use of interpolation (often linear) from the cell centered densities. Due to the free surface and the large density difference between the gas and liquid, this leads in certain cases to the pressure gradient being smeared over the rather sharp density gradient, leading to spurious high-pressure regions just above the surface, resulting in turn in a discontinuous velocity field, especially for cells with a very low phase fraction H_c.

To avoid this problem, the density field is not interpolated at the top and bottom cell faces. Instead, the phase fraction is calculated exactly by shifting the reference frame by half the cell in the z-direction, thus allowing to calculate the density at the face without interpolation using Equation 3.8a (see Figure 3.3). Since this is an expensive procedure in terms of computational cost, it is performed only in the z-direction, which is the same direction of gravity. This could theoretically be a possible source of instabilities in the computation in the presence of an extremely deformed surface, but such problems were never encountered in the course of this work, even with very wavy surfaces.

3.2.3 Discrete bubbles

The remaining phase is represented by the discrete gas bubbles rising in the liquid (hereafter subscripted with b). Each of the bubbles is tracked in a Lagrangian fashion using Newton's laws of motion, described in Equation 3.9a:

$$\rho_b V_b \frac{d\mathbf{v}}{dt} = \sum \mathbf{F} \tag{3.9a}$$

$$\frac{d\mathbf{x}_b}{dt} = \mathbf{v} \tag{3.9b}$$

where $\mathbf{v}$ represents the bubble velocity and $\mathbf{x}_b$ its position. Equation 3.9a needs to be closed with a description of the sum of the forces acting on the bubble, which is given in Equation 3.10

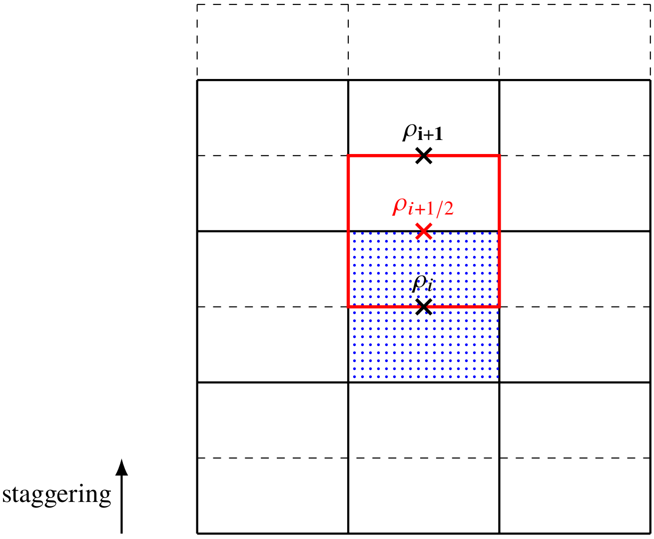

Figure 3.3: Schematic depiction of the density calculation at the cell face ($\rho_{i+1/2}$). The density can be obtained from: a) linear interpolation of ρ_i and ρ_{i+1} (classical method) or b) staggering of the grid by half a cell in the z-direction to calculate the density at the new cell center, located on the face of the computational cell (new method).

accounting for buoyancy, drag (including swarm effects) [6, 7], lift [86], virtual mass [87] and wall-interactions [88].

$$\sum \mathbf{F} = \mathbf{F}_G + \mathbf{F}_P + \mathbf{F}_D + \mathbf{F}_L + \mathbf{F}_{VM} + \mathbf{F}_W \tag{3.10}$$

An overview of the different closure relations is given in Table 3.1, as previously described by Lau et al. [15] and Battistella et al. [84].

Bubble interactions

Due to the Lagrangian description of the gas bubbles, their individual positions and velocities are available at run time, resulting in the straightforward inclusion of binary collisions, coalescence and break-up. The hard-sphere model of Hoomans et al. [89], adapted by Delnoij et al. [14], is hereby applied to perform elastic collisions between two bubbles or a bubble and a wall, in a event-based fashion. The neighbor list algorithm described by Darmana et al. [8] is employed to reduce the computational time.

Moreover, bubble coalescence is included when two bubbles are in contact for enough time for the thin liquid film in between them to drain. Several models are available in the literature. Similar to Lau et al. [15], in this work the film drainage model by Darmana et al. [8] is applied. If the drainage time criterium is met, the two bubbles will coalesce to form a larger bubble whose mass is equal to the sum of the two parents.

Table 3.1: Forces acting on a bubble.

Force	Closure relation	Reference
$\mathbf{F}_G = \rho_b V_b \mathbf{g}$	-	-
$\mathbf{F}_P = -V_b \nabla P$	-	-
$\mathbf{F}_D = -\frac{1}{2} C_D \rho_l \pi R_b^2 \lvert \mathbf{v} - \mathbf{u} \rvert (\mathbf{v} - \mathbf{u})$	$\frac{C_D}{C_{D,\infty}} = \left(1 + \frac{18}{\mathrm{Eo}} \alpha_b\right) \alpha_l$ $C_{D,\infty} = \sqrt{C_{D,\infty}(\mathrm{Re})^2 + C_{D,\infty}(\mathrm{Eo})^2}$ $C_{D,\infty}(\mathrm{Re}) = \frac{16}{\mathrm{Re}} \left(1 + \frac{1}{1 + \frac{16}{\mathrm{Re}} + \frac{3.315}{\sqrt{\mathrm{Re}}}}\right)$ $C_{D,\infty}(\mathrm{Eo}) = \frac{4\mathrm{Eo}}{\mathrm{Eo}+9.5}$	[6, 7]
$\mathbf{F}_L = -C_L \rho_l V_b (\mathbf{v} - \mathbf{u}) \times (\nabla \times \mathbf{u})$	$C_L = \begin{cases} \min[0.288 \tanh(0.121\mathrm{Re}), f(\mathrm{Eo}_d)] & \mathrm{Eo} < 4 \\ f(\mathrm{Eo}_d) \quad 4 \le \mathrm{Eo} & \le 10 \\ -0.29 & \mathrm{Eo} > 10 \end{cases}$ $f(\mathrm{Eo}_d) = 0.00105\mathrm{Eo}_d^3 - 0.0159\mathrm{Eo}_d^2 - 0.0204\mathrm{Eo}_d + 0.474$ $\mathrm{Eo}_d = \frac{\mathrm{Eo}}{E_b}, \quad E_b = \frac{1}{1+0.163\mathrm{Eo}^{0.757}}$	[86]
$\mathbf{F}_{VM} = -C_{VM} \rho_l V_b \left(\frac{D\mathbf{v}}{Dt} - \frac{D\mathbf{u}}{Dt}\right)$	$C_{VM} = 0.5$	[87]
$\mathbf{F}_W = -C_W R_b \left(\frac{1}{y^2} - \frac{1}{(L-y)^2}\right)$ $\rho_l \lvert (\mathbf{v} - \mathbf{u}) \cdot \mathbf{n}_z \rvert^2 \mathbf{n}_w$	$C_W = \begin{cases} e^{(-0.933\mathrm{Eo}+0.179)} & 1 \le \mathrm{Eo} \le 5 \\ 0.007\mathrm{Eo} + 0.04 & 5 \le \mathrm{Eo} \le 33 \end{cases}$	[88]

In addition to coalescence, single bubbles can also break as a consequence of various factors, such as turbulent fluctuations, viscous shear stress, surface instabilities *etc.* [90]. The break-up model implemented in the DBM is based on the work of Lau et al. [15]: break-up occurs when the inertial forces acting on the bubble (causing deformations) are larger than the surface tension force. The break-up is considered binary, resulting in the formation of two daughter bubbles with a size taken from a U-shaped daughter size distribution. The largest of the two bubbles is assigned the parent's original position while the smaller is randomly placed around the other, at a distance of 1.1 times the sum of their radii, preventing overlap and immediate coalescence of the two daughter bubbles (see Lau et al. [15]).

Bubble removal

Bubbles are removed as soon as they touch the interface. Jain et al. [9] found instabilities in the handling of bubbles too close to the top interface, forcing them to remove bubbles two cells below the surface. In this work, bubbles are removed when their center of mass crosses the upper boundary of the cell containing the interface. Indeed, the introduced numerical treatment of the continuous phase density, the mass weighing of the forces from the discrete to the continuous phase and the handling of the wall markers allow for the stable operation of the free surface and for the removal of bubbles as soon as they touch the interface, without instabilities. When bubbles are removed, the change in discrete phase fraction effectively causes liquid inflow from the surrounding cells resulting in a "pull down" of the free surface, to conserve the liquid mass. In addition, given that the objective is not to fully capture bubble-surface dynamics, a more detailed description of the bubble merging and popping with the top interface is not required. A more accurate model for such behaviour might be desired if foaming or complex interface dynamics are studied.

3.2.4 Numerical Implementation

The computational sequence for the DBM-FT model is shown in Figure 3.4. As shown in Figure 3.4, the bubble dynamics is solved first, followed by the interface advection and remeshing. The flow is solved last, using a second order Barton scheme for the convection terms [91]. The viscous stress tensor is treated explicitly, as well as the surface tension force and the inter-phase coupling, using a modified SIMPLE scheme. The discretized system of algebraic equations is then solved iteratively with a Preconditioned Conjugate Gradient method included in the scientific library PETSc [92, 93, 94], until the mass defect (D_f) is below the selected tolerance (10^{-13} kg).

Two-way coupling

The two-way coupling between the Eulerian grid and the Lagrangian bubbles is performed through a clipped fourth-order polynomial mapping technique, following the work of Deen et al. [3]. An important issue with this method is that, when bubbles get close to the interface, a large force is mapped to the gas phase above the free surface, generating large pressure gradients and spurious currents, causing the interface to deform abruptly. A mass weighing concept, similar to the one applied for the surface tension force described in Section 3.2.2, is therefore added to the stencil derived by Deen et al. [3].

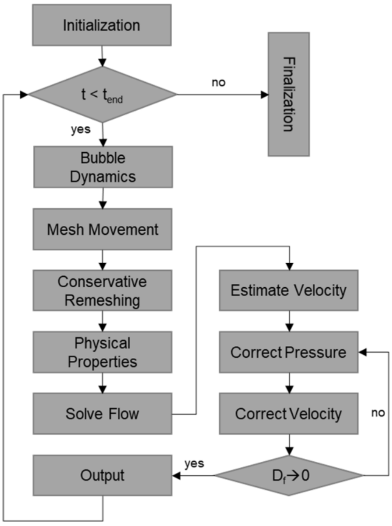

Figure 3.4: Order of operations for the DBM-FT model

In general, the Eulerian quantity $\Phi(j)$ at cell j is calculated from the Lagrangian quantity $\phi(b)$ of all the bubbles in the mapping window B, by [5]:

$$\Phi(j) = \frac{1}{V_{cell}} \sum_{\forall\, b \in B} \phi(b) \int_{-n}^{+n} \int_{-n}^{+n} \int_{-n}^{+n} D(x-x_b)D(y-y_b)D(z-z_b)\, dx\, dy\, dz \tag{3.11}$$

The weighing factor is thus described by (in the x direction):

$$\begin{gathered} D(x-x_b) = \frac{15}{16}\frac{\rho_c}{\rho_l}\left[\frac{(x-x_b)^4}{n^5} - 2\frac{(x-x_b)^2}{n^3} + \frac{1}{n}\right]; \\ -n \leq (x-x_b) \leq +n \end{gathered} \tag{3.12}$$

where x is the x-position of the Euler node, x_b is the x-position of the bubble and n is the so-called mapping window [5].

The mass weighing allows to avoid mapping too large forces to the top liquid interfaces, while at the same time conserving the traditional force mapping for bubbles fully immersed in the liquid phase.

3.3 Verification and validation

The DBM has been extensively validated in the past with experimental data, see for instance the work of Darmana et al. [8] and Lau et al. [15]. With the current implemented extensions, the newly added free surface has to be thoroughly validated as well.

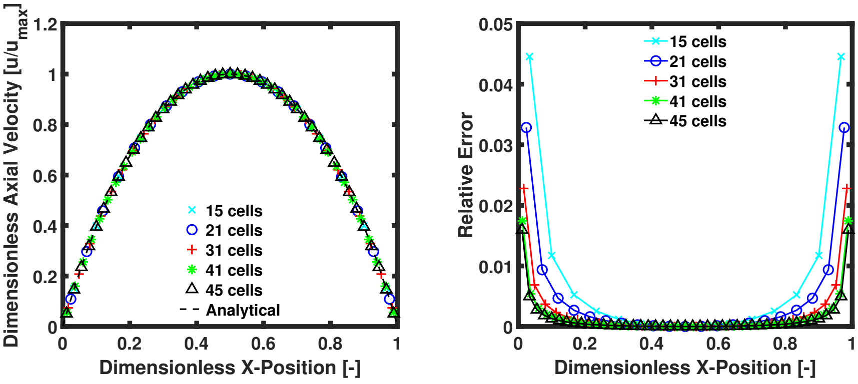

(a) (b)

Figure 3.5: (a) Dimensionless axial velocity profile: comparison between simulations and analytical solution. (b) Relative error.

3.3.1 Single phase flow

The flow solver has been modified since the work of Lau et al. [15]: *i.e.* the density has been taken out of the derivatives in Equation 3.1a and Equation 3.1b in view of the incompressibility of the liquid. As a consequence, the flow solver has to be verified again. The chosen verification case is laminar flow through a rectangular duct: a liquid with an inlet velocity of $0.1\,\mathrm{m\,s^{-1}}$ enters a $5 \times 5\,\mathrm{cm}$ column and flows for a length of $25\,\mathrm{cm}$. The dimensionless axial velocity profile has an analytical solution, as described by Holmes and Vermeulen [95]:

$$\frac{u_z}{u_z^{max}} = \frac{\sum\limits_{k=1,3,5\ldots}^{\infty} (-1)^{1/2(k-1)} k^{-3} \cos\left(\frac{1}{2}k\pi\zeta\right) \left\{1 - \frac{\cosh(\frac{1}{2}k\pi\xi\frac{B}{H})}{\cosh(\frac{1}{2}k\pi\frac{B}{H})}\right\}}{\sum\limits_{k=1,3,5\ldots}^{\infty} (-1)^{1/2(k-1)} k^{-3} \left\{1 - 1/\cosh(\frac{1}{2}k\pi\frac{B}{H})\right\}} \tag{3.13}$$

where B and H represent the breadth and height of the cross section (as mentioned, both 5 cm). $\zeta = 2y/H$ and $\xi = 2x/B$ represent the reduced position along the breadth and height of the cross section.

As can be discerned from Figure 3.5a, the simulation results for fully developed flow through a rectangular domain match very well with the analytical solution, at five different grid resolutions, namely 15 to 45 cells per side. In addition, the relative error for each ζ and ξ positions is calculated as:

$$\varepsilon(\zeta, \xi) = \frac{u_z(\zeta, \xi) - u_{z,\mathrm{analytical}}(\zeta, \xi)}{u_{z,\mathrm{analytical}}(\zeta, \xi)} \tag{3.14}$$

Since the axial velocity is normalized with the maximum velocity, the relative error is exactly zero at the center of the column. This is captured by Figure 3.5b. The relative error increases

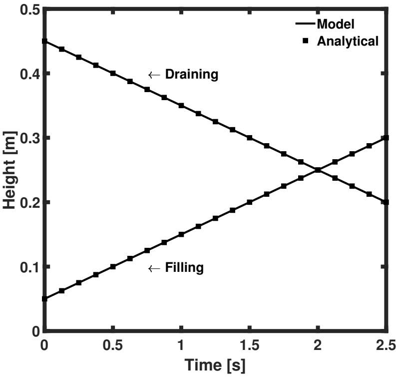

Figure 3.6: Change of the liquid height over time for the filling and draining cases: comparison with the analytical solution

towards the edges, as expected, but remains nonetheless relatively small, within 5% even for the coarser resolution of only 15 cells. It is important to note that another source of error lays in the maximum velocity itself, which is not captured by the dimensionless velocity profile. This error was also calculated less than 5% for the 15 cells case. In addition, second order convergence was confirmed from the velocity profile calculations.

3.3.2 Free surface

With the verified flow solver, this section continues to verify the free surface implementation. Two verification cases are shown, in order to validate both the kinematic and dynamic conditions of the interface. In addition, a few stability tests of the interface are performed, together with a verification of the surface tension implementation.

Kinematic condition

The kinematic condition specifies that the interface is sharp, meaning no flow crosses the free surface. An easy verification case is the filling or draining of a square column with a liquid in presence of a top gas layer. In the case of filling, liquid is injected from the entire bottom with a constant velocity ($0.1\,\mathrm{m\,s^{-1}}$) and in the draining case liquid is removed with the same velocity, while gas enters/leaves the system from the top with a inflow/outflow boundary condition to compensate for the liquid height changes. As visible from Figure 3.6, the analytical solution is matched, confirming the correct kinematic behaviour.

Dynamic condition

The dynamic condition ensures momentum is conserved at the free surface. In essence, tangential stresses are continuous while normal stresses are opposed by surface tension, as described by Equation 3.2. To validate the implementation of the jump condition, a lid driven cavity flow is studied.

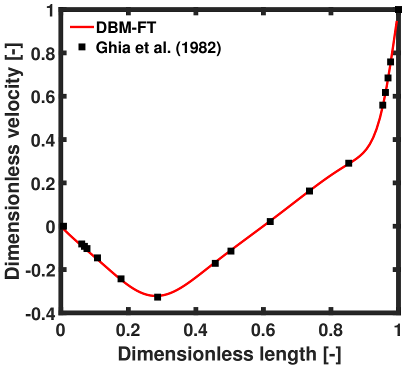

Figure 3.7: Dimensionless velocity profile: comparison with the results from Ghia et al. [96].

Before entering the investigation of the two phase flow, a single phase case is verified. A pseudo 2D high resolution domain is compared to the 2D solution obtained by Ghia et al. [96]. The system height and width are equal (aspect ratio of 1) and the wall velocity corresponds to a Reynolds number of 400, to ensure laminar flow. To obtain a pseudo 2D system, the boundary conditions are set to no-slip (zero velocity) for the bottom, left and right walls, imposed wall velocity at the top and free-slip at the front and back walls in order to mimic an infinitely deep domain.

As visible from Figure 3.7, the single-phase pseudo 2D case matches very well with the results presented by Ghia et al. [96].

The results are then expanded to a two phase case. In this case, two immiscible fluids with equal properties (*viz.* density, viscosity) are separated in the middle by an interface. Similarly to the previous single phase case, two walls (top and bottom) are moved with an equal and opposite velocity. The results from this simulation, presented in Figure 3.8b, are compared with two additional simulations: a case with a top and bottom moving lid and a solid wall in between (Figure 3.8a) and a case where there is no separation between the top and bottom lids (Figure 3.8c). Since the domain is relatively small with low velocities, surface tension dominates enough to maintain the interface between the fluids flat. As a consequence, the flow patterns of Figure 3.8b should be identical to the ones of Figure 3.8a, with two clearly defined vortices and with flow in one fluid unaffected by the other fluid. This does not happen in Figure 3.8c, where the system is influenced by both walls and a completely different flow pattern occurs. Indeed, the results of case b very well match the ones of case a, with minor differences due to the, unavoidable, small curvature of the interface.

Rayleigh-Taylor instability

To provide insights in the stability and convergence of the implemented numerical methods, the case of Rayleigh-Taylor instability is investigated. Four different grid resolutions were used, as shown in Figure 3.9, all describing a domain of 15 × 15 × 30 cm. The two fluids have a density ratio of 2. As visible from Figure 3.9, all different grid resolutions are able to describe the vortex formation, although with clear differences in accuracy. Moreover, all runs

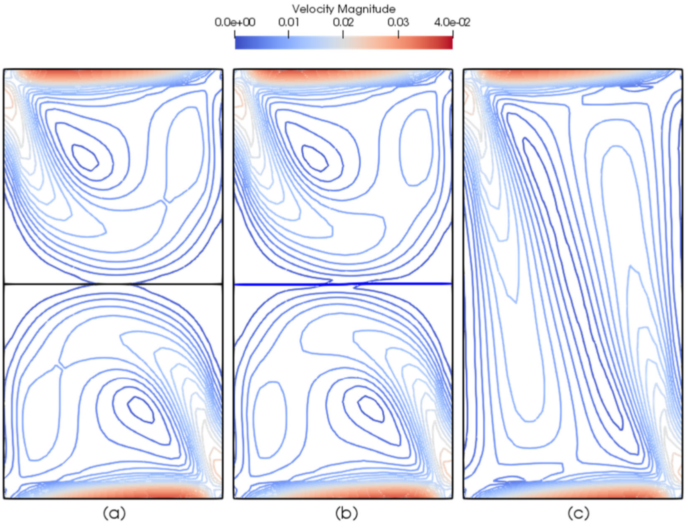

Figure 3.8: Velocity magnitude contours for fully developed flows: (a) two mirrored domains separated by a fixed wall (b) two immiscible fluids separated by an interface and (c) one single domain with one single fluid.

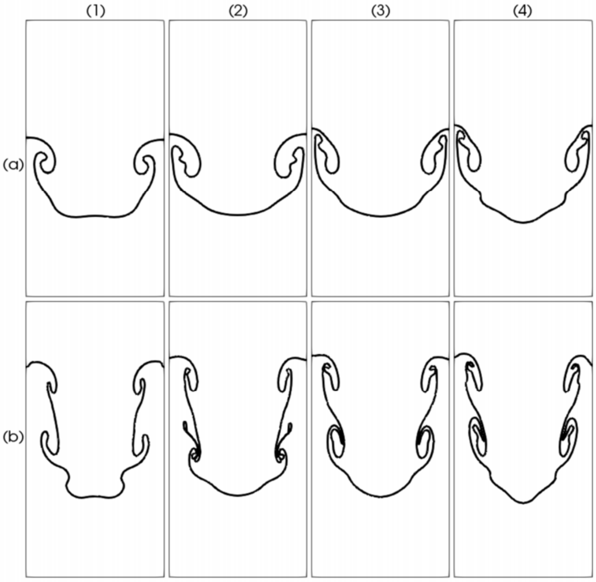

Figure 3.9: Rayleigh-Taylor instability at different grid resolutions. (a) Horizontal slice at the center of the domain; (b) diagonal slice corner to corner through the center of the domain. The numbers 1 to 4 represent increasing grid resolutions: (1) $30\times30\times60$; (2) $45\times45\times90$; (3) $60\times60\times120$; (4) $75\times75\times150$.

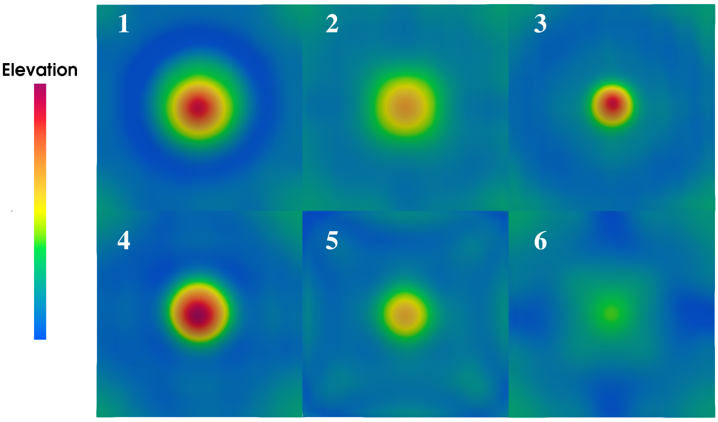

Figure 3.10: Effect of a single bubble on the free surface: **frame 1)** bubble approach, **frame 2)** bubble removal, **frame 3-4)** bubble wake rising, **frame 5-6)** interface relaxing.

were stable, although the resolution has a large impact on the performance. Interestingly, in Case 2 (visible especially in 2b) the interface does not create a vortex but rather a thin lip. The explanation is that this system is resolved enough to accurately capture the thin liquid finger visible in Case 3 and 4, but not enough to create a full vortex, instead letting the above liquid collapse onto itself. In addition, it is important to mention that a grid independent solution is not yet reached even with the finest grid. Nonetheless, such level of detail is not necessary for the purpose of this work, but rather it is possible to conclude that the interface is stable with significantly more complex shapes than what is expected of bubbly flows, for which the Front-Tracking method was originally conceived.

3.4 Results and discussion

The effect of the free surface on the system is now studied, first with single bubbles and subsequently with a multiphase disperse system.

3.4.1 Single bubble

A single bubble rising and colliding with the top interface is used in order to characterize the bubble-surface interactions and demonstrate the impact of the free surface on the flow. A small domain of $2.5 \times 2.5 \times 5$ cm with a resolution of $30 \times 30 \times 60$ is used, and a train of bubbles with a diameter of 4 mm is injected in the center at the bottom, with sufficient time between injections to neglect interactions. For the free surface, an additional top gas section of 2.5 cm is added, meaning the column height becomes 7.5 cm.

Surface deformation

The effect of a bubble approaching and rising through the free surface can be described in four distinct phases: 1) bubble approach, 2) bubble removal, 3) bubble wake, 4) relaxation, as shown in Figure 3.10. For the first step, as a consequence of the approaching bubble, the

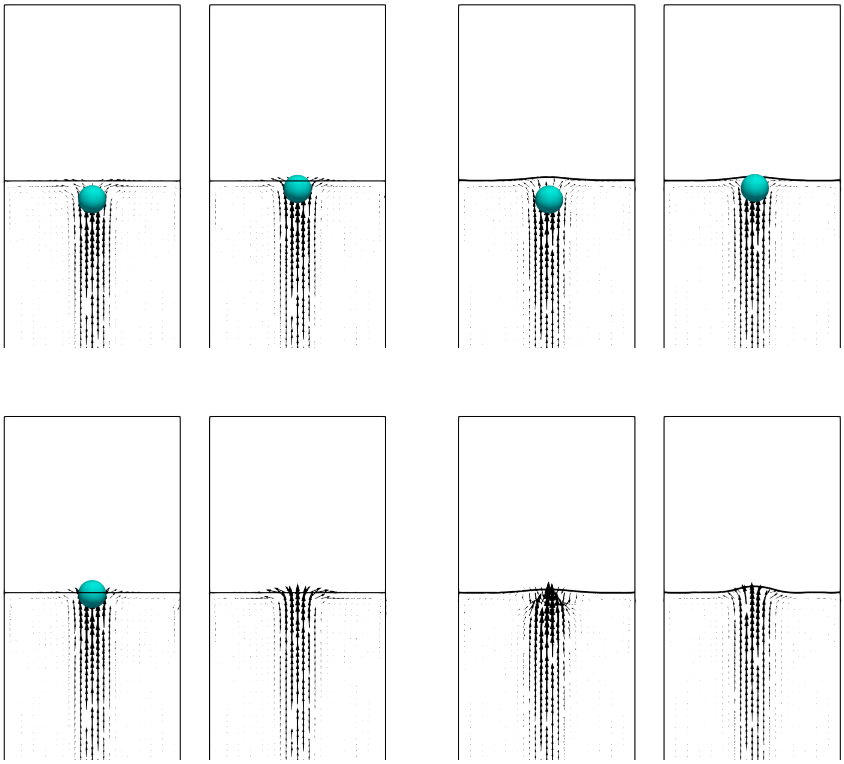

(b)

(b)

Figure 3.11: Four subsequent snapshots showing the liquid velocity vectors during a bubble approach to the top and subsequent removal. a) classic DBM and b) hybrid DBM-FT.

surface starts to move and deform. The surface starts rising in the center, due to the fact that the approaching bubble displaces a certain amount of liquid. The deformation of the surface increases until the bubble is removed: then the interface is quickly pulled down (second frame of Figure 3.10). Right after, the wake of the bubble imposes an additional rising motion to the surface, imposing a second rise in the center of the surface. Once the wake passes, the interface starts showing waves towards the sides which finally tend to normalize and relax the surface.

Bubble removal

The bubble removal (merging with the surface) has a net effect not only on the surface dynamics but also on the fluid velocity in the proximity of the merging location. With the original DBM boundary conditions, described for instance in Darmana et al. [8], the liquid shows increased shear stresses at the top boundary, because the flow cannot cross it and is rather diverted to the sides, with a free-slip boundary and fictitious holes to permit fluid inflow/outflow and conserve mass. This boundary condition does not alter the general flow pattern of the column, but rather influences the bubble size by increasing break-up rates at the top.

Figure 3.11 gives a better impression of the aforementioned phenomena. Here four snapshots are presented, for both the DBM with the classic boundary condition (on the left) and the hybrid DBM-FT (on the right). The four snapshots represent respectively the moment the bubble approaches the top boundary, the bubble touching the top boundary, the bubble merging with the top surface (crossing it for the classic DBM) and the relaxation of the surface after the bubble removal (or in general, after removal is done).

For the classic DBM, the approaching bubble shows larger lateral velocities nearby the surface, pushing the liquid to the side, towards the outflow holes. When reaching the top boundary, the velocity vectors increase their magnitude and point much more in the axial direction. Liquid then enters the domain through the inflow points when the bubble is removed.

For the DBM-FT, it is visible how the bubble pushes the free surface upwards, instead of pushing the liquid to the sides. This also causes the magnitude of velocities to be significantly lower, generating lower shear stresses in this region as compared to the classic DBM case. When the bubble is removed, the velocity field temporarily collapses and the interface is pulled down, to preserve the mass balance. In both cases, the bubble wake then causes the velocities to rise again in a similar way, causing dynamic movements of the free surface.

In addition, Figure 3.12 shows that the free surface also experiences waves formation when the flow develops further (*i.e.* when the second bubble is approaching the free surface). Indeed, small-scale velocity fluctuations generate dynamic larger waves at the free surface. Such fluctuations will then alter significantly the flow pattern in the proximity of the interface, with stronger upwards/downwards currents which affect the overall hydrodynamics. Nonetheless, it is noted that this case is significantly smaller than a common system such as the experimental case presented later. It is expected that effects of the bubble rising on the free surface and of the latter on the column hydrodynamics are less pronounced for larger columns.

Bubble break-up

As mentioned before, one of the issues of the fictitious DBM boundary condition for the top surface, is that higher shear stresses at this boundary result in higher break-up rates. This effect is clearly shown in Figure 3.13, highlighting the differences between the classic DBM and the DBM-FT as a result of the surface-induced bubble break-up caused by the fictitious high shear rates in the classic DBM.

Interestingly, break-up of a bubble can happen when a bubble is still in the domain (for instance when the bubble is crossing the top boundary but not yet fully removed), placing the small daughter bubble back in the domain with strong effects on the hydrodynamics, as can be discerned from the large velocity vectors in Figure 3.13. Here, the bubble breaks in two smaller daughters placing the smaller one in the domain, with consequences on the hydrodynamics at the top boundary. The novel free surface implementation does not

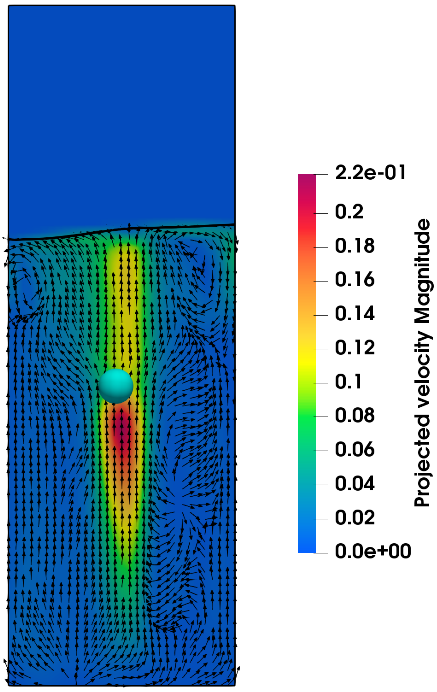

Figure 3.12: 2D projection of the velocity field of the DBM-FT showing waves formation, after several bubbles of the train reached the surface.

experience numerical break-up in the proximity of the surface, resulting in a much smoother velocity profile. Moreover, from the top view the effect of the side holes is clearly visible, which also generate much stronger downwards currents in the corners. As a final comment, a probable alternative to a free surface would be to simply restrict break-up in the top region of the DBM close to the surface, as the effect of the hydrodynamics on a larger system is expected to be negligible.

3.4.2 Bubble swarms

Having validated the use of the free surface implementation, it can be applied to a larger bubble column scenario. The DBM has been validated in the past with the experimental data of Deen [71], which is a representative scale for this type of models.

Numerical setup

The experimental data consist of a $15 \times 15 \times 45\,\mathrm{cm}$ rectangular column filled with water. Air bubbles, with an equivalent diameter of $4\,\mathrm{mm}$ are injected with a superficial gas velocity of $4.9\,\mathrm{mm\,s^{-1}}$ from 49 nozzles placed in a square pitch (distance between injection points

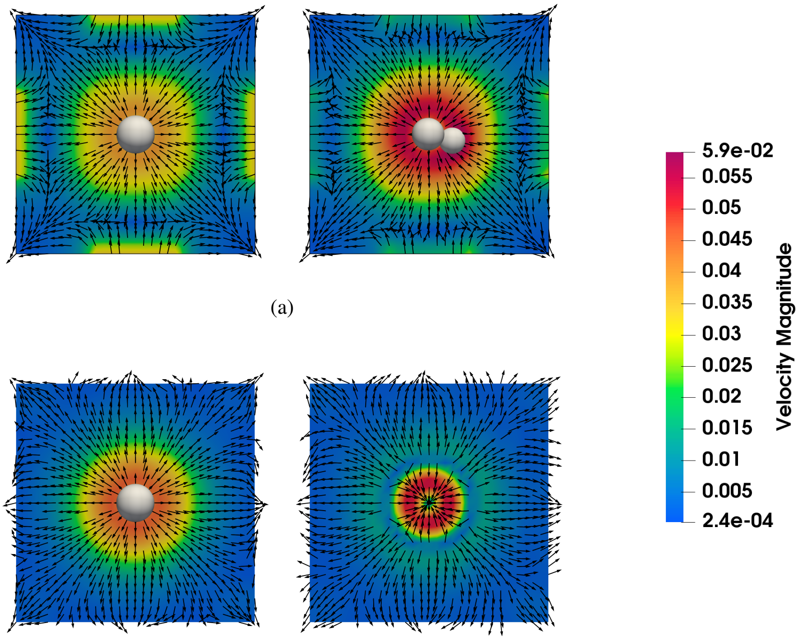

(a)

(b)

Figure 3.13: Top view of the velocity field in the proximity of the top boundary in two subsequent time steps: a) classic DBM and b) DBM-FT.

6.25 mm). An additional air layer is set on top of the liquid height for the DBM-FT simulation (reaching a total column height of 60 cm, with a liquid height of 45 cm). The simulation is carried out for 200 s and time averaged data are obtained, discarding the first 20 s of simulation.

The numerical setup has been already extensively described in the past (e.g. by Darmana et al. [8] and Lau et al. [15]) and a summary of the parameters is given in Table 3.2 and Table 3.3.

Table 3.2: Numerical settings for the Deen case [10].

Setting	Value	Units
Δt - flow	1×10^{-3}	s
Δt - bubble	5×10^{-5}	s
Averaging window	20-200	s
Grid size	0.005	m

Table 3.3: Simulation parameters for the Deen case [10].

Parameter	Value	Units
ρ_l	1000	$\mathrm{kg\,m^{-3}}$
ρ_g	1.25	$\mathrm{kg\,m^{-3}}$
μ_l	1×10^{-3}	Pa s
μ_g	1.8×10^{-5}	Pa s
σ	7.3×10^{-2}	$\mathrm{N\,m^{-1}}$
Domain	$0.15 \times 0.15 \times 0.45$	m
Superficial gas velocity	0.0049	$\mathrm{m\,s^{-1}}$

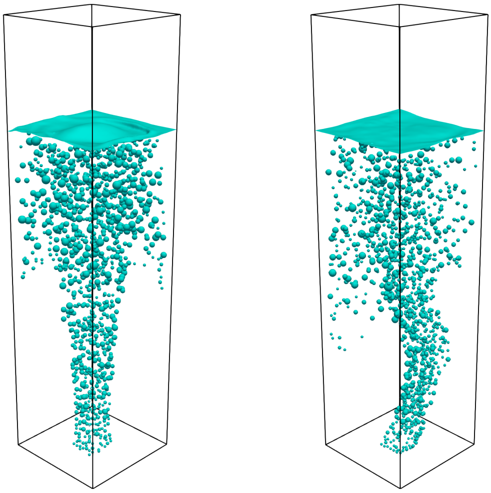
(a)

(b)

Figure 3.14: Snapshots of the DBM-FT simulations of Deen's case. a) startup ($t \approx 11$ s) and b) developed flow ($t \approx 75$ s).

Free surface behaviour

Figure 3.14 shows snapshots of Deen's case computed with the DBM-FT model with a free surface at the startup and when the flow is fully developed. The startup is characterized by a dynamic behaviour of the surface, first rising as bubbles are injected and with clear waves formation following the meandering of the bubble plume. As the flow develops, the region in the proximity of the surface becomes more homogeneous and the surface stabilizes. The surface itself remains mostly within one cell layer, with small waves formed due to bubbles removal.

Due to the injection of gas volume, the liquid height rises, which is visible in Figure 3.15a. The boundary for the classic DBM case is a fixed wall, which is located at a fixed height of

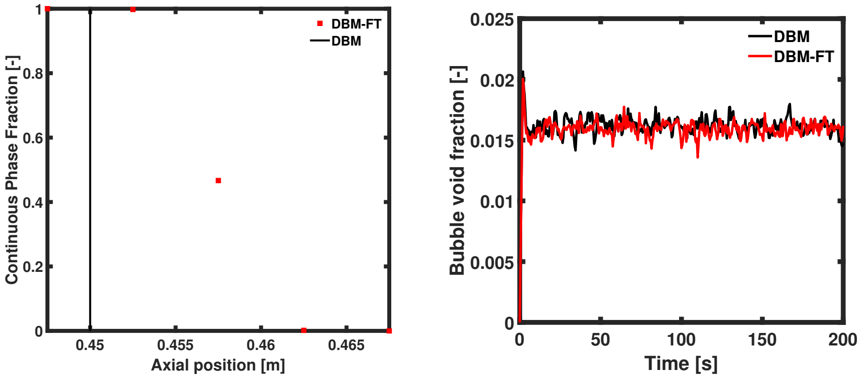

(a) (b)

Figure 3.15: (a) Time averaged continuous phase fraction and location of the DBM top boundary wall; (b) bubble holdup in the column over time.

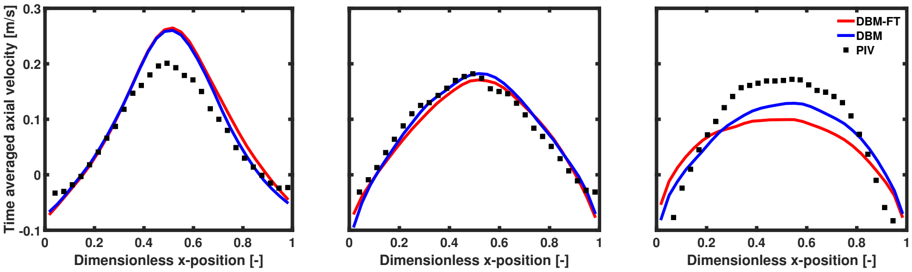

(a) (b) (c)

Figure 3.16: Time averaged axial liquid velocity in the center of the column and at three different heights: a) 0.15 m, b) 0.25 m and c) 0.35 m.

45 cm. The liquid height in the DBM-FT is located in the same position at startup, but due to the injection of bubbles it moves to an height of ≈ 45.75 cm, thus rising about 1.6% (or approximately two computational cells in the presented numerical setup).

The bubble holdup in the column and its temporal evolution, shown in Figure 3.15b, follows a very similar trend between the two cases, showing that the free surface has, as expected, a small influence on the system holdup and its temporal fluctuations. There is an initial spike due to the startup of the system in both cases, and than a stabilization at about 1.6% (exactly 1.59% for the DBM-FT and 1.62% for the DBM).

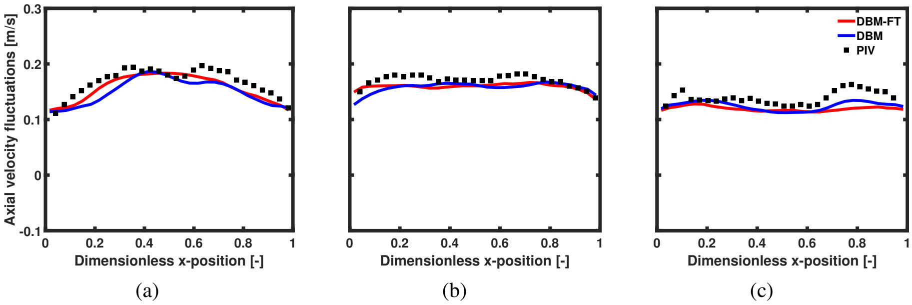

(a) (b) (c)

Figure 3.17: Time averaged axial liquid velocity fluctuations in the center of the column and at three different heights: a) 0.15 m, b) 0.25 m and c) 0.35 m.

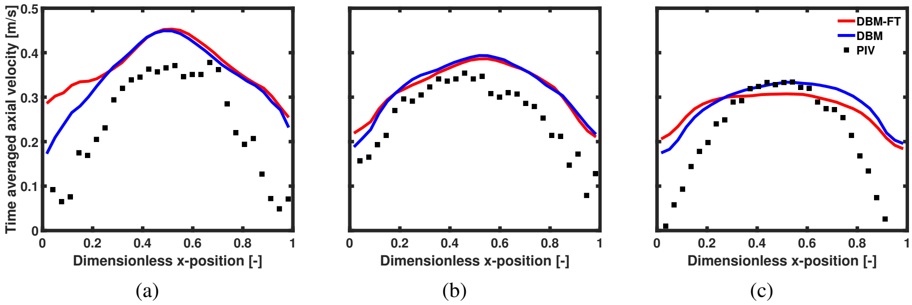

(a) (b) (c)

Figure 3.18: Time averaged axial bubble velocity in the center of the column and at three different heights:a) 0.15 m, b) 0.25 m and c) 0.35 m.

Liquid velocities

The time averaged axial liquid velocities are shown in Figure 3.16. At the height of 15 cm the model results do not differ, as the free surface is relatively far and its effect is unlikely to be present deep in the column. Both models clearly overestimate the liquid velocity at this height, as also reported in the literature by Lau et al. [5]. At the height of 0.25 m, still both models agree well with each other and this time very well with the experiments. A larger difference is found at the height of 0.35 m, where the influence of the boundary condition is more pronounced. Both models underestimate the liquid axial velocity compared to the experiments. Interestingly, the free surface case flattens the liquid velocity profile, as already was noticed for the single bubble case in Figure 3.11. Indeed, the general effect of the free surface is to dampen velocities in magnitude, avoiding the formation of steeper circulation patterns.

Interestingly, the axial velocity fluctuations are captured well by both models, as visible in Figure 3.17. Most probably, the effect of the free surface on these fluctuations is only visible at a closer proximity, and the influence of the interface is only visible in the macro-scale

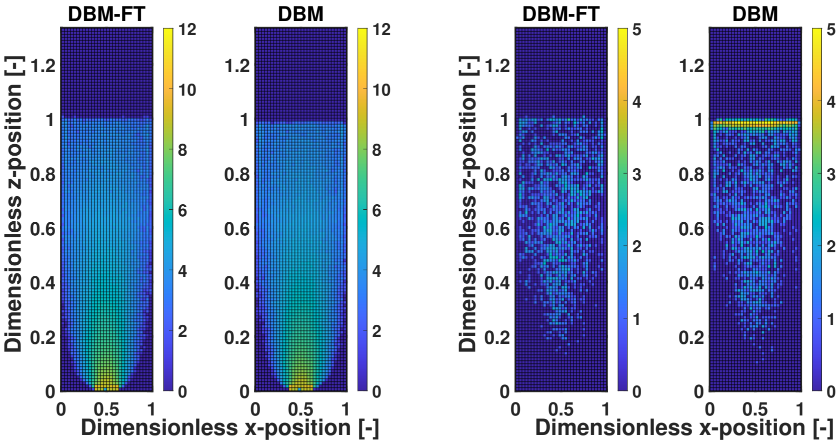

(a) (b)

Figure 3.19: Total numbers (natural logarithm) of break-ups and coalescence occurring in the DBM-FT (left) and the classic DBM (right, the domain ends at the height of 1). a) Natural logarithm of the total number of coalescence events and b) natural logarithm of the total number of breakups.

circulation patterns, presented in Figure 3.16.

Bubble velocity

The time averaged axial bubble velocities are shown in Figure 3.18. Noticeably, the bubble velocity is overestimated particularly at the walls. Both models show similar predictions of the bubble velocity until the top (35 cm). The largest discrepancies between experiments and simulations are at the side walls. One cause of the mismatch could be identified in the lift model: this would lead to an inaccurate prediction of the plume width and in turn influence the bubble velocity profiles. Another reason, especially for the profiles close to the bottom, is that the plume is narrow and less bubbles pass from the sides, meaning more statistical data might be necessary for accurate time averaging.

Coalescence and break-up rates

It has been mentioned that the presence of the fictitious boundary condition in the classic DBM to mimic the free surface overestimates the break-up rates at the top of the column as a consequence of the unphysically higher shear rates due to the liquid being diverted to the sides of the column.

In Figure 3.19 it is visible how, while coalescence is virtually unaffected by the presence of the free surface, break-up shows a large difference between the cases of the classic DBM and new DBM-FT. Indeed, coalescence happens mostly in the center of the plume at the bottom of the column, where bubbles are smaller and closer to each other leading to more

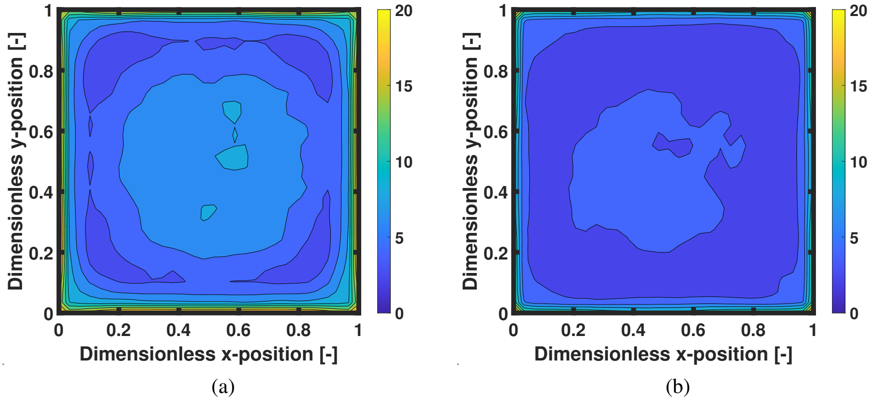

(a) (b)

Figure 3.20: Shear rates ($\left[\mathrm{s}^{-1}\right]$) at the top for a) the classic DBM and b) the novel DBM-FT.

frequent collisions and thus coalescence. On the other hand, break-up occurs mostly for larger bubbles when larger stresses are present. Visibly, in the case of the DBM a layer of break-up occurs in the proximity of the top boundary.

The shear rate can be written as the magnitude of the rate of strain tensor:

$$\dot{\gamma} = \sqrt{\frac{1}{2}(\dot{\gamma} : \dot{\gamma})} \tag{3.15}$$

where the rate of strain tensor is:

$$\dot{\boldsymbol{\gamma}} = \left(\nabla \mathbf{u} + (\nabla \mathbf{u})^T\right) \tag{3.16}$$

Figure 3.20 shows the shear rate at the top of the column for both the classic DBM and the DBM-FT case, indeed demonstrating higher shear rates and increased break-up rates for the classic DBM.

3.5 Conclusions

The hybrid DBM-FT model has been developed and thoroughly validated with a variety of verification cases and the experimental results of Deen [71]. The kinematic and dynamic conditions of the free surface are respected, and the numerical representation of the surface is very stable even for highly deformed structures as seen for the Rayleigh-Taylor instability case.

The effect of the treatment of the free surface both for single bubbles and Deen's case is clearly observed in the immediate proximity of the free surface, where reduced shear rates and velocity magnitudes are observed for the novel free surface implementation in the DBM-FT model. Despite these observations, the general effect of the free surface on the overall hydrodynamics is pronounced only in the top part of the column, where it influences the overall circulation patterns, and particularly the bubble break-up rates.

Concluding, the novel DBM-FT implementation for the free surface can be used as a good starting point for further studies where the free surface has a larger impact, as for instance for narrow columns. In addition, because of the nature of Front-Tracking compared to Volume of Fluid methods (particularly the avoidance of numerical coalescence), it can be applied when studying foams, perhaps including the relevant merging physics with the top surface. In addition, large bubbles in heterogeneous flow regimes can be transferred to Front-Tracking bubbles (similarly to Li et al. [31] for VOF) in order to better capture shape changes and avoid typical problems of Euler-Lagrange models when bubbles become much larger than the grid.

CHAPTER

4

EULER-LAGRANGE MODELING OF BUBBLES FORMATION IN SUPERSATURATED WATER *

Phase transition, and more specifically bubble formation, plays an important role in many industrial applications, where bubbles are formed as a consequence of prevailing chemical reactions, such as in electrolytic processes or fermentation. Predictive tools, such as numerical models, are thus required to study, design and optimize these processes. This chapter aims at providing a meso-scale modeling description of gas-liquid bubbly flows including heterogeneous bubble nucleation using a Discrete Bubble Model (DBM), which tracks each bubble individually and which has been extended to include phase transition. The model is able to initialize gas pockets (as spherical bubbles) representing randomly generated conical nucleation sites, which can host, grow and detach a bubble. To demonstrate its capabilities the model has been used to study the formation of bubbles on a surface as a result of supersaturation. Higher supersaturation results in a faster rate of nucleation, which means a larger number of bubbles in the column. A clear depletion effect could be observed during the initial growth of the bubbles, due to insufficient mixing.

---

*This chapter is based on: Battistella, Aelen, Roghair, van Sint Annaland (2018) [84]

4.1 Introduction

Phase transition as a consequence of supersaturation occurs in a variety of natural and industrial processes. A well-known example is opening a bottle of soda: the sudden change in pressure creates a local supersaturation and bubbles form on the surface of the bottle. Another mechanism to obtain local supersaturation is when a reaction produces gas in excess. Relevant industrial applications are in electrolytic processes where gas (such as H_2 in the electrolysis of brine) bubbles are formed on the electrodes [34, 35], carbonated beverages [97], molten polymers [98] and even bubbles in oil reservoirs [99]. Computational Fluid Dynamics (CFD) models describing the hydrodynamics of a system where bubbles are formed are thus very relevant for industry, but their capabilities are often too limited in practice.

Eulerian-Eulerian models typically include a gas generation term as a boundary condition and information about the bubble sizes can be obtained through the implementation of a nucleation rate in a Population Balance Model (PBM) [36]. Examples of the use of these models can be found in the context of electrochemical reactions, where gasses are produced on electrodes. For instance, Liu et al. [100] used the Two Fluid Model to simulate the electrochemical oxidation of *p*-methoxyphenol, while El-Askary et al. [101] simulated the production of hydrogen in an electrochemical cell. On the other hand, detailed Direct Numerical Simulations (DNS) models are limited by their computational cost. Liu et al. [37] used a Volume of Fluid (VOF) model to simulate a single gas bubble growing in the water electrolysis process. In their study, they noted the strong analogy between boiling and bubble formation in supersaturated liquids. Many studies have been carried out investigating boiling flows, especially using VOF [102, 103] and Lattice-Boltzmann methods [104], but a comprehensive overview goes out of scope of this work. Regarding supersaturation, DNS methods have been applied for instance by Liu et al. [37], but it is possible to even find detailed Molecular Dynamics (MD) simulations of nano-bubbles nucleation by Weijs et al. [105].

In the framework of multi-scale modeling, for instance presented by [4], the meso-scale remains important to close the gap between the large- and micro-scales. In literature, to the knowledge of the author, not many authors have studied bubble nucleation at the meso-scale. Mandin et al. [106] introduced a Lagrangian tracking for a vertical electrode, but the gas injection was modeled based on a given mass flow rate. Nierhaus et al. [107] used a two-way coupled Euler-Lagrange model to study hydrogen bubble formation in a rotating electrode configuration. In their work they applied at the gas inlet a pre-defined bubble size distribution obtained from experimental data. In their group, they subsequently improved the model: first, van Parys et al. [108] introduced a model of bubble growth on a surface by supersaturation, and thereafter, van Damme et al. [109] extended the model with nucleation sites, although the detachment radius was fixed in their simulations. More recently, Hreiz et al. [110] used the Euler-Lagrange model of ANSYS Fluent to simulate a vertical electrode. They treated the nucleation sites as injection points, recognizing in their work that a more sophisticated approach for bubble nucleation/injection in the system is required to capture the nucleation dynamics. The novelty of this work lies in a novel nucleation algorithm which considers discrete nucleation sites with distinct properties, and links it to the hydrodynamics of the Euler-Lagrange model and to the classical nucleation theory, as an improvement of the work by van Damme et al. [109]. This model enables improving the fundamental understanding on bubble nucleation rates at the meso-scale, obtaining information on bubble sizes, nucleation rates and growth rates.

The aim of this work is thus to develop an Euler-Lagrange model to simulate bubbly flows at the meso-scale where phase transition via supersaturation occurs. In the following sections, the developed model and the numerical setup will be described and verified. Then, results of a number of demonstration simulations on bubble formation due to supersaturation by heterogeneous nucleation are described to illustrate the model's capabilities.

4.2 Model description

The Discrete Bubble Model (DBM) is an Euler-Lagrange type CFD model, based on the work of Delnoij et al. [14], subsequently expanded and improved by Darmana et al. [8] and Lau et al. [15]. Newton's laws of motion are used to track each individual bubble, while accounting for bubble-bubble interactions (collisions, coalescence and breakup), mass transport and in this work also phase transition. A detailed description of the model will be given in the following sections. For more details the interested reader is referred to the cited works [14, 8, 15].

4.2.1 Liquid dynamics

The fluid flow is described by the volume-averaged Navier-Stokes equations:

$$\frac{\partial}{\partial t}\left(\rho_l \alpha_l\right) + \nabla \cdot \rho_l \alpha_l \mathbf{u} = \dot{M} \tag{4.1a}$$

$$\frac{\partial}{\partial t}\left(\rho_l \alpha_l \mathbf{u}\right) + \nabla \cdot \left(\rho_l \alpha_l \mathbf{u}\mathbf{u}\right) = -\alpha_l \nabla p + \alpha_l \rho \mathbf{g} + \nabla \cdot \alpha_l \boldsymbol{\tau}_l + \boldsymbol{\Phi} \tag{4.1b}$$

where $\mathbf{u}$ is the fluid velocity, α_l denotes the liquid fraction, $\boldsymbol{\Phi}$ represents the momentum coupling between the liquid and the discrete gas phase and $\dot{M}$ the volumetric mass exchange rate. Note that, compared to Chapter 3.2.1, here the continuity equation (Equation 4.1a) is written in the compressible form with the addition of a mass transfer term. In this equation, $\boldsymbol{\tau}$ represents the stress tensor, which has been described in Chapter 3.2.1 for Newtonian fluids and includes the contribution of the LES sub-grid scale turbulent viscosity.

4.2.2 Bubble dynamics

With Newton's laws of motion, each bubble is tracked accounting for the different forces acting on it. The motion of the bubbles can be described with:

$$\rho_b V_b \frac{d\mathbf{v}}{dt} = \sum \mathbf{F} - \left(\rho_b \frac{dV_b}{dt}\right) \mathbf{v} \tag{4.2a}$$

$$\frac{d\mathbf{x}_b}{dt} = \mathbf{v} \tag{4.2b}$$

where $\mathbf{v}$ represents the bubble velocity and $\mathbf{x}_b$ its position in the 3D domain. The following forces on the bubbles are accounted for: buoyancy, drag [6, 7], lift [86], virtual mass [87] and wall-interactions [88], as given by Equation 4.3:

$$\sum \mathbf{F} = \mathbf{F}_G + \mathbf{F}_P + \mathbf{F}_D + \mathbf{F}_L + \mathbf{F}_{VM} + \mathbf{F}_W \tag{4.3}$$

An overview of the different closure relations used for the forces is given in Table 3.1. These closures were selected following the work of Lau et al. [15] and have been used in several works, within our group [15, 8, 111] as well as others [112, 81, 113]. The interphase two-way coupling is performed through a polynomial mapping in order to map quantities between the Eulerian grid and the Lagrangian bubbles. The chosen technique is a clipped fourth-order polynomial following the work by Deen et al. [3].

An important aspect is the volume change due to the interphase mass transfer. This is accounted for as:

$$\rho_b \frac{dV_b}{dt} = \dot{m} \tag{4.4}$$

It is relevant to note that the virtual mass force should account for the contribution of the changing volume of the bubble, $\rho C_{VM} dV_b/dt(\mathbf{u}-\mathbf{v})$, as described by Magnaudet and Eames [114]. This contribution is important even when the relative velocity does not change with time, if the bubble is shrinking or growing. In the present work, this contribution has been neglected as the main purpose is the demonstration of the nucleation model. Moreover, the fastest rate of volume change happens when the bubble is still attached to the surface. In this case, forces are not calculated, as will be explained further in section 4.2.5, which allows to safely exclude this term for these bubbles. However, when the bubble is freely rising in the column, the contribution becomes of the same order of magnitude as the drag force for the fastest growing bubbles, which implies that this term should not be omitted and has to be included in future works, despite the fact that the majority of the bubbles are not growing as fast.

More details on the gas-liquid mass exchange rate will be given in the following sections.

Bubble interactions

As mentioned in the previous section, bubble collisions, coalescence and breakup have been taken into account in the model. The position, velocity and size of each bubble is already available as it is obtained during the simulation, allowing for an easy detection of binary encounters with other bubbles or with the wall. The collision model used in this work is based on the hard-sphere approach of Hoomans et al. [89] and its adaptation from Delnoij et al. [14], where collisions are event-based and are considered as perfectly elastic. To speed up the calculation routines, a neighbor list concept as described by Darmana et al. [8] is used. When bubbles are colliding (assuming bubbles i and j collide, as visible in Figure 4.1), the tangential velocity component (v_i^T) remains unchanged, while the normal velocity component after collision (v_i^{N*}) is calculated as:

$$\mathrm{v}_i^{N*} = 2\frac{m_i \mathrm{v}_i^N + m_j \mathrm{v}_j^N}{m_i + m_j} - \mathrm{v}_i^N \tag{4.5}$$

When the collision is evaluated, the size change of the bubble as a result of mass transfer needs to be accounted for. In the cases considered in this chapter, the supersaturation of the liquid sometimes results in faster rates of bubble growth than the velocity of the bubble itself. Two bubbles that are slowly moving apart could still collide if their sizes are growing fast. To

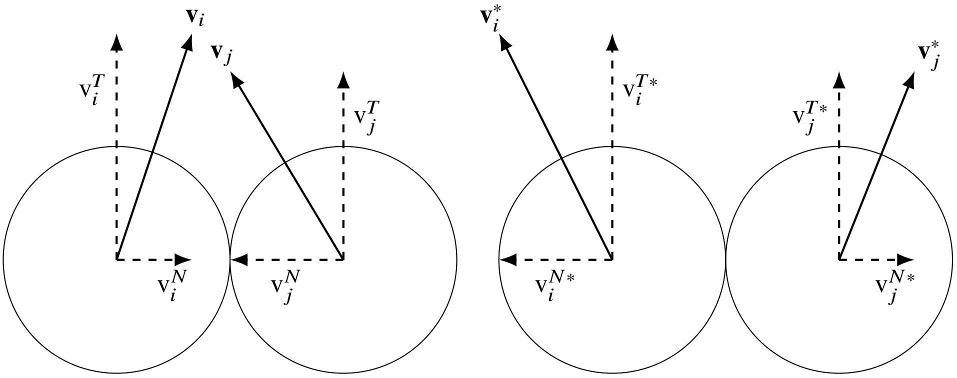

(a) Before collision (b) After collision

Figure 4.1: Schematic representation of the collision process for two bubbles of the same mass (here depicted in 2D for clarity).

accurately resolve these situations, the bubble size rate of growth $\dot{R}$ has been included in the impulse calculation for the collision [8].

In addition to elastic collisions, bubbles can coalesce and merge into a bigger one when in contact for enough time. Many theories and models exist for bubble coalescence (see Lau et al. [15]). In this work, the film drainage model as implemented by Darmana et al. [8] is used. Two colliding bubbles trap a thin film of liquid between them, which can drain over time. If the two gas elements are in contact for sufficiently long time, it will completely drain allowing coalescence. This can be modelled with:

$$t_{\text{contact}} \geq t_{\text{drainage}} \tag{4.6}$$

Prince and Blanch [115] calculated the drainage time as:

$$t_{\text{drainage}} = \sqrt{\frac{d_{eq}^3 \rho_l}{128\sigma}} \ln \frac{\theta_0}{\theta_f} \tag{4.7}$$

where θ_0 and θ_f represents respectively the initial and final film thickness during the drainage process, which are equal to 1×10^{-4} m and 1×10^{-8} m respectively [8]. The contact time of the two bubbles is calculated through the correlation proposed by Sommerfeld et al. [18], assuming that it is proportional to a deformation distance divided by the normal component of the absolute relative velocity of the two bubbles, as described by Equation 4.8:

$$t_{\text{contact}} = \frac{C_{\text{co}} d_{\text{eq}}}{2\left|\mathrm{v}_i^N - \mathrm{v}_j^N\right|} \tag{4.8}$$

The deformation distance is in essence the distance that the two centers of mass cover starting from the sum of the two radii (zero deformation, perfect spheres) when bubbles deform. Since deformation is difficult to quantify, it is calculated as a fraction of the equivalent diameter. Indeed, the coalescence constant (C_{co}), which is set to a value of 0.5, represents the deformation distance normalized by the effective bubble diameter and should be treated as a calibration parameter. For a detailed description of the deformation process, the reader is referred to the work of Sommerfeld et al. [18]. When both the film drainage and contact time are calculated, with Equation 4.6 it is possible to distinguish between simple elastic collision or coalescence, i.e. at the step of Figure 4.1a. In the latter eventuality, the resulting bubble will have a volume, or mass as it is considered as incompressible, equal to the sum of the two parents.

Bubbles rising in a liquid can also break as a consequence of various factors, such as turbulent fluctuations, viscous shear stress, surface instabilities *etc.* [90]. The break-up model implemented in the DBM is based on the work of Lau et al. [15]: this model assumes that break-up occurs when the inertial forces acting on the bubble (which deform the bubble) are larger than the surface tension force. Based on a force balance, a critical Weber number is used as a criterion for the break-up of spherical bubbles:

$$\mathrm{We} = \frac{\rho_l \overline{\delta u^2(d)} d_{\mathrm{eq}}}{\sigma} \geq 12 \tag{4.9}$$

where $\overline{\delta u^2(d)}$ represents the mean square velocity difference at the distance of the bubble diameter [15]. The break-up is considered to be binary, forming only two daughter bubbles with a size taken from a U shaped daughter size distribution. The resulting bigger bubble is assigned the parent's original position while the smaller is randomly placed around the other, at a distance of 1.1 times the sum of their radii, preventing overlap and immediate coalescence of the two daughter bubbles (see Lau et al. [15]).

4.2.3 Species transport and mass transfer

The Discrete Bubble Model includes the species transport equations accounting for mass transfer and chemical reaction. A transport equation for each species is implemented on the same Eulerian grid as:

$$\frac{\partial}{\partial t}\left(\alpha_l \rho_l Y_l^j\right) + \nabla \cdot \left(\alpha_l \left(\rho_l \mathbf{u} Y_l^j - \Gamma_{\mathrm{eff}}^j \nabla Y_l^j\right)\right) = \dot{M} + \alpha_l S^j \tag{4.10}$$

where Y_l^j represents the mass fraction of component j in the liquid phase, S^j is its source/sink term accounting for chemical reactions, $\dot{M}$ represents the net volumetric mass transfer rate between the phases and Γ_{eff} is the effective dispersion coefficient, calculated as:

$$\Gamma_{\mathrm{eff}}^j = \rho_l \mathcal{D}_l^j + \frac{\mu_T}{\mathrm{Sc}_T^j} \tag{4.11}$$

In Equation 4.11, the turbulent Schmidt number is approximated to $\mathrm{Sc}_T^j = 1$ [111]. Equation 4.10 is solved for $N_S - 1$ components. The last component, usually the solvent (e.g. water), is evaluated by enforcing the summation equation:

$$\sum_{j=1}^{N_S} Y_l^j = 1 \tag{4.12}$$

The physical properties of the mixture are calculated as the weighted average of each specie. The interphase mass transfer rate is a function of the concentration difference between the bubble (assumed to be composed entirely of one gas, namely CO_2, thus neglecting evaporation of the liquid) and the liquid. This has been expressed by [8] as:

$$\dot{m}_b^j = k_l^j A_b \rho_l \left(Y_l^{j*} - Y_l^j \right) \tag{4.13}$$

The mass transfer coefficient is determined by a Sherwood relation valid for spherical gas bubbles [64]:

$$\mathrm{Sh} = 2 + 0.6415(\mathrm{ReSc}^j)^{1/2} \tag{4.14}$$

The gas side mass fraction is calculated from the Henry constant:

$$Y_l^{j*} = H^j Y_b^j \frac{\rho_b}{\rho_l} \tag{4.15}$$

The transport equation is discretized implicitly (with a semi-implicit source term for the reaction) on the Eulerian grid and the resulting linear system is solved using a biconjugate gradient method implemented in the scientific library PETSc [93, 94].

4.2.4 Verification

The hydrodynamics of the DBM has been validated in the past by Lau et al. [15], with the use of experimental data from a square bubble column, performed by Deen [71]. On the other hand, the species solver has been modified since Darmana et al. [8] and a verification with benchmark analytical cases is required to assess the numerical validity of the results. A few unidirectional verification cases have been performed, as will be detailed in the following sections.

1D convection-diffusion

In this case, a unidirectional flow in the domain is considered where the concentration of the component of interest is initially zero. The density is assumed constant. A flow from one side (where the mass fraction is $Y_l = 1$) is started and diffusion takes place. Equation 4.10 simplifies to:

$$\frac{\partial c}{\partial t} + u \frac{\partial c}{\partial x} = \mathcal{D} \frac{\partial^2 c}{\partial x^2} \tag{4.16}$$

The analytical solution for this system has been derived by Ogata and Banks [116] as:

$$\frac{c}{c_0} = \frac{1}{2} \left[\mathrm{erfc} \left(\frac{x - ut}{2\sqrt{\mathcal{D}t}} \right) + \exp\left(\frac{ux}{\mathcal{D}} \right) \mathrm{erfc} \left(\frac{x + ut}{2\sqrt{\mathcal{D}t}} \right) \right] \tag{4.17}$$

In Figure 4.2a it is shown that the grid resolution plays an important role (due to the well known numerical diffusion) but the solver approaches very well the analytical solution at sufficiently high number (200 in this case) of grid elements. As visible from Figure 4.2b, the error reduces linearly when increasing the number of grid sizes.

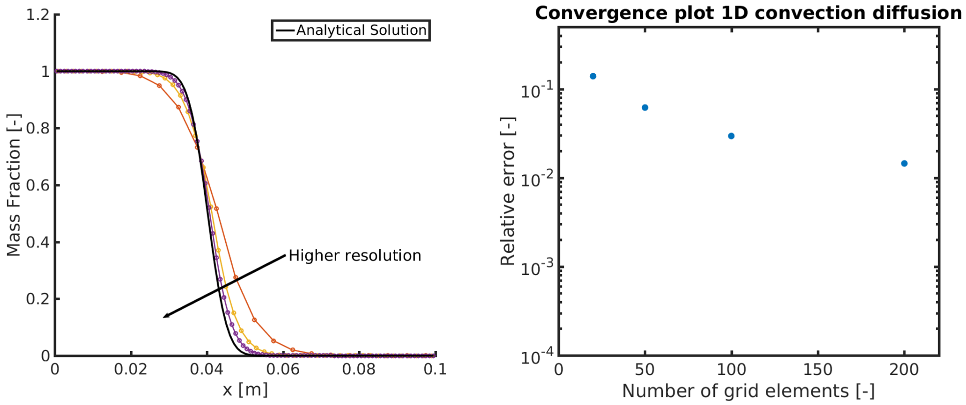

(a) (b)

Figure 4.2: Comparison of the DBM species solver with the analytical solution for a unidirectional convection-diffusion flow, for different grid resolutions. (a) Analytical vs simulations data: the analytical solution is represented by the black line. (b) L2-norm relative error vs grid elements

Batch reaction

In order to verify the correct implementation of the semi-implicit discretization for the source/sink term and mass transfer, a simple reaction $A \longrightarrow B$ is implemented with a first and a second order kinetics, assuming an ideally mixed batch reactor. In this case, Equation 4.10 simplifies to:

$$\frac{dc}{dt} = R = \begin{cases} -k_R c & 1^{st} \text{ order reaction} \\ -k_R c^2 & 2^{nd} \text{ order reaction} \end{cases} \tag{4.18}$$

where k_R represents the reaction rate. Integration of Equation 4.18 yields to the analytical solutions:

$$c = \begin{cases} c_0 \exp(-k_R t) & 1^{st} \text{ order reaction} \\ \frac{1}{1/c_0 + k_R t} & 2^{nd} \text{ order reaction} \end{cases} \tag{4.19}$$

As shown in Figure 4.3, the DBM results match very well with the analytical solutions.

4.2.5 Phase transition

Theoretical overview

An important concept is supersaturation: a liquid is (locally) supersaturated when the concentration c is higher than the equilibrium concentration c_s, which can be expressed, for instance, by Henry's law as done in Equation 4.15. A relevant parameter, called the *supersaturation ratio*, is introduced as [117]:

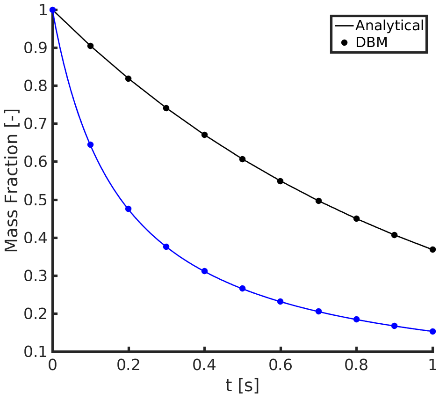

Figure 4.3: First (top line) and second (bottom line) order reactions in a batch reactor: comparison with the analytical solutions.

$$\zeta = \frac{c}{c_s} - 1 \tag{4.20}$$

It indicates that, for phase transition to occur, $\zeta > 0$. Equilibrium between the two phases exists when this ratio is equal to 0.

The mechanism of a gas bubble formation has been a topic of investigation for many years [118]. Two different macro classes are generally distinguished: homogeneous and heterogeneous nucleation. In their review, Jones et al. [118] identifies four different types of bubble nucleation mechanisms:

Type I: The classical homogeneous nucleation, i.e. the spontaneous creation of a bubble in the liquid bulk. This mechanism is characterized by the high energy requirements to form a new gas-liquid interface and the necessity to have enough gas molecules in close proximity to each other. For these reasons, only a system which exceeds a supersaturation ratio of 100 is able to form bubbles, which is extremely large. For example, for common drinks like soda and champagne, ζ typically ranges from 2 to 5, which would mean it is impossible to have Type I nucleations for such systems [117, 97].

Type II: The classical heterogeneous nucleation. This mechanism assumes that the new interface is created in small cavities or imperfections at a solid surface (such as a wall or suspended impurities). However, a new interface still has to be created, so that supersaturation levels comparable with homogeneous nucleation are required.

Type III/IV: Pseudo-classical and non-classical nucleation respectively. These two types represent the vast majority of the nucleation events in liquids with low supersaturation. Both mechanisms account for a pre-existing gas pocket, for instance as a consequence of another type of nucleation event (e.g. type II) or simply because of the inability of the liquid to fully fill cavities on a surface. The difference between these two types lies in the geometry of the cavity. It is worth mentioning that the energy requirement for both

> types is respectively low and zero, meaning that type IV is the one responsible for the long term cycle of bubble production in carbonated drinks. In this case, the production of bubbles will continue until the critical radius, increasing as a consequence of the depletion of gas in the liquid, reaches a value equal to the radius of the cavity meniscus and thus nucleation stops.

As introduced in the previous paragraph, the size of the nucleation site is crucial in describing the formation and growth of a bubble for the case of the most common mechanism type IV. Only nucleation sites with a radius larger than a critical value [118] (related to the Laplace pressure) can host a growing bubble. This radius represents the minimum size for a bubble to be able to grow by mass transfer, without dissolving back into the liquid, and is defined as:

$$R_c = \frac{2\sigma}{p_s \zeta} \tag{4.21}$$

where σ and p_s represent the surface tension coefficient and the saturation pressure of the gas respectively. In addition, there is a second property influencing bubble formation: the depth of the nucleation site with respect to its width/radius. As mentioned before, while pouring the (supersaturated) liquid into a vessel, flask or glass, a liquid front will move across the solid surface and encounter holes and gaps. If the liquid manages to reach the bottom of this hole before any liquid reaches the other side, gas will be expelled from this site turning it into a nucleation site for type II nucleation. If, however, this liquid does not manage to reach the lowest point in time, gas will become trapped within this site and facilitate type III or IV nucleation depending on the value of R_c at that moment in time. The last property of the surface influencing the nucleation process is the hydrophobicity of the substrate. Water based substances moving across a hydrophilic substrate will have a very shallow contact angle. This will result in these liquids to favour following the contours of the substrate, leaving less gas pockets (nucleation sites) in their wake.

The implementation of phase transition in the DBM can be divided into three different parts: initialization, nucleation and detachment. Once a bubble is detached, it will be resolved as a standard Euler-Lagrange simulation as described in the previous sections.

Initialization

Nucleation cavities present on all substrate samples have a variety of shapes and sizes. Due to the limitations on complexity on the boundary only rudimentary shapes can be set as nucleation sites. For this reason it was opted to simply represent all nucleation sites as small conical cavities due to their simple geometry and the more available literature, thus making them a good starting point on which to further expand in later works using more complex geometries (rounded sites, elongated crevices, *etc.*), if deemed necessary. All nucleation sites are distributed randomly across the nucleating boundary wall (see Figure 4.4) with a site radius (R_{site}) taken from a Gaussian distribution. The depth (d) is taken as a random value ($0.5R_{\text{site}} < d < 1.5R_{\text{site}}$). This has been selected to represent a general surface. To describe actual real surface, experimental data to correlate properties such surface roughness to the number of nucleation sites is necessary. An experimental setup has been constructed

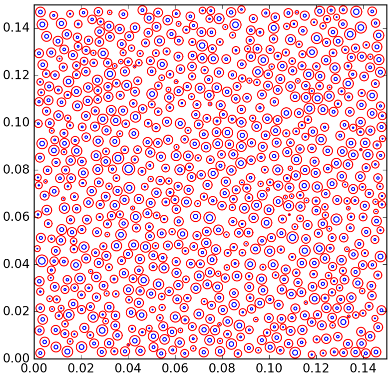

Figure 4.4: Top down view of the x-y plane containing randomly distributed nucleation sites. The blue circles represent the actual size of the nucleation site, whereas the red circles are representing the expected maximum growth.

(based on the work by Enríquez et al. [117]), to obtain data on the nucleation site density from real surfaces, described in Chapter 5. The sites are placed in such a way that the minimum distance between each site is 1.5 times the maximum expected growth to prevent overlap of nucleating bubbles.

As was noted in the review by Jones et al. [118], only cavities containing a gas pocket are able to form bubbles in fluids with a low to moderate supersaturation ratio (see Section 4.2.5, type III and IV). In order for such a cavity to hold any gas, it needs to be entrapped by the moving liquid closing the cavity mouth before all of the gas has been pushed out by the moving liquid front, or alternatively to host a type I or II nucleation event. In a study investigating this phenomena, Bankoff [119] linked the entrapment to the contact angle of the approaching liquid, noting that a highly wetting liquid ($\theta \approx 0$) will always lead to the full expulsion of any gas present in the cavity. The simple condition presented relies on the liquid's surface tension and capability of keeping a highly rounded cap. This cap will, under the right conditions (Equation 4.22), entrap gas at the bottom of a cavity with a cone angle ϕ.

$$2\phi > \theta \tag{4.22}$$

This condition, however, assumes that the cavity walls are completely smooth and thus may differ from similarly sized cavities during nucleation experiments when the contact-angle of the liquid is very close to the half angle of the cavity.

When the DBM is initialized, the condition given by Equation 4.22 is used to determine whether a given cavity holds a gas pocket or not. This pocket is formed at the exact moment when the liquid front reaches the opposite side of the site mouth: it is thus possible to define the exact entrapped gas volume as shown by Tong et al. [120]. This gas volume V_g (Equation 4.23) can subsequently be used to calculate the gas pocket radius of curvature R_p, for the entrapped gas within the cavity (Equation 4.24). An artificial bubble attached to the

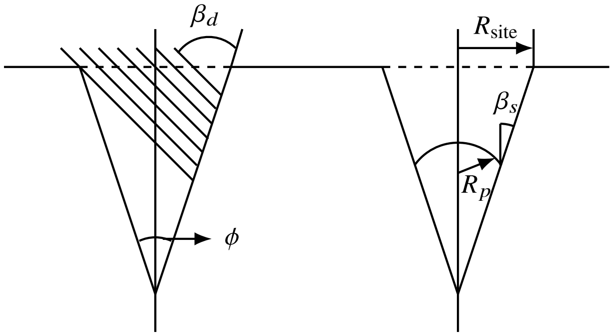

Figure 4.5: Visualized parameters for Equations 4.23 and 4.24, redrawn from Tong et al. [120]

surface is thus generated, with a volume of gas equal to the gas pocket. The radius of the generated bubble is thus calculated from the volume assuming spherical shape and it is thus not equal to the radius of curvature. This artificial bubble serves as a place-holder for the gas pocket, basically behaving like an embryo bubble for the subsequent nucleation phase.

$$V_g = \frac{\pi R_{\text{site}}^3}{3} \frac{\sin(\beta_b - 2\phi)\left[\frac{\tan(\phi)}{\tan(\beta_b - \phi)}\right]^2}{\sin(\phi)\sin(\beta_b - \phi)\left[1 - \frac{\tan^2(\phi)}{\tan^2(\beta_b - \phi)}\right]^{2/3}} \tag{4.23}$$

$$R_p = \frac{1}{\pi} \frac{3V_g}{\frac{\cos^3(\beta_s - \phi)}{\tan(\phi)} + \left[2 - 3 - \sin(\beta_s - \phi) + \sin^3(\beta_s - \phi)\right]} \tag{4.24}$$

The dynamic contact-angle β_d is a property of the liquid-substrate pair, as well as the liquid-cavity contact angle of the gas embryo β_s. β_d has been imposed equal to 90°, to avoid hydrophilicity/hydrophobicity effects. Due to very limited data in this field, the inter cavity contact angle is difficult to be estimated for liquids which are not highly wetting. It was therefore decided to choose an average value of 30° for all liquids until more detailed information becomes available.

Nucleation

During each time step all nucleation sites not currently nucleating bubbles are checked for their ability to perform nucleation. This is accomplished by firstly interpolating the dissolved gas phase concentration from the Eulerian grid to the nucleation site. Thus, a local supersaturation ratio is calculated at the center of the nucleation site, which allows the calculation of the critical radius, as defined in Equation 4.21. A bubble equal to the gas pocket embryo will be created at the nucleation point if the critical radius is greater than the radius of curvature of the site, calculated through Equation 4.24. This bubble is artificially kept in place during the nucleation and growth, until its detachment. Any nucleation site not able to perform a nucleation event due to a local insufficient supersaturation will be skipped until the amount of dissolved gas at the nucleation site becomes large enough to enable nucleation, for instance as a consequence of local fluctuations. While the bubble is attached to the surface, it is subjected to mass transfer (as described in Section 4.2.2), thus growing until it is ready to detach.

Detachment

Bubble detachment occurs when the forces pulling the bubble upwards overcome the surface force keeping the bubble anchored to the site. Several forces play a role in this process, but research is still ongoing to describe their different effects on the detachment. In this chapter, the simple approach by Fritz [121] is used: a force balance between buoyancy and surface force allows to obtain a critical radius for detachment, usually called the Fritz radius (R_f in Equation 4.25).

$$R_f = \left(\frac{3}{2}\frac{\sigma R_{\text{site}}}{(\rho_l - \rho_g)g}\right)^{\frac{1}{3}} \tag{4.25}$$

Upon reaching this radius, the bubble will detach and it will start rising in the column. The process of detachment is treated in the DBM as a breakup: a volume of gas equal to the cavity volume is left attached to the surface ready to nucleate a new bubble while the remaining gas is the newly formed bubble that is free to rise in the column.

It is important to note that the Fritz radius represents a good approximation of the detachment size when no other forces are present, or in other words if the bubble and the liquid around are completely stagnant. If shear flow, for instance, or other types of flow are present, then the detachment would occur at a different size (perhaps earlier, as shown for instance by Mirsandi et al. [122]). On the other hand, the system under consideration does not have such strong cross-flows and using the Fritz radius is a considered as a safe approximation.

Limitations and assumptions

Finally, a few remarks on the limitations of the current implementation of heterogeneous bubble nucleation. The state-of-the-art detachment criterion, based on the Fritz radius, does not account for the many other relevant phenomena that might play a role. For instance, shear flow or even collisions of nucleating bubbles with neighboring bubbles are not considered in the calculations, as well as possible coalescence with neighboring nucleating bubbles (while they remain considered for freely rising bubbles as described in section 4.2.2). The initialization of the nucleation sites is currently done in such a way that this will never happen, while for a real case scenario this should be included in the model. Moreover, the initial volume of the gas pocket is initialized as a spherical bubble, of which the radius is used as a detachment criterion. Compared to a conical cavity, the assumption of a spherical bubble might not result in the correct radius calculation for the detachment. In addition, our simulations now rely on fictional parameters for the nucleation sites properties (i.e. a random Gaussian distribution of site radii). However, these parameters will depend upon the surface material, the liquid and gas properties *etc*. These parameters need to be adjusted to obtain physical results for a real surface, as will be further discussed in the following chapter.

4.2.6 Summary of the implementation

At the DBM initialization, a surface is initialized with assigned nucleation sites, with random position, radius (R_{site}) taken from a Gaussian distribution and depth (d) assigned as explained in Section 4.2.5. Equation 4.22 is used to check if a gas pocket is formed, of which the gas volume is calculated through Equation 4.23 while its radius of curvature (R_p) is computed from Equation 4.24. If the local critical radius, defined in Equation 4.21, is larger than the radius of curvature, an artificial bubble with equal volume as the cavity is generated, functioning as the bubble embryo and kept attached to the wall. Such bubble will grow, until reaching a size which allows the detachment. This size is called the Fritz radius, as defined in Equation 4.25. At the moment of detachment, the embryo bubble remains attached to the surface with a volume equal to the cavity volume, while the remaining gas is treated as a breakup, with a new detached bubble which can rise in the column.

4.3 Results

4.3.1 Numerical setup

The considered domain is a cube box with a length of 15 cm described by a Eulerian grid of 30 × 30 × 30 grid nodes. The liquid is water at standard conditions ($\rho_l = 1000\,\mathrm{kg\,m^{-3}}$, $\sigma = 0.073\,\mathrm{N\,m^{-1}}$ and $\mu_l = 10^{-3}\,\mathrm{Pa\,s}$). The dissolved gas is CO_2, which is initially perfectly mixed in the liquid bulk with different mass fractions, corresponding to different initial supersaturation ratios. The typical time step is 1 ms for both the species and the flow solvers while bubble movements are computed using time steps 20 times smaller. A total of 1300 nucleation sites is randomly generated with a size taken from a Gaussian distribution with a mean of 0.5 mm and a standard deviation of 0.3 mm, chosen to obtain a relatively dense surface coverage. Out of these nucleation sites, a total of 592 gas pockets (active sites) are formed, following the procedure detailed in Section 4.2.5.

4.3.2 Analysis of the nucleation process

A snapshot of the bubble nucleation, growth and detachment is shown in Figure 4.6. At the beginning, the gas pockets are represented as a bubble with equal volume attached to the surface. As a consequence of mass transfer, the pockets (bubbles) start growing, until a bubble reaches a diameter equal to the Fritz radius and detaches (leaving behind the gas pocket volume), as visible in Figure 4.6b. After some time, most of the sites reach a pseudo-steady state in which the system is continuously forming bubbles. This pseudo-steady state, where the supersaturation in the liquid is reducing as the concentration of dissolved gas starts depleting as a consequence of the bubble formation, is also visible in terms of average bubble sizes in the column (see Figure 4.7). The first peak (slowly shifting to the right) represents the gas pockets volumes, growing because of mass transfer. When the detachment of bubbles starts, the distribution tends to become wider and flatter, because of the presence of large bubbles rising in the column and small nuclei growing on the surface.

The initial growth of bubbles attached to the surface also affects the concentration profiles in the column, where the supersaturated liquid starts desaturating closer to the surface (see Figure 4.8a) as a consequence of the mass transfer of dissolved gas in the liquid towards the growing bubbles. Indeed, a depletion zone can be observed, which is slowly extending

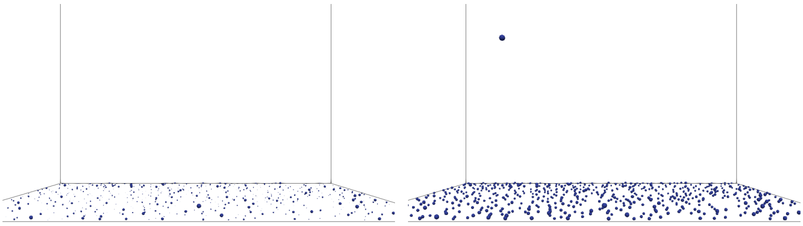

(a) $t \approx 0\,\mathrm{s}$ (b) $t \approx 4.8\,\mathrm{s}$

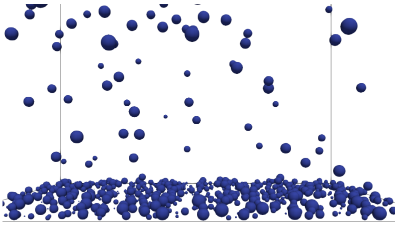

(c) $t = 120\,\mathrm{s}$

Figure 4.6: Snapshots of the bubble nucleation process on a surface for supersaturated water with CO_2 with $\zeta \approx 5.7$ as initial supersaturation. (a) Initial gas pockets volumes. (b) First detachment event. (c) Pseudo-steady state.

upwards. As soon as bubbles start detaching, this zone gets perturbed, as visible in Figure 4.8b. Channel-like structures of lower concentration areas represent the wake of bubbles rising, which meanwhile still grow because of mass transfer. This is a transition regime, which ends when swarms of bubbles detach steadily from the surface inducing more mixing in the system, as visible in Figure 4.8c.

4.3.3 Effect of the supersaturation ratio

The initial supersaturation ratio has a large influence, not only because it changes the amount of gas that can be transferred to the gas phase (and thus directly the mass transfer rate), but also because it affects properties such as the critical radius (defined in Equation 4.21) that controls the nucleation process. When the supersaturation is increased, bubbles grow much faster on the surface, detaching earlier. The critical radius is also smaller, which implies that more nucleation sites are active. This is clearly visible in Figure 4.9, showing the bubble size distributions in the column for different supersaturation ratios. At the lowest initial supersaturation, the nucleation process is still in its early stages, corresponding to the situation where bubbles are still growing on the surface, while for larger ratios (Figure 4.9c and Figure 4.9d) the surface is already bubbling and a wider bubble size distribution has been established. For the highest supersaturation ratio the bubble size distribution has shifted

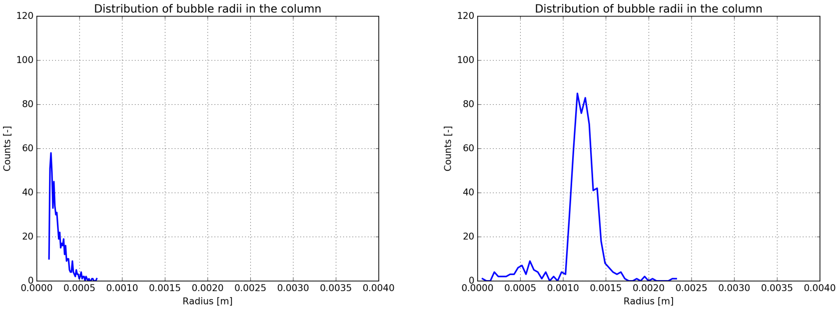

(a) $t = 2$ s (b) $t = 20$ s

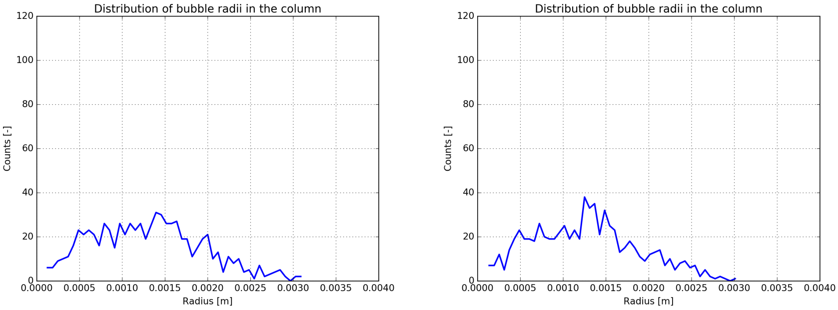

(c) $t = 40$ s (d) $t = 80$ s

Figure 4.7: Bubble size distribution in the column for a supersaturation ratio $\zeta \approx 5.7$

slightly to larger diameters, which can be attributed to two effects: i) bubbles grow much faster on the surface, increasing the number of large bubbles in the column compared to the number of small bubbles on the surface; ii) the bubbles can grow larger because of increased mass transfer and bubble coalescence (a higher bubble number density increases the bubble encounter frequency). It is worth mentioning that a time span of 20 s seems rather unrealistic for an initial supersaturation of about 2.3 to not have detached any bubble yet, but this is related to the nucleation sites density and the relatively small selected radii of the original gas pockets, requiring the bubbles to grow for a relatively long time span before the first bubble is detached. This work is the first step in the integration of a nucleation model in the DBM. Selection of the model parameters can be improved when more experimental data become available. As bubbles detach faster, more of them will be present in the column at the same time, as can be discerned from Figure 4.10, showing the total number of bubbles in the column as a function of time. Indeed, the total number of bubbles in the column is much smaller for the smallest supersaturation, while at the same time it takes much more time to develop a steady rate of bubble formation. On the other hand, the depletion of concentration starts to become pronounced for the highest supersaturation, where bubbles are quickly formed, but where the number of bubbles is already decreasing, corresponding to the decrease in liquid

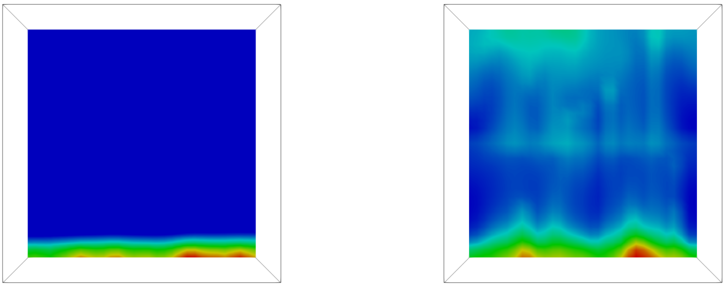

(a) $t = 4\,\mathrm{s}$

(b) $t = 26.2\,\mathrm{s}$

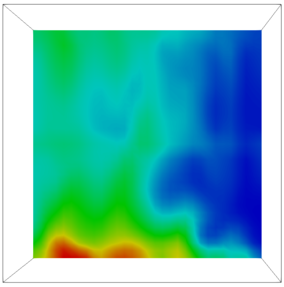

(c) $t = 120\,\mathrm{s}$

Figure 4.8: Concentration profiles of CO_2 in the liquid phase in a plane in the middle of the column for an initial supersaturation $\zeta \approx 5.7$. Concentration ranges from red (lower) to blue (higher).

concentration.

4.3.4 Effect of the surface properties

In this work, the surface nucleation properties have been randomly generated. Real surfaces may have different properties, which can be determined from dedicated measurements. In order to put into context how the system will respond to a certain variation in the nucleation properties, a sensitivity analysis of nucleation site parameters has been performed. The numerical setup as described in section 4.3.1, with a starting supersaturation of $\zeta \approx 5.7$ (initial mass fraction of CO_2 $Y_{0,CO_2} = 0.015$) has been taken as the base case, while in three other cases the total number of sites (Case 1), the mean nucleation site radius R_{site} (Case 2) and the standard deviation of the nucleation site radii distribution (Case 3) has been varied. A list of varied parameters for each case is summarized in Table 4.1.

From Figure 4.11a it can be observed that the number of bubbles in the column is drastically reduced for Case 1, as a consequence of the lower number of nucleation sites. Indeed, out of the predefined 200 sites, a total number of 131 gas pockets is available for nucleation. This slows down the nucleation process considerably, which affects the occurrence of all bubble

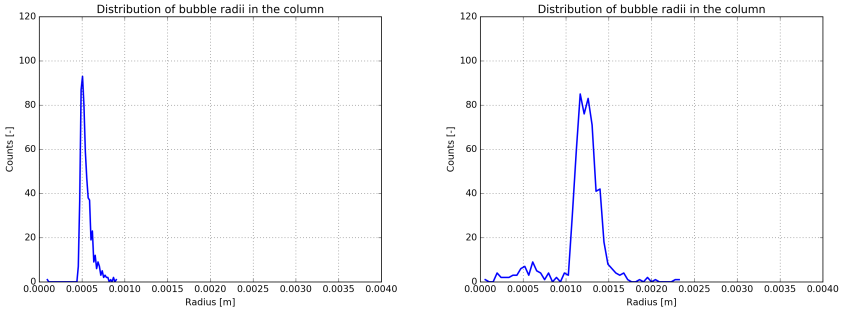

(a) $\zeta \approx 2.3$ (b) $\zeta \approx 5.7$

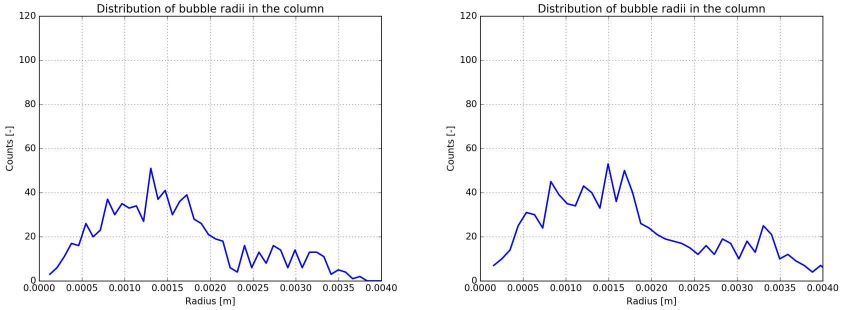

(c) $\zeta \approx 9.0$ (d) $\zeta \approx 12.4$

Figure 4.9: Bubble size distribution in the column for different initial supersaturation ratios at $t = 20\,\mathrm{s}$.

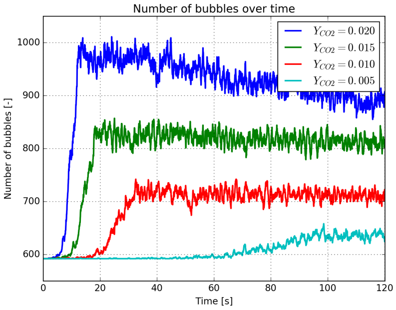

Figure 4.10: Number of bubbles in the column over time, at different initial CO_2 concentrations.

Table 4.1: Description of sensitivity analysis cases

Case	Description	Parameters
Base Case	$\zeta \approx 5.7$, case described in section 4.3.1	$N_{site} = 1300$ $R_{mean} = 0.5$ mm s = 0.3 mm
Case 1	Decreased number of nucleation sites	$N_{site} = 200$
Case 2	Decreased mean radius of radii distribution	$R_{mean} = 0.25$ mm
Case 3	Decreased standard deviation of radii distribution	s = 0.2 mm

sizes, as seen in the bubble size distribution shown in Figure 4.11b. Since more bubbles are still growing attached to the surface, the bubble size distribution becomes more similar to the one of lower supersaturation, with a clear bimodal peak due to the presence of a considerable amount of bubbles still growing at the surface. On the other hand, the effect of the change in the standard deviation of the nucleation sites (Case 3) is not as influential, and results in a similar bubble size distribution as the base case. Unless the site radius distribution is generated with a very wide distribution, the site radius distribution is of less importance for the nucleation process.

Changing the mean radius however (Case 2) shows a considerable effect in the number of bubbles produced. The reason for this particular increase lies in the number density of nucleation sites. Indeed, when they are generated with a smaller average radius, more sites can be fitted on the surface, leading to a larger number of nucleating bubbles. The difference in size does not induce a difference in trends, which can be seen to match well with the Base Case and Case 3. However, it is visible that in Case 2 the detachment phase starts slightly earlier compared to the base case. This is related to the Fritz radius, which is proportional to the cube root of the nucleation site radius, allowing bubbles to detach earlier when the site has a smaller size. Although the number of bubbles changes, the bubble size distribution does not; this is because the size is dominated by bubbles rising in the column which are mostly

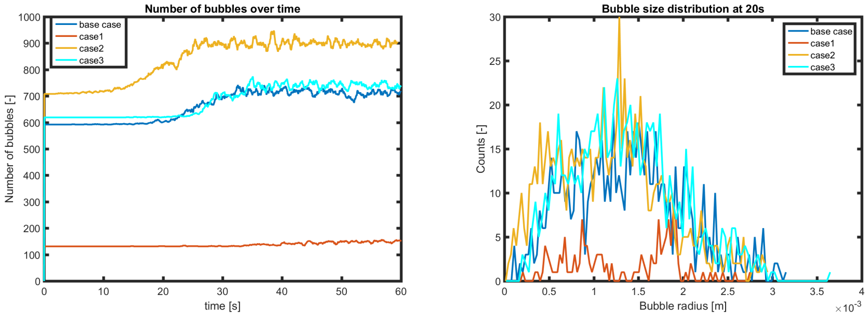

(a) (b)

Figure 4.11: (a) Number of bubbles in the column over time, varying surface parameters. (b) Bubble size distribution in the column at $t = 40$ s.

determined in size by the degree of supersaturation, while for Case 1 the majority of bubbles are still attached to the nucleation sites.

As visible from this short sensitivity analysis, surface properties are able to influence the number of nucleated bubbles and in some cases the instantaneous bubble size distribution. For this reason, it is important to stress again the importance of dedicated measurements to be able to mimic real surfaces.

4.4 Conclusions and outlook

This work has discussed the integration of heterogeneous bubble nucleation into a Discrete Bubble Model. An algorithm has been proposed and implemented to study the formation of bubbles on a solid surface as a result of supersaturation, assuming random conical nucleation sites. This chapter serves as a demonstration of the capabilities of the DBM as a meso-scale model: it is possible to gain relevant understanding on relatively large swarms of bubbles with a sufficient level of detail, successfully performing as the gateway between Direct Numerical Simulations (DNS, very detailed but limited to a handful of bubbles) and large-scale Euler-Euler (fast and large scale, but no details on individual bubbles).

A clear initial regime is visible where bubbles are slowly growing while remaining attached to the surface, with the formation of a depletion layer close to the bottom surface. As soon as bubbles start reaching the Fritz radius, and thus detach, they introduce a more vigorous mixing which breaks the depletion layer. An increase in the initial supersaturation not only decreases the time span of this first growing regime, but also increases the total number of bubbles in the system and their sizes. For higher supersaturation ratios, the total number of bubbles is clearly decreasing in time, as a consequence of the fast depletion of the dissolved gas in the system.

A sensitivity analysis of surface properties has been performed. The nucleation sites number density has a clear effect both in the number of bubbles and in the bubble size distribution. Fewer sites will form less bubbles and will not mix the system leading to an overall slower phase transition process. On the other hand, decreasing the average site radius will lead to a higher number of bubbles as a consequence of the changed site density, while also slightly accelerating the detachment process because of the smaller average Fritz radius.

Despite its interesting capabilities, this model is not yet complete. Firstly, other effects for detachment, as for instance shear flows, have to be included. Moreover, interactions between bubbles that are still attached to the surface could lead to a potential early detachment after a collision or a coalescence event between two bubbles attached to neighboring nucleation sites, increasing the bubble formation rate. The effect of depletion should be studied further, as well as the fact that a bubble attached to the surface will experience lower mass transfer rates as a consequence of the lower available interfacial area. The latter two phenomena have been studied experimentally for single bubbles by Moreno Soto et al. [123] and Enríquez et al. [124] respectively, and could represent a relevant topic for future research at the meso-scale. In addition, experimental validation determining nucleation model parameters of actual surfaces is of extreme importance and has been started following the work of Enríquez et al. [117].

To conclude, the similarities with boiling flows have been already highlighted in literature [37]. The model here presented could be expanded to a boiling case, where similar simulations can be performed for instance at different Pr numbers.

CHAPTER 5

EXPERIMENTAL STUDY OF CO_2 BUBBLE FORMATION ON A SURFACE IN SUPERSATURATED WATER *

In this chapter, an experimental study is described to better understand the processes involved in the nucleation of multiple bubbles at different substrates, where the generated experimental data can be used to calibrate the parameters of the heterogeneous bubble nucleation model described in Chapter 4. A dedicated experimental setup consisting of two interconnected tanks has been constructed. In the larger tank, CO_2 is dissolved under pressure in water, while the pressure is released in a controlled environment in the second tank, where images of nucleating bubbles can be taken with a camera. A Digital Image Analysis technique has been developed and validated in order to analyze the growing bubbles.The experiments showed a consistent outcome compared to the modeling results of Chapter 4: an initial wave of equally sized small bubbles grows over time into a flatter and wider bubble size distribution, as a consequence of detachment, coalescence and nucleation events. In addition, a higher supersaturation ratio is found to be responsible for the formation of more bubbles, but with smaller sizes due to the reduced critical radius. The effect of a larger pore size surface is negligible, as bubbles nucleate on smaller cavities than the steel pores. The bubbles show a consistent growth rate with the analytical solution of Epstein and Plesset (1950) but with a much slower mass transfer, because of the combined effect of the presence of the surface and local depletion. The nucleation model of Chapter 4 has been applied and it has been shown that it is able to predict qualitatively the experimental bubble size distribution, with a limited effect of surface properties apart from the site radius. In order to see the widening of the distribution, a distribution in the Sh number is required, to mimic depletion/competition effects, which needs to be studied in more detail in further works.

---

*This chapter is based on: Battistella et al. [125]

5.1 Introduction

The formation of gas bubbles occurs often in natural and industrial processes as a consequence of supersaturation or superheating. While the opening of a soda bottle or the boiling of water represent perhaps the easiest examples from everyday life, several industrial processes are also affected by the formation and growth of gas bubbles, as for instance in electrolysis [34, 35], molten polymers [98] and even bubbles in oil reservoirs [99].

As shown in Chapter 4, CFD based models represent an indispensable tool for the design and optimization of such processes. On the other hand, they require input parameters, such as the size and density of nucleation sites, which require an analysis and understanding of nucleation on a real surface.

Literature studies regarding the understanding of the physics of nucleation can be split into two different fields: supersaturation, where excess gas is dissolved in a liquid compared to its equilibrium, and superheating, where excess heat is stored in a liquid compared to its equilibrium. In both cases, bubbles (of gas or vapor respectively) are formed in the liquid in order to lower the local concentration/temperature and restore equilibrium.

Most research has been put into understanding the growth rate of bubbles from a microscopic point of view, tracking between a single and a handful of bubbles simultaneously on very well defined surfaces ([127, 128]). The achieved results are, for the most part, in agreement with the expected analytical solutions when bubbles grow solitary. However, it has been noted in Chapter 4 and from the work by Moreno Soto et al. [123] that bubbles which are growing in pairs or groups will compete for the available gas and grow slower. Consequently, this also affects their sizes when detaching from the surface or when coalescing each other, as there is not as much space to grow compared to the single case.

While still about a single microbubble, Frank et al. [129] investigated the detachment and growth of a bubble in different fluids (Newtonian and non-Newtonian) with Particle Image Velocimetry, showing promising results to connect with their Lattice Boltzmann approach. In the works of Enríquez et al. [117], Dietrich et al. [130], van der Linde et al. [131] and Moreno Soto et al. [123], an experimental setup with very well defined nucleation sites on surfaces has been used to study the growth of a single or a few microbubbles. Their fundamental work shows in rich detail the nucleation and growth process under diffusive conditions.

On the other hand, there is a gap in the literature regarding the nucleation of gas bubbles in relatively large numbers on a porous substrate. Most of the literature is more focused on gaining a total number of bubbles per unit time (nucleation rate) rather than dedicating attention to the surface parameters found in Chapter 4 (*i.e.* the size and density of nucleation sites), such as in the work of Lubetkin and Blackwell [132] where they used the sound of bubbles bursting on the top surface to quantify the nucleation rates.

The aim of this chapter is thus to bridge this gap and experimentally investigate the nucleation of (larger) groups of bubbles in order to provide the link between the CFD model described in Chapter 4 and real surfaces, understanding the influence of surface properties on the process of bubble formation. This will be done by recording images of nucleating CO_2 bubbles from supersaturated water and processing these images with Digital Image Analysis (DIA), to create an account of the evolution of the site distribution of nucleating, growing and detaching bubbles. In the following sections, the principles of nucleation will be recapped, the constructed experimental nucleation setup will be described, the developed DIA technique described and verified, and the experimental results of the formation of bubbles on real porous steel surfaces investigated.

5.2 Theoretical overview

A more comprehensive description of supersaturation and the formation of bubbles in a supersaturated liquid has been already given in Chapter 4. Nonetheless, a few relevant parts are hereby repeated for the sake of completeness.

5.2.1 Supersaturation

A liquid is (locally) supersaturated when the concentration is higher than the equilibrium concentration, which can be expressed, for instance, by Henry's law. A relevant parameter, called the *supersaturation ratio*, is introduced as [117]:

$$\zeta = \frac{c}{c_s} - 1 \tag{5.1}$$

which is an indication of the quantity of excess gas that is dissolved in the liquid compared to its equilibrium concentration (c_s, the saturation concentration). Thus, for phase transition to occur, the ratio has to be higher than the equilibrium, thus $\zeta > 0$. Equilibrium between the two phases exists when this ratio is equal to 0.

5.2.2 Mechanism of bubble formation

The mechanism of a gas bubble formation has been a topic of investigation for many years [118]. It is nowadays accepted in the literature that the predominant mechanism for bubble formation is heterogeneous nucleation, where bubbles form on pre-existing gas cavities present on a solid surface (see type III/IV in Chapter 4). The size of the cavity, the so-called nucleation site, is important to establish whether a growing bubble can be hosted. A critical radius (related to the Laplace pressure) is recognized by Jones et al. [118] as shown in Equation 5.2, which represents the minimum size for a bubble to be able to grow by mass transfer, without dissolving back into the liquid.

$$R_c = \frac{2\sigma}{p_s \zeta} \tag{5.2}$$

In this equation, σ and p_s represent the surface tension coefficient and the saturation pressure of the gas respectively.

The bubble on the site grows until the buoyant forces pulling on the bubble are able to overcome the surface tension anchoring the bubble to the surface. At this point, the bubble detaches and starts rising in the liquid. Fritz [121] derived an expression (see Equation 5.3) for the detachment radius, usually called the Fritz radius, by writing a force balance between said buoyancy and surface tension:

$$R_f = \left(\frac{3}{2} \frac{\sigma R_{\text{site}}}{(\rho_l - \rho_g) g} \right)^{\frac{1}{3}} \tag{5.3}$$

As explained in Chapter 4, the Fritz radius is a good approximation of the detachment radius when the liquid is quiescent, but does not account for several other factors such as shear flow. On the other hand, the experimental system in consideration does not present strong flows and thus it is considered as a reasonable assumption.

5.3 Experimental Setup

The constructed experimental setup is based on the setup used by Enríquez et al. [117]. A saturated solution of a gas and liquid (*e.g.* water-carbon dioxide) is prepared and then supersaturation is induced by a controlled release of the pressure. Below a description of the setup and its major characteristics is provided.

5.3.1 Vessels configuration

The system consists of two interconnected 316L stainless steel vessels manufactured by METAL machinebouwers b.v. (Nijverdal, the Netherlands). The largest of the two (shown in Figure 5.1a) holds approximately 7 liters of liquid and has the sole purpose of preparing a water solution saturated with carbon dioxide. Hence, it is hereby referred to as the *mixing vessel*. The top plate covering the tank has openings for both the gas and the liquid and a magnetic couple (Macline mrk16, Premex Reactor AG), required in order to rotate the gas injection propeller (BR-3, Premex Reactor AG) within the tank. The magnetic stirrer is required in order to mix the gas and the liquid and decrease the preparation time of the saturated solution, following the work of Enríquez et al. [117]. Figure 5.2 illustrates the propeller's work: the shaft is hollow, allowing gas to pass through and exits at the blades, forming bubbles and increasing the gas-liquid mixing, which allows preparing a saturated solution in about 1 hour.

The saturated solution is then flowing in the smaller tank (*measurement vessel*, Figure 5.1b), which holds approximately 1.5 liters of liquid and is placed below the level of the mixing vessel. The measurement vessel has three sight glasses installed giving visual

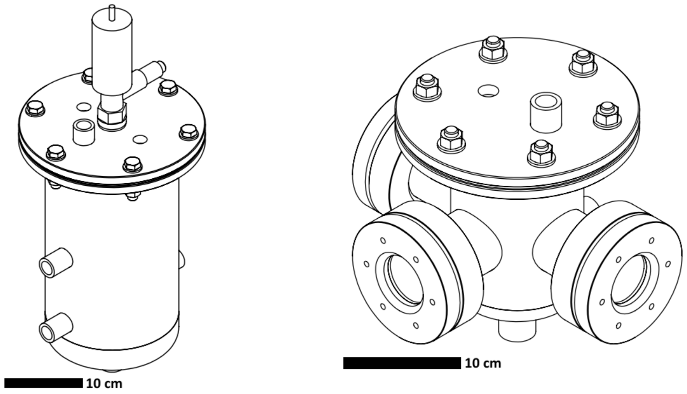

(a) Mixing vessel

(b) Measuring vessel

Figure 5.1: Depiction of the two vessels.

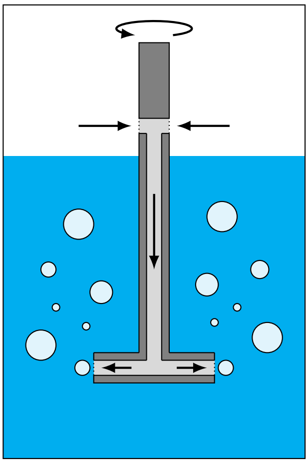

Figure 5.2: Depiction of the gas injection propeller. Adapted from Enríquez et al. [117].

access to the inside. The configuration allows for a flexible placement of the illumination and visualization of the experiments, as will be explained further below.

Both vessels are equipped with a level sensor (FTL31; Endress+Hauser) to ensure the amount of liquid in between two experiments is equal within the error of the valve/sensor. As temperature can greatly affect the solubility of gasses in liquids a temperature sensor (TMP31; Endress+Hauser) is placed in both tanks. Two equal pressure sensors (PMP11; Endress+Hauser) are present to monitor the tank pressure, which is extremely important as described in the next section.

5.3.2 Pressure control

The setup makes use of Henry's law, which states that the amount of dissolved gas in a liquid solution is proportional to its partial pressure above the liquid. The so-called Henry's constant, which is the proportionality coefficient, represents the solubility of the given gas in the given liquid. Thus, when the mixing tank is filled with gas under pressure and left for a sufficiently long time, the system can be considered at equilibrium and the gas-liquid solution is saturated. The alteration of the (partial) pressure (for instance by a sudden release of part of the gas) brings the system into a supersaturated state, thus initiating the bubble nucleation process, as it is for instance when opening a bottle of sparkling water.

The two vessels are designed for a maximum operating pressure of 8 barg, which allows for a wide range of supersaturation by controlling the pressure release. To ensure a smooth transition while releasing pressure, a small buffer tank is placed on top of the measurement vessel. In addition, a needle valve is used to release the pressure more slowly and achieve a better control.

5.3.3 Substrate and substrate holder

Inside the measurement vessel, a substrate is placed where bubbles are forming and analyzed through Digital Image Analysis (see Section 5.4).

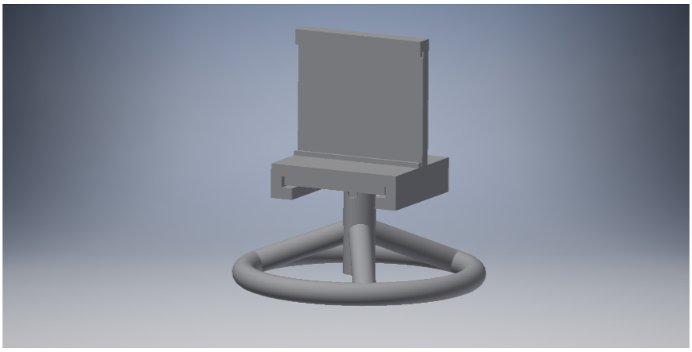

Figure 5.3: Depiction of the 3D-printed sample holder in the vertical position.

Two porous steel plates with different pore sizes (40 µm and 100 µm) are used as different substrates in this work, in order to capture the effect of the surface pore sizes on the nucleation rates. In order to correlate the camera resolution with the actual dimensions, a $2 \times 2\,\mathrm{cm}$ square is drawn on the substrate with a black marker. This coating has the additional effect of reducing reflections, which is advantageous for the Digital Image Analysis processing, but it will probably also (slightly) change the surface properties. The detailed effect of the surface properties is considered out-of-scope of this work, as the most likely affected surface properties of unmarked steel (*e.g.* gas-liquid-solid contact angle or surface energies) are not measured either.

The substrate is kept in position vertically by a 3D-printed holder made of ABS plastic, illustrated in Figure 5.3. This solution allows for a cheap and easily adaptable design of the holder, giving the possibility to achieve various configurations. In this chapter, only the vertical positioning is discussed.

5.3.4 Experimental procedure

The selected gas-liquid combination is CO_2-water, as it represents a convenient choice due to the high solubility of CO_2 in water ($\sim\ 1.6\,\mathrm{g}_{\mathrm{CO}_2}\,\mathrm{kg}^{-1}_{\mathrm{H}_2\mathrm{O}}$), allowing for a shorter mixing period compared to other gases in order to reach saturation and shorter degassing times [117].

Saturated solution preparation

The first step is the preparation of the saturated solution in the mixing vessel. Initially, the system is completely flushed from the bottom with CO_2, in order to purge any other gas. At the end of the purging, all exit valves are closed and the pressure is increased to 1 barg, in order to maintain a CO_2 atmosphere.

With both tanks purged and pressurized, the connection between them is closed in order to separate the two sections. Then, the water inlet is opened and the tank is filled until the level switch activates. It is important to note that, during this operation the pressure increases (liquid volume is entering the vessel). In order to avoid backflow of gas into the liquid lines (which are at about 4 barg), the exit valve from the mixing vessel is opening regularly in order to keep the pressure at 1 barg.

Once the tank is full, the CO_2 line is opened for about 2 minutes (still with the pressure regulation described above), in order to strip the liquid of any other dissolved gas (*i.e.* nitrogen and oxygen). Then, at the end of this procedure, the vessels are both pressurized with CO_2 at about 6.5 barg. Finally, the motor is started, the propeller is set in motion and the solution is left to be saturated for approximately 1 hour.

Measuring procedure

When the solution is ready, the connection between the two tanks is opened and the liquid is transferred to the measuring tank. Once full, the two sections are separated again and the solution is left to settle for a couple of minutes while the camera and illumination are set. Then, the pressure is reduced by the desired amount using the needle valve, which is subsequently closed again while bubbles start to form on the substrate.

The optimal configuration to take images was experimentally found to be when two LED lights are illuminating the side sight glasses, with a diffuser plate to achieve an even illumination. An Imager pro HS 4M camera (LaVision GmbH), with a resolution of 2016 × 2016 pixels and a Nikkor 200 mm macro lens is placed in front of the front sight glass and is used in order to take images of the growing bubbles on the substrate, for about 30 minutes at intervals of 2/5 minutes. As will be later described, the first image is taken before the pressure release in order to have a reference background image for background removal.

After the experiment is performed, the liquid is drained from the measurement vessel after releasing fully the pressure. It is important to note that the mixing vessel is larger, in order to be able to perform multiple experiments with the same solution and shorten waiting times. For this reason, after the measurement vessel is completely empty, it is flushed with CO_2, brought back at the same pressure of the mixing vessel and refilled accordingly for another experiment.

5.4 Digital Image Analysis

The bubble properties, namely bubble sizes, positions, numbers *etc.*, can be acquired through Digital Image Analysis (DIA) following a number of image manipulation steps. A description and verification of the developed method is provided in the next sections.

5.4.1 Algorithm

The DIA algorithm is written in *Python* [133] (version 3.8.5) making use of the Open Source libraries *NumPy* [134] (version 1.20.0), *OpenCV* [135] (version 4.5.1.48) and *scikit-image* [136] (version 0.18.1).

The bubble detection, shown in Figure 5.4, is divided in three different parts: large bubbles (35-50 pixels), medium bubbles (20-35 pixels) and small bubbles (4-20 pixels). The reason for this is that the technique for bubble recognition/labelling works best for a specific range of sizes, which is too narrow to cover all the sizes observed in the experiments. The first steps of the detection are the preparation of the image: first the background is subtracted (using a background image taken beforehand), the rotation is adjusted (if required) and the figure is cropped to the borders of the marked area, as visible in step 1 of Figure 5.4.

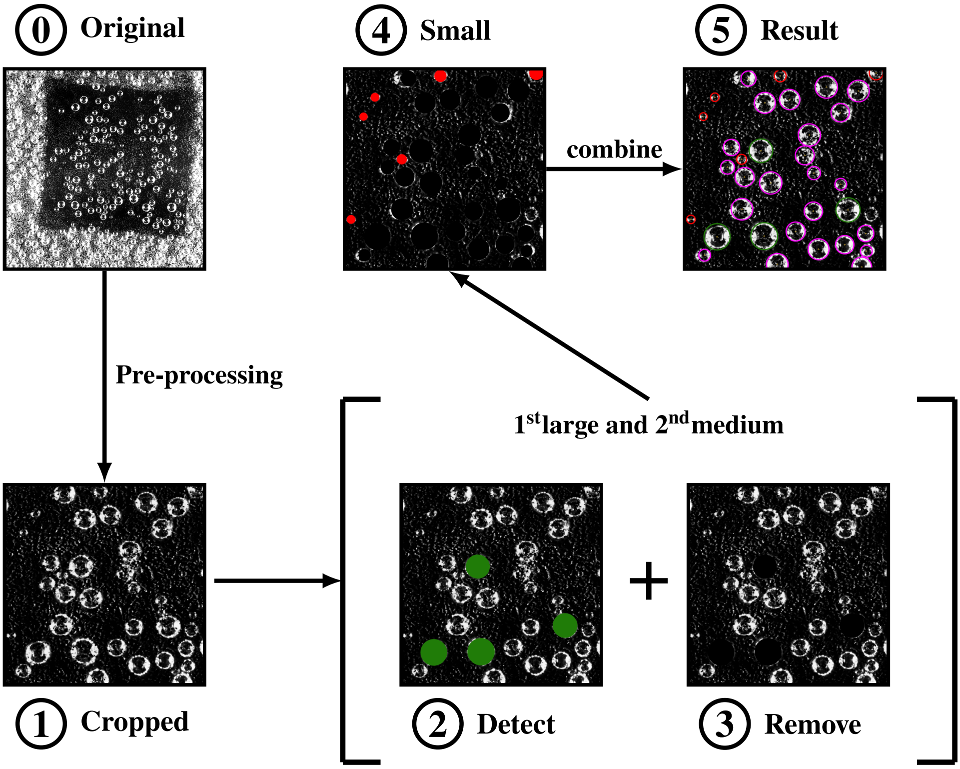

Figure 5.4: Image processing sequence to detect bubbles. The cropped area is smaller than an actual image for illustration purposes.

Then, the actual bubble detection routines start. First, the large bubbles are detected with their own parameters and then removed from the image, to avoid duplicates and interference (step 2 and 3 in Figure 5.4). Then, the same procedure is applied to the medium size bubbles, with different parameters, which are subsequently also removed from the image. Finally, the small bubbles are detected with their own procedure (step 4) and the three data sets of detected bubbles are combined to obtain the final result (step 5).

In Figure 5.5, the detection sequence for the small bubbles, after the removal of large and medium bubbles, is shown. As mentioned, the large and medium bubbles follow a different detection procedure from the small bubbles. Since the bubbles are extremely small in resolution (4 to 20 pixels radius), noise removal is challenging, as the noise from the porous steel reflections is of the same size as the bubbles. While background removal helps, noise is not entirely removed because the subtracted background and the image have slight deviations (usually to the pixel level) due to the camera vibrating while taking pictures as a consequence of the internal heat removal fan. The remaining noise influences the detection of the bubbles (especially with the smallest) because it has the same intensity of the bubble edges. On the other hand, the illumination from both sides of the setup results in brighter sides of the bubble

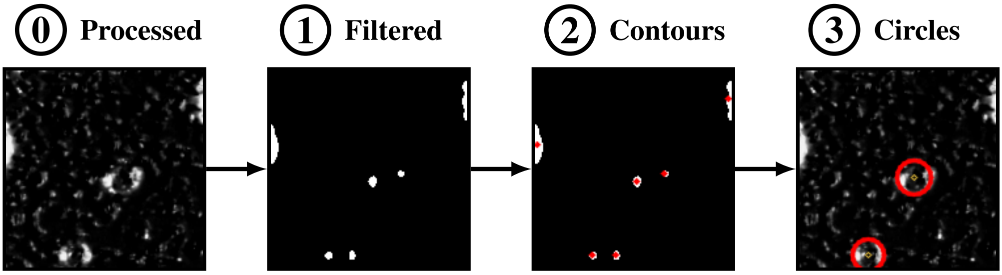

Figure 5.5: Image processing sequence to detect small bubbles after large and medium size bubbles have been removed. Magnification of the same experimental image shown in Figure 5.4.

edges. Thus, the image is heavily thresholded in order to intensively remove the noise while leaving only two parallel contours (the sides of the bubble edges). With the DIA, the two contours from the filtered image are identified. Then, their centroids are detected, and if they are close enough and on a horizontal line (within a few pixels margin) they are selected as a circle. The diameter of the circle is then calculated as the distance between the leftmost and rightmost points of the two contours and the circle center as the middle point of said line. In order to avoid overlaps with neighboring circles with contours close enough to be mistaken for a circle, the contours are all sorted from left to right and processed in such order.

While this procedure can be applied safely for small bubbles, for larger bubbles it results in several false circles detection without additional pre-processing steps. In Figure 5.6, the detection sequence for large and medium bubbles is illustrated. First, the noise from the porous steel reflections has again to be removed or reduced. Thus, a few steps are taken to reduce noise: i) a median blur filter is applied to smoothen the image, ii) the image is thresholded and iii) small objects (sometimes including small bubbles) are removed as noise. The final outcome is shown in Figure 5.6 at step 1.

After this, the edges of the bubbles are highlighted with the edge detection algorithm proposed by Canny [137] and implemented in the *OpenCV* library of Python, as shown in Figure 5.6 at step 2. This algorithm makes use of an additional series of internal filtering steps and uses the intensity gradient of the image in order to identify edges. This step is necessary in order to aid the subsequent circle detection step. Indeed, since the experimental bubbles are round by nature, a circle detection algorithm has been used to detect them. This is the Hough Circle Transform algorithm of *OpenCV*, which has been used widely in the literature to detect circles (or ellipses) in images [138]. The Hough circle transform implemented in *OpenCV* is relatively robust to identify circles, but unfortunately not as much when it comes to determine their sizes, constantly making errors especially when the bubble size is very close to the transition region (e.g. between large and medium). For this reason, once the bubble is identified with the Hough transform, it is passed to the same algorithm used for the small bubbles in order to detect its size properly.

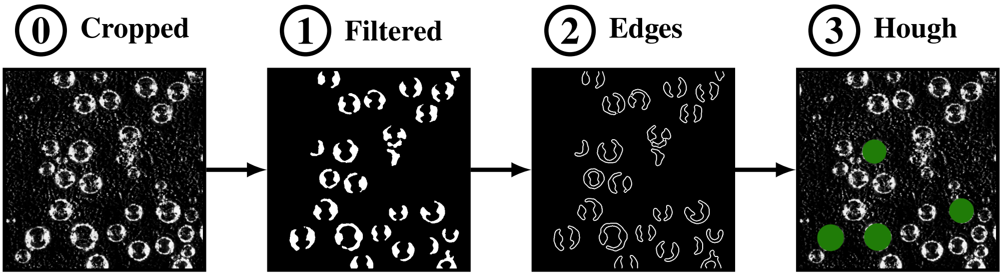

Figure 5.6: Image processing sequence to detect large and medium sized bubbles from the preprocessed image. The cropped area is smaller than an actual image for illustration purposes.

5.4.2 Verification

The performances of the DIA have been verified with artificially generated images and with experimentally obtained images.

Single bubble verification

A single bubble from an experimental image has been selected as representative of experimental bubbles for all the three sizes, namely one bubble of 10 pixels in radius, one of 34 pixels in radius and one of 45 pixels in radius. All three of them are then resized using the built-in function of *OpenCV* in the range of 10-50 pixels, in order to check for the correctness of the radius detection with a single bubble.

As visible from Figure 5.7, all three bubbles resized in all sizes are detected within a 1/2 pixel accuracy, which is a very good result accounting for the fact that bubbles are not perfectly spherical and even the human eye has a 1/2 pixel margin in the determination of the radius. In addition, sometimes the edge of the bubble is not sharply terminating between one pixel and another, resulting in a another source of inaccuracy.

From the images, it is also visible that the 10 pixel bubble is the one that, at increased bubble sizes, deviates the most. This is because the bubble is not very resolved (as it is small) and thus the resizing process introduces noise at the interface, which then adversely influences the accuracy of the DIA. Despite this, it can be seen that the bubble sizes are recognized well in the size range relevant for this work.

Generated bubble images

From experimental images, 470 bubbles have been manually labelled, measured in size and extracted as a single bubble image. Then, the extracted bubbles are binned and used to generate an artificial bubble image with an imposed bubble size distribution (e.g. a Gaussian distribution of radii). For the generation of the artificial image, a true empty experimental image of the background surface is used on which the extracted bubbles are randomly placed.

A number of 100 images with 100 bubbles each, totalling 10000 bubbles, are generated imposing a Gaussian distribution of radii with average 30 pixels and standard deviation 7.5 pixels. The DIA algorithm is then used to detect the bubbles, with a considerable accuracy,

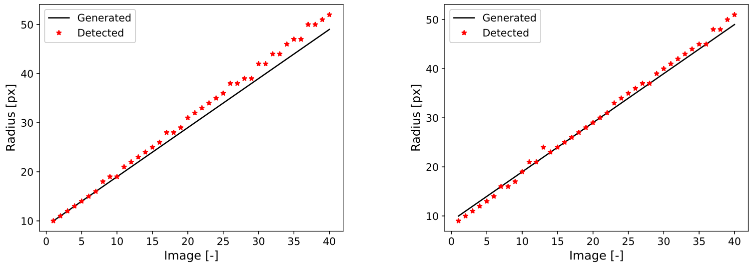

(a) $R_{bub} \approx 10\,\text{px}$ (b) $R_{bub} \approx 34\,\text{px}$

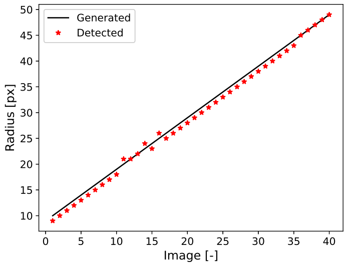

(c) $R_{bub} \approx 45\,\text{px}$

Figure 5.7: Detected vs generated radius for a single bubble resized across the 10-50 pixel size range, with three different experimentally obtained bubble images of radius R_{bub}.

of which an example is shown in Figure 5.8. A number of 9478 bubbles are detected with a mean radius of 29.08 pixels. The error is still considered within the margin of accuracy of the human eye, as the labelled images are measured visually and do introduce a source of inaccuracy. In addition, out of the 9478 detected bubbles, an average of 1 detection error (detected but not existing bubble) every 2 to 3 images reduces the overall hit rate to about 94%, which is considered a good result for the objective of this work.

To conclude, Figure 5.9 shows the generated bubble size distribution against the histogram of the detected bubbles' probability density function normalized to 1. It is visible that the shape and mean of the distribution is captured by the detection, but with considerable undershoots and overshoots in some of the bins. This is attributed to the somewhat limited number of bubbles used for the generation (470), which introduces a systematic error if their size is measured incorrectly by the human eye. Nonetheless, it is clear that the developed DIA is able to determine the bubble size distribution with a good margin of accuracy, thus it is possible to move further to the analysis of experimental bubble images.

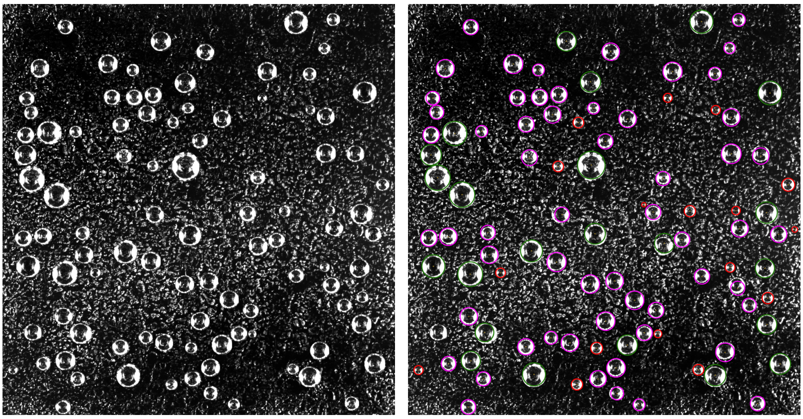

(a) Generated

(b) Detected

Figure 5.8: Generated vs detected for an artificially generated image with 100 bubbles with a Gaussian distribution. The colors represent the large sized bubbles (green), the medium sized bubbles (purple) and the small sized bubbles (red).

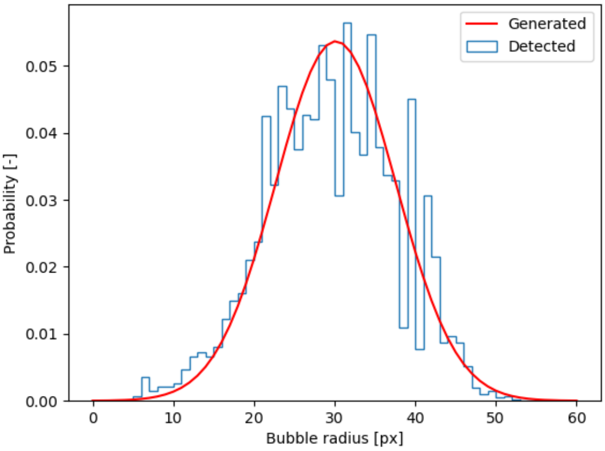

Figure 5.9: Comparison between the generated and detected bubble size distribution.

Experimental bubble images

When using an actual experimental image, bubbles do not have the same characteristics but present differences not only in their sizes but also in illumination and focus. This is the part that makes the DIA algorithm less robust, as it requires fine-tuning of the detection parameters (*e.g.* the Hough circle transform parameters and threshold levels) to obtain a better detection.

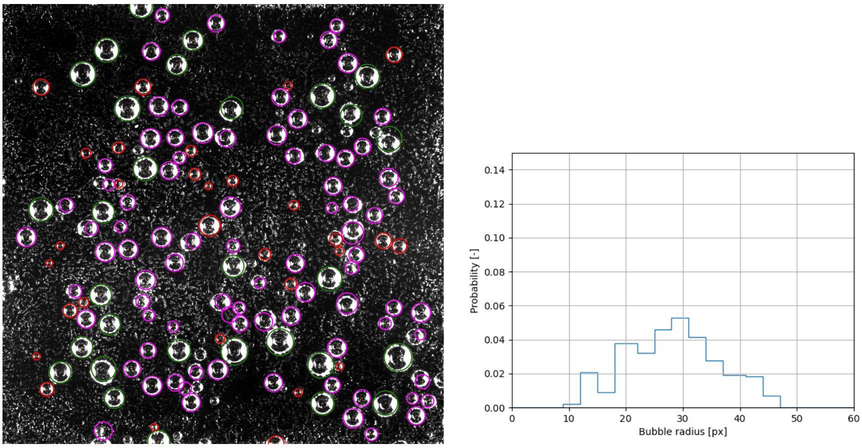

(a) (b)

Figure 5.10: (a) Detected bubbles from an experimental image and (b) detected bubble radii distribution.

Table 5.1: Experimental image detection verification.

	Detected	**Missed**	**Wrong**
Large	30	0	0
Medium	85	6	3
Small	30	22	0
Total	145	28	3

With a relatively good (slightly out of focus) experimental image, it is possible to obtain about 83.5% of correctly detected bubbles over the total (137/170 bubbles). Indeed, as visible in Figure 5.10, not all bubbles are correctly detected with a few bubbles that are missed and 3 wrongly detected ghost (*i.e.* not existing) bubbles. In Table 5.1 an overview of the total bubbles is presented.

The somewhat larger missing rate compared to the artificially generated images holds especially for the small bubbles (about 78% of the total miss), which are difficult to see even for the human eye. This should not be considered as an error, but rather as a limitation of the current setup which could be improved by using a higher resolution camera or a lens with higher magnification. On the other hand, missing a few small bubbles does not alter the findings of this chapter. The actual error (or inaccuracy) at the bubble size detection is much smaller, as only 5 (3%) of the bubbles are incorrectly detected in their size.

Final considerations

It is thus possible to fine-tune the DIA parameters in order to obtain 85% correct detection. On the other hand, in order to keep a consistent error between images of the same data set (experiment time evolution), where the conditions are more or less the same but the size of the bubbles changes drastically, it is better to slightly reduce the accuracy of a late time image (by missing a few bubbles more) but increasing drastically the accuracy of the early time image (where bubbles are smaller, hence more difficult to detect). This is difficult to determine *a priori*, but rather is depending on the conditions of the experimental dataset and is found by trial-and-error.

5.5 Results

The constructed experimental setup and the verified DIA technique have been used to perform experiments on two different porous steel substrates. The results of the time evolution, bubble growth and a comparison with the nucleation model developed in Chapter 4 are illustrated in the following sections.

5.5.1 Time evolution

Bubbles grow over time as a consequence of mass transfer induced by supersaturation. Figure 5.11 shows the development of the bubble size distribution over time for a supersaturation ratio of 0.16 on the surface with a pore size of 40 µm. Similar to what was observed in the modeling results of Battistella et al. [84], first (at a time of 2-5 minutes) there is a very narrow bubble size distribution where the bubbles attached to the surface grow more or less parallel to each other. As soon as the first bubbles start detaching or coalescing with each other and bubbles start growing again, the bubble size distribution widens and flattens.

Number of bubbles

The same effects are visible also on the total number of bubbles over time. As shown in Figure 5.12, the total number of bubbles is decreasing over time. This can be attributed to a few effects: i) when a bubble detaches, the subsequent one is too small to be immediately visible (camera resolution is limiting), ii) coalescence between two close bubbles without immediate detachment locally reduces the supersaturation and no bubble is formed on the original site immediately after detachment and iii) sometimes bubbles simply do not grow again on the same spot after detachment, probably as a consequence of local supersaturation levels being depleted (see Moreno Soto et al. [123]).

While depletion will be discussed in the following section, the limitation of the camera resolution becomes clear when comparing the total number of bubbles detected at a time of $t = 2\,\mathrm{min}$ with that at a time of $t = 5\,\mathrm{min}$. The total number of bubbles seems to increase from 2 min to 5 min, but this is attributed to the fact that some of the bubbles are too small to be detected at 2 min, but are detected at 5 min due to bubble growth.

Bubble growth

As pointed out by Enríquez et al. [117], the analytical solution for a spherical bubble in an unbounded liquid (assuming a constant bulk concentration) predicts that the bubble radius R_b increases according to $\sqrt{t}$. The differential equation describing the radius of such a bubble growing purely due to diffusion in an unbounded liquid is written as formulated by Epstein and Plesset [126]:

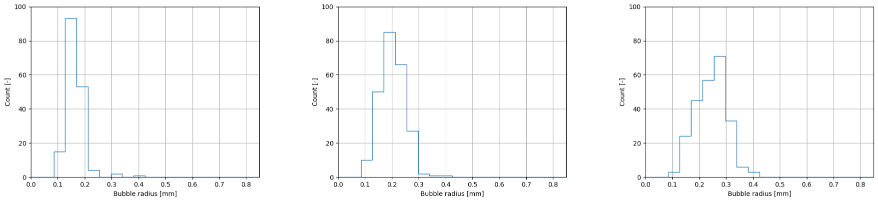

(a) $t = 2$ min (b) $t = 5$ min (c) $t = 10$ min

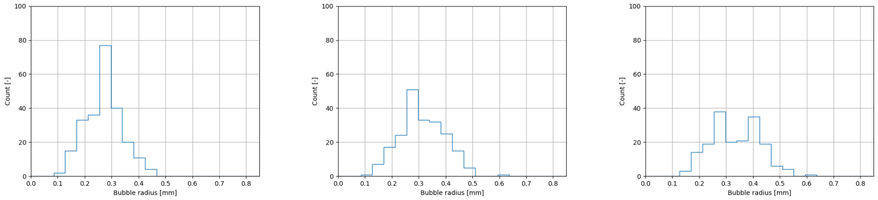

(d) $t = 15$ min (e) $t = 20$ min (f) $t = 25$ min

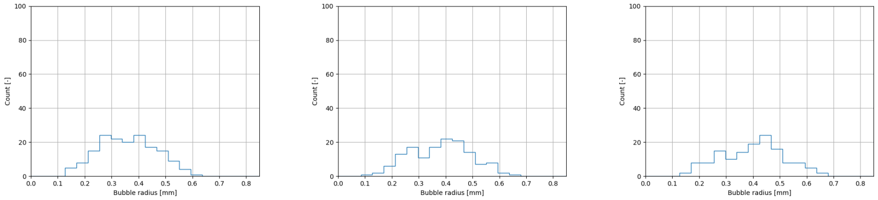

(g) $t = 30$ min (h) $t = 35$ min (i) $t = 40$ min

Figure 5.11: Bubble size distribution development over time for the surface with a pore size of 40 µm and supersaturation $\zeta = 0.16$.

$$\frac{dR_b}{dt} = \mathcal{D}\beta\left(\frac{1}{R_b} + \frac{1}{\sqrt{\pi\mathcal{D}t}}\right) \tag{5.4}$$

where $\beta = (c_0 - c_s)\rho_l/\rho_g MW$, $\mathcal{D} = 1.97 \times 10^{-9}\,\mathrm{m^2\,s^{-1}}$ is the diffusion coefficient of CO_2 in water, $\rho_l = 1000\,\mathrm{kg\,m^{-3}}$ is the liquid density, $\rho_l = 10.191\,\mathrm{kg\,m^{-3}}$ is the gas density at the experimental conditions (at P_s) and $MW = 44.01 \times 10^{-3}\,\mathrm{kg\,mol^{-1}}$ is the molecular weight of CO_2. The bulk (c_0) and saturation (c_s) concentrations are calculated from the Henry constant ($k_H = 3.79 \times 10^{-7}\,\mathrm{mol\,kg^{-1}\,Pa^{-1}}$ and from the pressure before the run and after the drop ($P_0 = 6.4$ bar and $P_s = 5.5$ bar).

To simplify the system, it is convenient to rewrite the equation in terms of dimensionless variables $R^* = R_b/R_0$ where R_0 is the initial bubble size and $x^* = \sqrt{(2\mathcal{D}\beta/R_0^2)t}$ is the square root of the dimensionless (Fourier) time. With these variables, a simplified (asymptotic) solution to Equation 5.4 is found as:

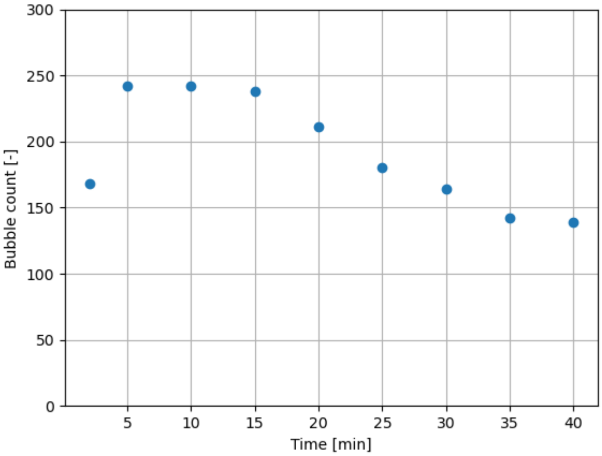

Figure 5.12: Total number of bubbles detected over time for the surface with a pore size of 40 µm and supersaturation $\zeta = 0.16$.

Table 5.2: Experimental bubble cases.

Case	**Description**
a	solitary bubble
b	solitary until $t \sim 15\,\mathrm{min}$
c	solitary after $t \sim 15\,\mathrm{min}$

$$R^* \approx \left[\gamma + (1+\gamma^2)^{1/2}\right] x^* \tag{5.5}$$

where the constant γ is calculated as $\gamma = \sqrt{\beta/2\pi}$. In addition, this solution is valid for an unbounded spherical bubble in a liquid, but the effect of the surface has to be taken into account. Enríquez et al. [124] provided a correction to the asymptotic solution in order to account for the reduced effective area through which gas can diffuse as a consequence of the surface. The solution proposed by them is thus:

$$R^* \approx \left[\gamma + (1/2+\gamma^2)^{1/2}\right] x^* \tag{5.6}$$

Table 5.2 shows three different selected experimental bubble cases from the experiment described in Section 5.5.1 to investigate their growth.

Figure 5.13a shows the two asymptotic solutions compared to the experimentally observed bubble growth for a somewhat solitary bubble on the surface (case *a*, see Table 5.2). It is very well visible that the bubble growth is not in line with the two asymptotic solutions, even with the one by Enríquez et al. [124] which accounts for the slower mass transfer as a consequence of the reduced area because of the presence of the substrate. It is nonetheless found that the

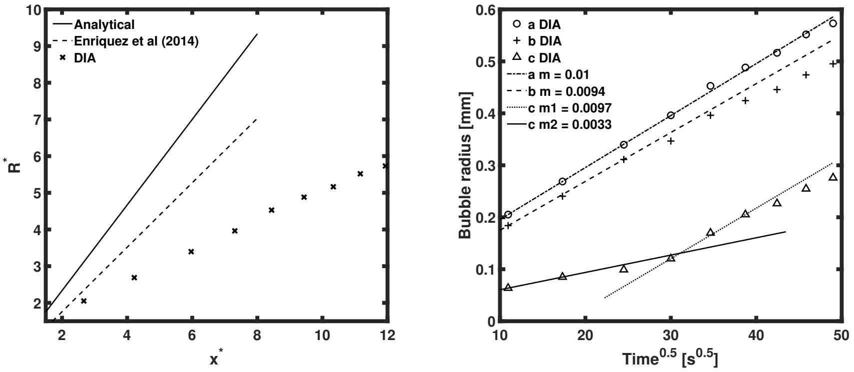

(a) (b)

Figure 5.13: Size of the bubble over time a) growth of bubble a compared to the theoretical prediction and b) comparison of different selected bubbles (cases a, b and c as explained in Table 5.2). The values of m refer to the slopes of the shown curves.

bubble growth is proportional to the square root of time, as expected, but with a much lower proportionality than expected (see Figure 5.13b).

Several possible explanations have been examined for this discrepancy:

i Effect of the non-spherical shape of the bubble

ii Effect of convection/advection

iii Effect of local depletion of CO_2

The first effect, the non-sphericity of the bubble shape, has been investigated analytically using a spherical cap model depending on the contact angle. As was also shown by Dietrich et al. [130] for a sessile droplet dissolving purely by diffusion, the expectations are that the Sherwood number remains in the order of $\mathrm{Sh}_d = 1$ for a reasonable span of contact angles, and the maximum reduction of mass transfer has been found to be about 5% of the analytical solution for a sphere, thus not accounting for the large difference found in the experimental work of this thesis. This is also confirmed by comparing with the adapted asymptotic solution of Enríquez et al. [124], as already mentioned.

The second effect has been shown to be present in the form of natural convection in the dissolution of a sessile droplet in Dietrich et al. [130] and responsible for the depletion between consequent bubbles in Moreno Soto et al. [123]. On the other hand, intuitively convective effects are expected to enhance the mass transfer rate.

Thus, the last effect is considered responsible for the observed reduced rate of mass transfer compared to the analytical solution by Epstein and Plesset [126]. As has been shown by Moreno Soto et al. [123], local depletion effects are responsible for the slowing down of the growth of subsequent bubbles from the same site, as well as for the reduced growth rate of two bubbles growing in the immediate vicinity. Thus, as we are accounting for a rather

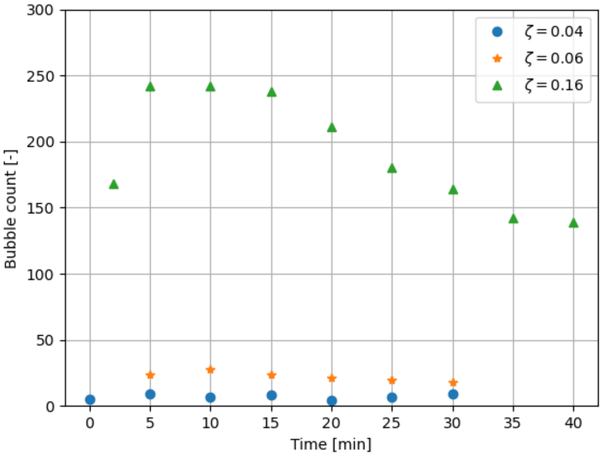

Figure 5.14: Total number of bubbles over time for different supersaturation ratios for the surface with a pore size of 40 µm.

large number of bubbles on the same surface, the effect of local depletion and stratification of the CO_2 concentration on the surface can reasonably expected to be there. On the other hand, more insights should be collected in future works.

The proportional growth to the square root of time is also visible (partially) for other bubbles, as shown in Figure 5.13b. It is quite noticeable that the bubbles in their solitary portion do follow the square root of time linearly with a proportionality constant (m) which is more or less the same for all three bubbles. On the other hand, they do deviate when there is competition for CO_2 when the bubble is close to other bubbles at the surface. This is visible for bubble c until it a time of $t \sim 15$ min and for bubble b after a time of $t \sim 15$ min, when they are no longer solitary but rather close to other bubbles. Here the behaviour starts to change, as competition starts to play a role. This was also noticed in the work of Enríquez et al. [117] where two bubbles growing side by side influence each other and the growth rate is slower.

5.5.2 Effect of supersaturation

The increase of supersaturation results in a net increase in the total number of bubbles formed (see Figure 5.14). This is consistent with the nucleation model presented by Battistella et al. [84], as an increase in supersaturation enables more nucleation sites to grow a bubble. Indeed, the ability to grow a bubble is directly related to the critical radius (see Equation 5.2) which is in turn decreasing with increasing values of supersaturation.

An additional effect of the supersaturation is the change of the mean bubble size. It was shown in Chapter 4 that a larger driving force makes bubbles grow faster and detach earlier. Unfortunately, the moment of detachment is not captured with the current configuration, since the very fast phenomenon of bubble detachment occurs virtually instantaneously, while the camera records images with a 5 min time span to accommodate the much slower bubble

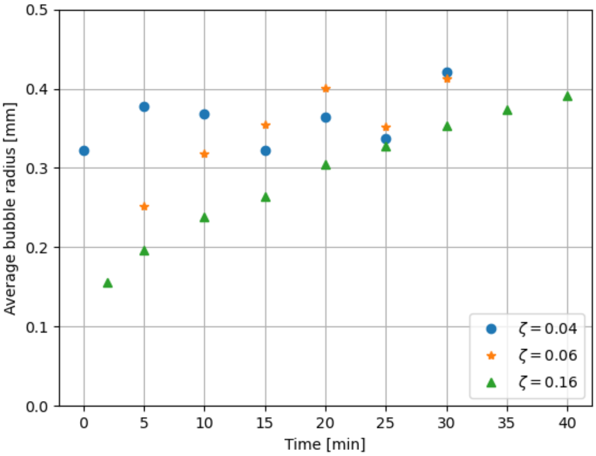

Figure 5.15: Average bubble size per image for different supersaturation ratios for the surface with a pore size of 40 µm.

growth process. On the other hand, the bubble size is readily available from the Digital Image Analysis, although a limited number of bubbles (only ~10 for the smallest supersaturation ratio) gives a somewhat limited statistical representation.

In Figure 5.15, the average bubble size (in millimeters) is shown. The dataset which gives more insight is probably the largest supersaturation ratio, as more bubbles are observed providing better statistics. It is visible that the average bubble size keeps increasing, as bubbles grow on the surface. Interestingly, despite the lower numbers which do not show a consistent statistical overview, the average bubble size for the lower supersaturation is in general higher. Although counterintuitive, due to the smaller supersaturation ratio only sites with a higher critical radius are able to grow a bubble, meaning on average bubbles with a larger radius are the only one able to be formed.

5.5.3 Effect of surface porosity

The results presented before were obtained using a porous steel with a pore size of 40 µm. To investigate the effect of the surface properties additional experiments were carried out with a metal plate with a larger average pore size (100 µm). First of all, it is important to underline that the larger pore size results in a coarser surface (more rough and corrugated), which is not coated very well with the black marker, thus resulting in a considerably larger noise, degrading drastically the DIA performances (see Figure 5.16).

Interestingly, the change in surface has a limited effect on the bubble count and the average bubble size. This can be discerned from Figure 5.17, where the change in the total number of bubbles and the average bubble radius is perfectly in line with the change in the supersaturation (note: the two cases have a slight variation of the supersaturation ratio, due to pressure/temperature control in the experiments). The results are similar to what was

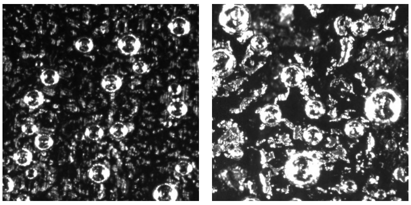

(a) 40 µm (b) 100 µm

Figure 5.16: Comparison of the noise produced by using a porous steel substrate with a: a) fine pore size (40 µm) and b) coarse pore size (100 µm).

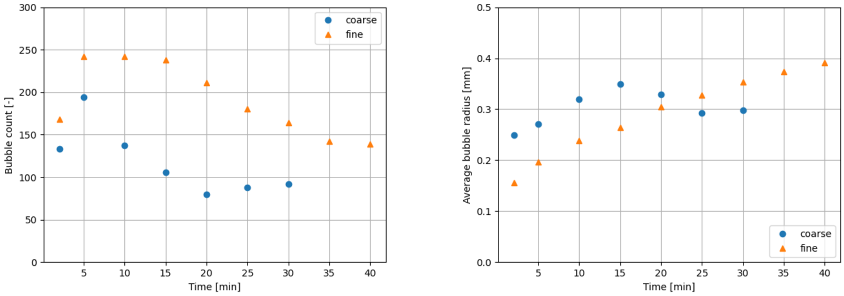

(a) (b)

Figure 5.17: Comparison of the a) number of bubbles and b) average bubble radius between a coarse (100 µm) and a fine (40 µm) surface. Note that the supersaturation ratios are different (0.092 for the coarse and 0.16 for the fine.)

observed before: the number of bubbles is indeed decreasing over time (the first increase is due to the DIA not detecting the smallest nucleating bubbles) and the total number of bubbles is lower on the coarse surface as a consequence of the smaller supersaturation. The bubble size seems slightly bigger at the beginning, but the subsequent decrease could be associated with a decrease in DIA accuracy due to the noise.

A possible explanation for why there is a rather limited effect of the surface roughness lies in the nature of the nucleation sites. When investigating the bubble size, it was noticed that the average bubble size is in the order of 400 µm. Using the Fritz radius as calculated with Equation 5.3 and assuming the detachment size is in this order of magnitude, it is possible to calculate the average pit radius, which corresponds to about 6 µm with $\sigma = 0.069\,\mathrm{N\,m^{-1}}$ (accounting for the presence of CO_2 [117]). This means that the used nucleation sites are not the pores of the steel but rather smaller crevices and cavities which are independent on the pore size.

5.5.4 Comparison with the model simulations

As described in Chapter 4, a nucleation model has been implemented in the DBM. For the comparison with the presented experimental data, the nucleation model has been separated from the Euler-Lagrange framework of the DBM by means of i) not tracking the bubbles once they detach (remove the Lagrangian part) and ii) imposing a bulk concentration instead of calculating the flow-field and species transport (remove the Euler part). In addition, immediate coalescence of bubbles is imposed when bubbles touch each other, as an infinite contact time is assumed. A random surface is generated with the maximum number of bubbles as the case described in Section 5.5.1. The average site radius and the standard deviation are deduced through fitting in order to mimic the bubble size distribution from the experiments.

A mass balance for all bubbles is solved as:

$$\rho_b \frac{dV_b}{dt} = k_l a \rho_l (Y_l - Y_l^*) \tag{5.7}$$

where the saturation mass fraction (Y_l^*) is calculated from Henry's coefficient ($k_H = 3.79 \times 10^{-7}\,\mathrm{mol\,kg^{-1}\,Pa^{-1}}$ at 21 °C) and the mass transfer regime is assumed to be totally diffusive. The mass transfer resistance inside the gas bubble is considered negligible as it is much smaller than the liquid phase resistance.

As visible in the comparison between Figure 5.18 and Figure 5.19, the model is able to describe the evolution of the bubble size distribution, although not entirely the widening of the distribution at $t = 40$ min. This best fit of the model has been chosen as a representation for the subsequent discussion, and it has been obtained with normally distributed nucleation sites with a mean radius of $\mu = 30\,\mu\mathrm{m}$ and a standard deviation of $\sigma = 10\,\mu\mathrm{m}$. In addition, the height of the nucleation sites has been fixed to a value of $H = 2R_0$ and the Sherwood number has been adapted in order to account for the slower mass transfer rates (found in Section 5.5.1) to a mean value of $\mathrm{Sh} = 0.4$ and also normally distributed with a standard deviation of $\sigma = 0.1$ in order to mimic different grow rates for different bubbles as a consequence of competition and local depletion.

Effect of the site radius

The radius of the nucleation site has a very pronounced effect on the bubble size distribution: it determines the Fritz radius, and thus the maximum size the bubble can reach.

In addition, the model explained in Chapter 4 assumes that a certain variability (i.e. a normal distribution of nucleation site radii) is present, as it is visible in the images at a time of $t = 2$ min that bubble sizes differ already at the very early stages. Interestingly, the effect of the standard deviation in the nucleation site radius is not very pronounced, as shown in the comparison in Figure 5.20, where the distribution at a time of $t = 40$ min is shown for the case with a standard deviation of $\sigma = 10\,\mu\mathrm{m}$ and the case with a uniform site distribution. Moreover, despite the absence of a distribution in site radii, the small variability of the bubble size at a time of $t = 2$ min is maintained, most probably as a consequence of the induced differences in mass transfer rates.

On the other hand, the mean value for the nucleation site radii has a great effect on the evolution of the bubble size distribution. In Figure 5.21 the distribution at a time of $t = 40$ min is shown for three different site radii (without distribution). A smaller site causes a much

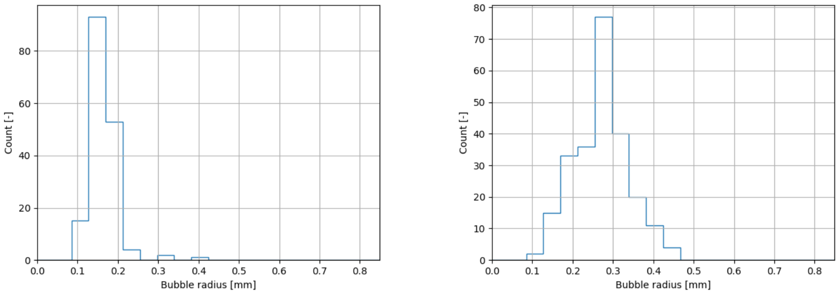

(a) $t = 2$min

(b) $t = 15$min

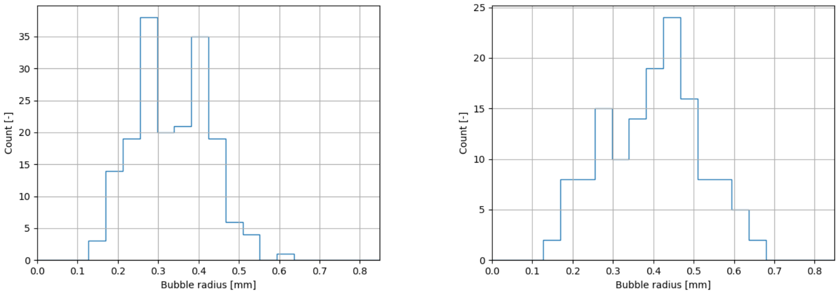

(c) $t = 25$min

(d) $t = 40$min

Figure 5.18: Bubble size distribution (in mm) development over time for the experiment.

earlier detachment of the bubble, while at a larger nucleation site the attached bubble can reach a size that is not observed in the experiments because of the increased Fritz radius.

Effect of the site depth

The nucleation sites also have an associated depth. In the model of Chapter 4, this has been assumed as distributed randomly and with equal probability between 0.5 and 1.5 the nucleation site radius. To connect with the experiments, where inactive sites are not visible, assuming a contact angle of $\beta = 90\,^\circ$, the site depth has been varied from $H = 1.1R_0$ to $H = 5R_0$, as a depth equal to the site radius will impose that no gas pocket can be formed (geometrically, see Chapter 4 for further details).

Figure 5.22 shows the net effect of the site depth. It is very well visible that the model is not very sensitive to the site depth, unless a very shallow depth ($H \leq R_0$) is used where no gas pocket is formed, which is not the case here as this is not visible from the experiments.

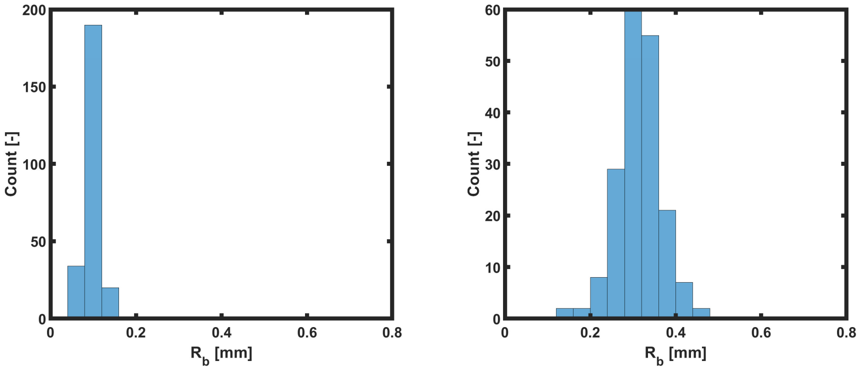

(a) t = 2min

(b) t = 15min

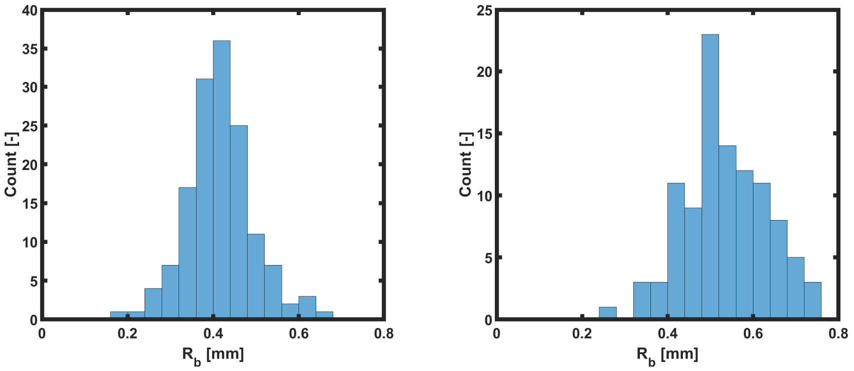

(c) t = 25min

(d) t = 40min

Figure 5.19: Bubble size distribution (in mm) development over time: model predictions.

Sherwood number

Although the presence of coalescence is able to widen the bubble size distribution, the actual width is due to different bubble growth rates. Indeed, a normally distributed Sherwood number has been introduced and fitted in order to mimic the effect of local depletion/competition, as it was seen that some bubbles exhibited slower grow rates due to the presence of neighboring bubbles. This has a large effect on the width of the bubble size distribution, as some bubbles simply lag behind while others grow faster.

Figure 5.23 shows the effect of the induced distribution of Sherwood numbers. If no distribution is included (Sh = 0.4), then a front of bubbles is growing with some bubbles at higher sizes because they coalesced before. The distribution does not widen and flatten, because bubbles grow more or less at the same rate. In conclusion, it is very important to underline that further studies on the effect of local depletion/slower mass transfer rates is

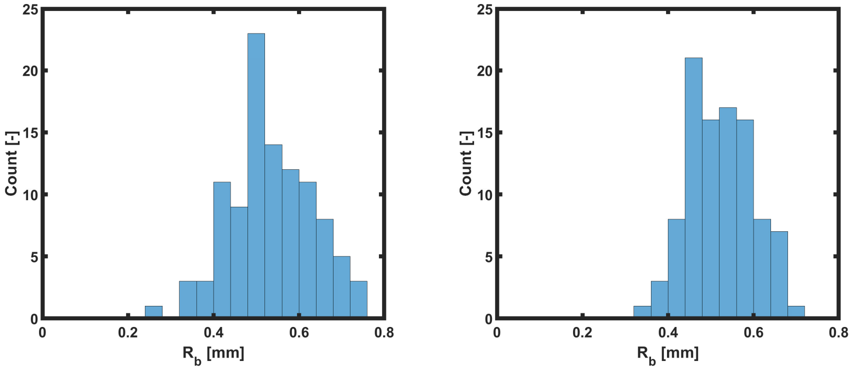

(a) (b)

Figure 5.20: Comparison of bubble size distribution (in mm) at a time of $t = 40$ min for a) the case with a standard deviation of nucleation site radii of $\sigma = 10\,\mu\text{m}$) and b) no distribution of nucleation site radii.

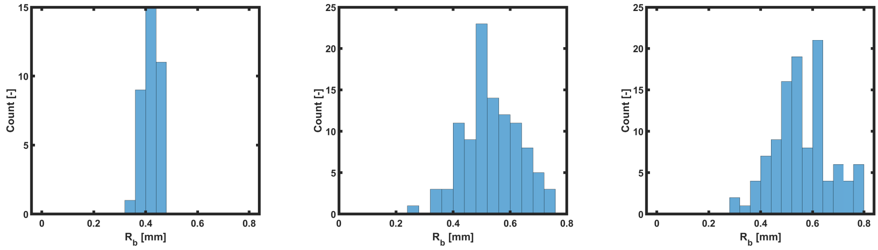

(a) (b) (c)

Figure 5.21: Comparison of bubble size distribution (in mm) at a time of $t = 40$ min for a) the case with a nucleation site radius of $R_0 = 10\,\mu\text{m}$); b) site radius of $R_0 = 30\,\mu\text{m}$) and c) site radius of $R_0 = 50\,\mu\text{m}$).

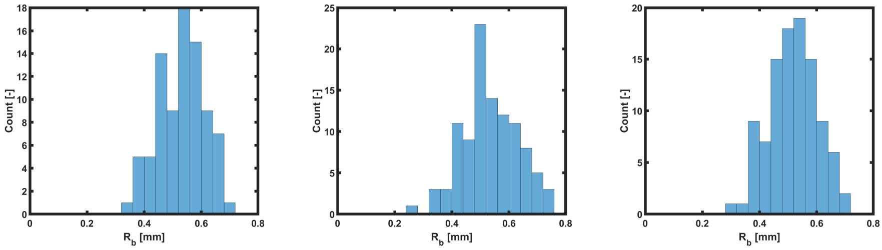

(a) (b) (c)

Figure 5.22: Comparison of bubble size distribution (in mm) at a time of $t = 40\,\text{min}$ for a) the case with a nucleation site depth of $H = 1.1R_0$); b) site depth of $H = 2R_0$) and c) site depth of $H = 5R_0$).

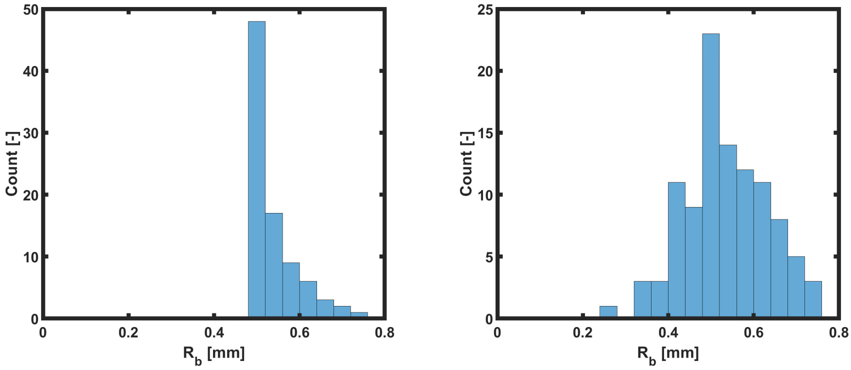

(a) (b)

Figure 5.23: Comparison of bubble size distribution (in mm) at a time of $t = 40\,\text{min}$ for a) a fixed Sherwood number Sh = 0.4 and b) a normally distributed Sherwood number $\sigma = 0.1$ with mean $\mu = 0.4$.

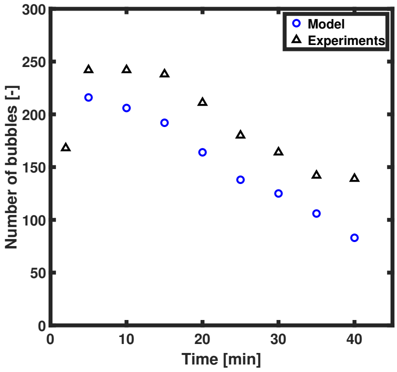

Figure 5.24: Comparison of the total number of bubbles over time for the model predictions and the experimental findings, for the best fit case shown in Section 5.5.4.

required to understand the underlying physics.

Final considerations

In conclusion, the model is able to describe the bubble size distribution at the surface after a tuning of several nucleation parameters. On the other hand, several parameters have not been considered here, such as the contact angle between the surface and the gas liquid interface and the effect of the change of surface tension due to the colored marker.

An additional effect which is of extreme importance is the depletion effect on the formation of subsequent bubbles. To obtain the experimental bubble size distribution and the correct number of bubbles (see Figure 5.24), it is important to switch off subsequent bubble nucleations in the model from the same site. This is also observed in the experiments, where only a handful of sites are seen growing a bubble right after another one has detached. To conclude, this needs further investigation in future works.

5.6 Conclusions and outlook

This chapter discussed the experimental work performed to investigate bubble nucleation and growth caused by supersaturation on porous steel surfaces, and compared the results with simulations using the nucleation model from Chapter 4. An experimental setup has been built in order to obtain a supersaturated water-carbon dioxide solution under pressure. When the pressure is released, the solution becomes supersaturated and experimental images of growing bubbles on a surface could be taken.

A Digital Image Analysis technique has been adapted and validated for the specific surface, both with artificially generated and experimentally obtained images. The DIA is able to effectively detect bubbles and their sizes, although attention has to be given to accurate noise removal from the reflecting steel surface. In addition, the DIA requires manual fine-tuning of the parameters (thresholds and Hough transform parameters) in order to perform accurately, making it not very robust when changing settings. A future work is dedicated to the implementation of a deep learning DIA, which could potentially solve this problem.

Corresponding to the model simulations described in Chapter 4, a clear initial growing stage is visible where a front of bubbles grow more or less equally. When coalescence and detachment events start taking place, the bubble size distribution flattens and widens, as more bubbles of different size are in different stages of growth. In addition, the total number of bubbles decreases over time, as a consequence of coalescence, depletion and the limitation of the camera resolution, making bubbles in the very early stages of growth undetectable.

The growth rate of bubbles over time corresponds to the well-known analytical proportionality to the square root of time, but with a much lower mass transfer compared to the analytical solution by Epstein and Plesset [126]. This has been attributed partially to the effect of the surface reducing the effective area for mass transfer and also to local depletion effects.

Supersaturation is shown to have two main effects: a) a larger number of bubbles grow at higher supersaturation because of the increased number of sites able to grow a bubble (the critical radius is smaller) and b) the average bubble size is smaller as a consequence of the smaller critical radius allowing smaller bubbles to grow. A change in average pore size of the surface, on the other hand, does not seem to have a pronounced effect on the nucleation process. This is attributed to the nucleation sites being smaller than the pore size in both cases, meaning inner cavities and crevices of the corrugated surface are used rather than the whole pore.

A simplified version of the nucleation model of Chapter 4 has been setup in order to investigate the performance of the model and the obtained experimental data. The model is able to describe the evolution of the bubble size distribution with a limited effect of site properties, apart from the site radius, determining the detachment Fritz radius. It is of great importance to include a certain variability (normally distributed) of the Sherwood number, to account for bubbles growing at different rates because of the presence of neighboring bubbles.

To conclude, further studies should be dedicated to further investigate this depletion/competition effect and how local depletion can cause bubbles to delay/stop nucleating from the same site. In addition, more research can be dedicated to investigate nucleation at different surfaces and to the understanding of all the possible effects of surface properties. For instance, surfaces with controlled nucleation sites (as was shown in Enríquez et al. [117]) could be used, as well as studies on the effect of contact angle and wetting dynamics.

CHAPTER 6

EPILOGUE

Previous chapters focused on three blind spots identified in the state-of-the-art when it comes to simulating bubbly flows for different applications at the meso-scale with Euler-Lagrange models: i) the behavior of bubbles in non-Newtonian liquids and their drag coefficient; ii) accurate sharp tracking of the free surface in Euler-Lagrange models and iii) heterogeneous bubble nucleation due to phase transfer. In this chapter, the relevant conclusions are presented and it shown how these features can be integrated in larger scale simulations. The DBM can be a useful tool to simulate bubbly flows, but much more need to be done. First, for each of the three topics studied in this thesis, it is necessary to continue the work started, in order to expand our fundamental understanding. For example, preliminary calculations at a larger scale show the influence of the liquid rheology, which should be further investigated. In addition, the extension to larger scales cannot be done without the optimization of the parallel capabilities of the DBM. To conclude, the DBM can be used for other challenges, such as the development of closures for higher scale models.

Conclusions

Industrial processes often involve bubbles, and bubbly flows, which present a challenge due to the complex interactions between the hydrodynamics and mass transport with chemical reaction. Examples of complex systems involving the formation of bubbles are bubble column reactors, fermentors (bio-reactors) and electrolytic processes as water splitting for hydrogen production.

In order to improve the fundamental understanding of these complex systems, Computational Fluid Dynamics has proven to be a valuable tool to simulate, understand and aid the design and optimization of industrial processes, especially when limited experimental data are available. In this framework, the use of more detailed models such as the Euler-Lagrange Discrete Bubble Model (DBM) proves to be useful in providing insights in the bubble dynamics while including relevant physical phenomena. In addition, with the increase of computer power, it is foreseeable that the industrial scale can be achieved with what is nowadays considered a meso-scale model.

In particular, the focus of this thesis is dedicated to the investigation of three aspects, which are relevant for many different processes involving bubbly flows with the aim of further improving the capabilities of the Euler-Lagrange Discrete Bubble Model (DBM). The three challenges identified in this thesis are: i) the analysis of the behaviour and the derivation of a drag coefficient closure for bubbles rising in non-Newtonian power-law liquids (as for instance in an industrial fermentor); ii) the inclusion of a sharp and accurate interface between the top gas freeboard and the liquid in Euler-Lagrange models for bubbly flows and iii) the heterogeneous nucleation of bubbles as a consequence of local supersaturation, as for instance in electrolytic processes. The main findings of this thesis are summarized below:

- In Chapter 2, a Front-Tracking detailed model has been used to show that the drag coefficient of single bubbles rising in non-Newtonian power-law fluids can be captured well with a correlation for the drag coefficient originally derived for Newtonian fluids when using a modified Reynolds number to account for the non-Newtonian apparent viscosity. In addition, it was found that the non-Newtonian rheology acts on the bubble shape and rise velocity, where bubbles rising in shear-thickening fluids become more spherical and rise slower.

- In Chapter 3, a Front-Tracking Free Surface was incorporated in the Discrete Bubble Model to simulate the interface between the liquid and the top gas freeboard. The chapter shows an extensive validation of the implementation, which shows great stability even at high deformations. This numerical representation of the free surface improves the prediction of break-up rates close to the surface, compared to the fictitious fixed boundary conditions often adopted before.

- In Chapter 4, a heterogeneous nucleation model has been implemented in the DBM, assuming conical nucleation sites as cavities, to simulate bubble formation as a consequence of supersaturation. A clear first wave of bubbles slowly growing attached to the substrate is visible, with the formation of a depletion layer, while the bubble size distribution widens and flattens as soon as bubbles start to detach and grow further in the column and coalescence starts occurring. A higher number of bubbles is visible at higher supersaturation ratios, with a faster bubble growth.

- In Chapter 5, a dedicated experimental setup is presented, where a supersaturated solution is prepared and bubbles can form on a specific substrate material. In addition, a Digital Image Analysis technique has been presented and validated, in order to accurately detect growing bubbles attached to the surface. A clear wave is visible at the beginning of the nucleation process, corresponding with the model results. In addition, the mass transfer rate is found to be following the expected square root dependency on time, but with a much slower rate than the theoretical one for spherical bubbles with pure diffusive growth. The widening and flattening of the bubble size distribution has to be attributed to local differences in the mass transfer rate for each of the bubbles, probably as a consequence of competition/local depletion effects.

Outlook

This thesis laid the foundations of some relevant building blocks for the simulation of a variety of processes involving bubbly flows using a deterministic Discrete Bubble Model. Nonetheless, this is just the start of several interesting possibilities offered by such a model. Below a few examples are described.

Large-scale non-Newtonian simulations

The developed drag closure is the start of two different lines of work. On the one hand, the Front-Tracking model can be used further to develop closures. As it is shown by Roghair et al. [7], the Front-Tracking technique is an authoritative tool to develop a closure for a swarm of bubbles: indeed, the presence of other bubbles influences the drag coefficient of the swarm. In addition, the non-Newtonian rheology is known to give place to alignment, clustering and preferential paths for the bubbles, as a consequence of the viscosity changes. Moreover, the inclusion of more complex types of fluid is relatively straightforward, allowing to investigate the effect of visco-elastic liquids (as polymers) and other complex rheologies, as long as they can be accounted for in the continuous phase description used in the FT model.

On the other hand, the developed closure (without swarm effects) has already been implemented in the DBM, opening the path for the investigation of large-scale effects of the non-Newtonian rheology. A preliminary calculation is performed with a column twice the size of the column used by Deen [71]: the numerical setup is a rectangular column of $30 \times 30 \times 90\,\mathrm{cm}$ with injection of 4 mm bubbles from the bottom through 196 nozzles placed in a square at the center, with a superficial gas velocity of $4.9\,\mathrm{mm\,s^{-1}}$ (for an overview of other parameters of the Deen case see Table 3.2 and Table 3.3). This already results in an order of $O(10^4)$ bubbles, slowing down the simulation considerably but still within reasonable limits. In this preliminary study the effect of the non-Newtonian rheology is introduced in the DBM, by simulating a Newtonian liquid with a viscosity of $10^{-2}\,\mathrm{Pa\,s}$ and two power-law liquids with a consistency index $K = 10^{-2}\,\mathrm{Pa\,s}^n$ and flow behaviour index $n = 1.1$ for the shear-thickening case and $n = 0.9$ for the shear-thinning case.

This exercise shows a number of interesting effects of the liquid rheology on the behaviour of the rising plume. The first effect is that the number of bubbles decreases at the same time

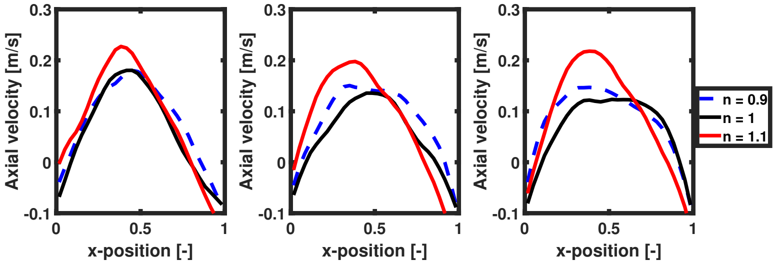

Figure 6.1: Time averaged axial liquid velocity profiles at three different heights in the column: a) 30 cm, b) 50 cm and c) 70 cm.

$t = 100$ s of simulation while increasing the flow behaviour index. The number of bubbles decreases from ≈ 19000 for $n = 0.9$, to ≈ 16000 for the newtonian case and ≈ 15000 for $n = 1.1$. This is probably related with the change in viscosity, which changes the residence time and alters the flow behaviour (*e.g.* in the shear-thickening case, bubbles are slowed down and might be closer to each other resulting in more coalescence events).

The change in viscosity alters the time-averaged lateral profiles of the axial liquid velocity as well (see Figure 6.1). Although this case is only preliminary (averaging time should be longer than 100 s, to average the plume meandering and a grid convergence analysis has to be performed), it shows how the flow behaviour is affected by the rheology. In particular, the shear-thickening case shows a narrower plume, visible also from the narrower liquid velocity profile. On the other hand, it counterintuitively shows a somehow faster liquid velocity in the center of the column, which should be further investigated.

To conclude, it is interesting to note that the viscosity profile shows macro-scale circulation patterns following the flow, as visible in Figure 6.2. In this figure, an instantaneous snapshot of the viscosity profile for the shear-thickening case shows how the circulation pattern clearly follows the motion of the bubbles. Indeed, as expected, bubbles induce shear while rising and higher viscosity regions are found where the liquid flow circulates back creating a vortex. These preliminary calculations show how the liquid rheology influences the large scale dynamics of bubbles, which is a relevant topic for further studies.

Free surface dynamics

The Free Surface technique developed in this thesis can be further extended and used for several other types of studies. For instance, a dedicated coalescence model can be included for bubbles merging with the top surface, with the inclusion of a bubble transition algorithm from the discrete Lagrangian phase to the Front-Tracking model, similar to the model by Li et al. [31]. Additionally, foaming can be studied if no merging is included.

Supersaturation

The studies on supersaturation presented both in the DBM's nucleation model and with the dedicated experimental setup, can be further expanded. The model can account for different surfaces and should be improved with local depletion effects obtained from the experiments. The effect of the contact angle can be of interest, together with the further extension to

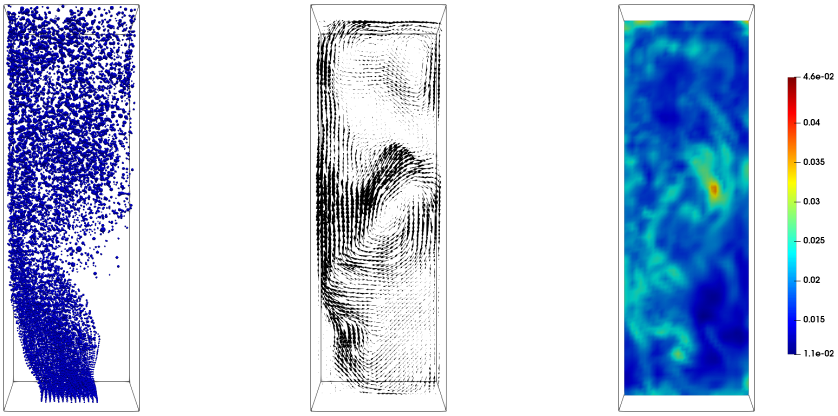

(a) (b) (c)

Figure 6.2: Instantaneous snapshots of a) bubble positions; b) velocity profile and c) viscosity profile for the shear-thickening $n = 1.1$ case.

different systems where bubble formation occur, such as electrolytic processes. Moreover, nucleation on impurities present in the liquid bulk can be accounted for.

A preliminary simulation has been carried out using the column twice the size of the one by Deen [71] with a simple fermentation reaction implemented as a demonstration case. The reaction is approximated as first order glucose fermentation reaction (with a purely demonstrative kinetics) which produces CO_2, which is then escaping the system through the nucleation of gas bubbles. As shown in Figure 6.3, even at this scale the layering and stratification of the concentration of CO_2 in the liquid can be discerned, which clearly has an impact in the early stages of the reaction where mixing is minimal. Of course, this simple numerical experiment should be taken as the base for further development of the DBM towards the simulation of industrial processes: the actual kinetics of fermentation or electrolysis can be implemented and effects such as the mixing induced by the bubble circulation, the effect of phase transition or the surface coverage can be further investigated.

To conclude, further development and use of the experimental setup can be performed. Preliminary calculations within the research group showed the applicability of deep learning techniques to Digital Image Analysis, which is promising to improve the robustness of the data analysis. In addition, further experiments with different surfaces should be performed to continue this line of study, especially concerning depletion effects affecting the growth of bubbles attached to the substrate.

Development of closures for larger scale models

The DBM provides as a result of the computation the position, size and velocity of all individual bubbles, allowing for accurate tracking of bubble collision events. This deterministic description can be used to aid the formulation of closures for larger scale models, such as the Euler-Euler model with Population Balance Modeling (PBM). In such systems, a transport

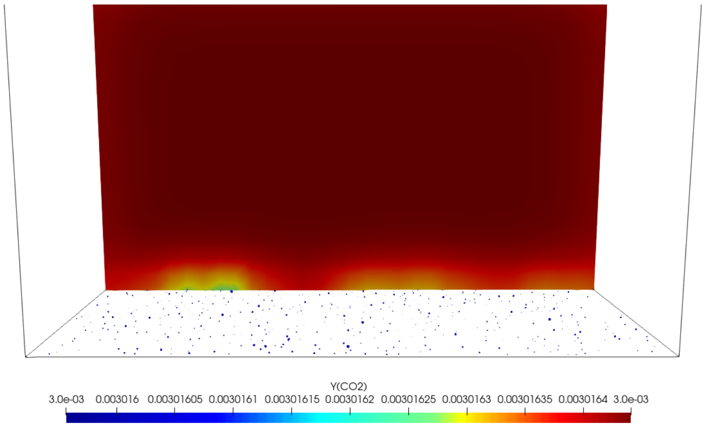

Figure 6.3: Snapshot of the CO_2 mass fraction in the early stages of nucleation during fermentation showing a clear depletion layer at the bottom surface.

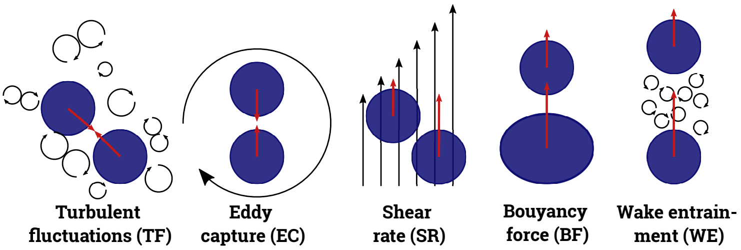

Figure 6.4: Depiction of the different mechanisms usually included for the collision frequency kernels in PBM modeling. Adapted from Falzone et al. [140].

equation for the number density function (in principle a function of the bubble size and time) is introduced and solved [139] with various methods, such as the Conditional Quadrature Based Method of Moment (CQMOM) in OpenFOAM by Buffo et al. [139].

In the population balance equation, a generation term due to discontinuous events, as coalescence and break-up, is introduced. The so-called kernel for coalescence includes a statistical description of the coalescence process, which usually is a function of the *collision frequency*. Normally, different mechanisms are accounted for to estimate the collision frequency, such as turbulence, eddy capture, buoyancy effects, wake entrapment, shear flows *etc* (see Figure 6.4). The DBM has great potential to verify model assumptions, develop closures for the kernels for these specific situations and in the understanding of the interactions (usually approximated as additive). Moreover, bubbles can collide as a consequence of more than one mechanism, which is currently not accounted for in the traditional population balance kernels.

Other plans

To conclude, a careful future development of the DBM has to go towards the optimization of the parallel capabilities of the solver, in order to increase the potential size of the system and reach actual industrial scale. The DBM can be extended to include different reactions and be dedicated to the study of a process, such as the study of electrolytic processes, where bubbles form on electrodes, using the nucleation model of the DBM or an industrial bio-reactor where fermentation forms bubbles. In any case, the DBM has shown its potential to include different phenomena and can bridge the gap between very detailed simulations (DNS) and large-scale Euler-Euler simulations, and the current development is going towards reaching a larger scale in shorter times, making the DBM even more valuable.

REFERENCES

[1] D. Darmana, “On the multiscale modelling of hydrodynamics, mass transfer and chemical reactions in bubble columns,” Ph.D. dissertation, Universiteit Twente, the Netherlands, 2006.

[2] D. Jain, “Cutting bubbles, discrete bubble modeling of a micro-structured bubble column,” Ph.D. dissertation, Eindhoven University of Technology, the Netherlands, 2015.

[3] N. G. Deen, M. van Sint Annaland, and J. A. M. Kuipers, “Multi-scale modeling of dispersed gas-liquid two-phase flow,” *Chem. Eng. Sci.*, vol. 59, no. 8-9, pp. 1853–1861, 2004.

[4] M. van Sint Annaland, N. G. Deen, and J. A. M. Kuipers, *Multi-level modeling of dispersed gas-liquid two-phase flows*, ser. Heat and mass transfer, M. Sommerfeld and D. Mewes, Eds. Springer, Berlin, 2003.

[5] Y. M. Lau, I. Roghair, N. G. Deen, M. van Sint Annaland, and J. A. M. Kuipers, “Numerical investigation of the drag closure for bubbles in bubble swarms,” *Chemical Engineering Science*, vol. 66, no. 14, pp. 3309–3316, 2011.

[6] W. Dijkhuizen, I. Roghair, M. van Sint Annaland, and J. A. M. Kuipers, “DNS of gas bubbles behaviour using an improved 3D front tracking model–Drag force on isolated bubbles and comparison with experiments,” *Chem. Eng. Sci.*, vol. 65, no. 4, pp. 1415–1426, 2010.

[7] I. Roghair, Y. M. Lau, N. G. Deen, H. M. Slagter, M. W. Baltussen, M. van Sint Annaland, and J. A. M. Kuipers, “On the drag force of bubbles in bubble swarms at intermediate and high Reynolds numbers,” *Chemical Engineering Science*, vol. 66, no. 14, pp. 3204–3211, 2011.

[8] D. Darmana, N. G. Deen, and J. A. M. Kuipers, “Detailed modeling of hydrodynamics, mass transfer and chemical reactions in a bubble column using a discrete bubble model,” *Chemical Engineering Science*, vol. 60, no. 12, pp. 3383–3404, 2005.

[9] D. Jain, J. A. M. Kuipers, and N. G. Deen, “Numerical study of coalescence and breakup in a bubble column using a hybrid volume of fluid and discrete bubble model approach,” *Chemical Engineering Science*, vol. 119, pp. 134–146, 2014.

[10] N. G. Deen, T. Solberg, and B. H. Hjertager, “Large eddy simulation of the gas–liquid flow in a square cross-sectioned bubble column,” *Chemical Engineering Science*, vol. 56, no. 21, pp. 6341–6349, 2001, proceedings of the 5th International Conference on Gas-Liquid and Gas-Liquid-Solid Reactor Engineering.

[11] S. Kamath, M. V. Masterov, J. T. Padding, K. A. Buist, M. W. Baltussen, and J. A. M. Kuipers, “Parallelization of a stochastic euler-lagrange model applied to large scale dense bubbly flows,” *Journal of Computational Physics: X*, vol. 8, p. 100058, 2020.

[12] J. Sanyal, D. L. Marchisio, R. O. Fox, and K. Dhanasekharan, “On the comparison between population balance models for CFD simulation of bubble columns,” *Industrial & Engineering Chemistry Research*, vol. 44, no. 14, pp. 5063–5072, 2005.

[13] D. L. Marchisio and R. O. Fox, “Solution of population balance equations using the direct quadrature method of moments,” *Journal of Aerosol Science*, vol. 36, no. 1, pp. 43–73, 2005.

[14] E. Delnoij, J. A. M. Kuipers, and W. P. M. van Swaaij, “A three-dimensional CFD model for gas-liquid bubble columns,” *Chemical Engineering Science*, vol. 54, no. 13-14, pp. 2217–2226, 1999.

[15] Y. M. Lau, W. Bai, N. G. Deen, and J. A. M. Kuipers, “Numerical study of bubble break-up in bubbly flows using a deterministic Euler-Lagrange framework,” *Chemical Engineering Science*, vol. 108, pp. 9–22, 2014.

[16] C. Webb, F. Que, and P. R. Senior, “Dynamic simulation of gas-liquid dispersion behaviour in a 2-D bubble column using a graphics mini-supercomputer,” *Chemical Engineering Science*, vol. 47, no. 13, pp. 3305–3312, 1992.

[17] A. Lapin and A. Lübbert, “Numerical simulation of the dynamics of two-phase gas—liquid flows in bubble columns,” *Chemical Engineering Science*, vol. 49, no. 21, pp. 3661–3674, 1994.

[18] M. Sommerfeld, E. Bourloutski, and D. Bröder, “Euler/Lagrange calculations of bubbly flows with consideration of bubble coalescence,” *The Canadian Journal of Chemical Engineering*, vol. 81, no. 3-4, pp. 508–518, 2003.

[19] S. Laín, D. Bröder, M. Sommerfeld, and M. F. Göz, “Modelling hydrodynamics and turbulence in a bubble column using the euler–lagrange procedure,” *International Journal of Multiphase Flow*, vol. 28, no. 8, pp. 1381–1407, 2002.

[20] C. Laborde-Boutet, F. Larachi, N. Dromard, O. Delsart, and D. Schweich, “CFD simulation of bubble column flows: Investigations on turbulence models in RANS approach,” *Chemical Engineering Science*, vol. 64, no. 21, pp. 4399–4413, 2009.

[21] S. Radl and J. G. Khinast, “Multiphase flow and mixing in dilute bubble swarms,” *AIChE Journal*, vol. 56, no. 9, pp. 2421–2445, 2010.

[22] C. Haringa, W. Tang, G. Wang, A. T. Deshmukh, W. A. van Winden, J. Chu, W. M. van Gulik, J. J. Heijnen, R. F. Mudde, and H. J. Noorman, "Computational fluid dynamics simulation of an industrial p. chrysogenum fermentation with a coupled 9-pool metabolic model: Towards rational scale-down and design optimization," *Chemical Engineering Science*, vol. 175, pp. 12–24, 2018.

[23] J. Xia, G. Wang, M. Fan, M. Chen, Z. Wang, and Y. Zhuang, "Understanding the scale-up of fermentation processes from the viewpoint of the flow field in bioreactors and the physiological response of strains," *Chinese Journal of Chemical Engineering*, vol. 30, pp. 178–184, 2021.

[24] S. Chatterjee and S. Venkata Mohan, "Refining of vegetable waste to renewable sugars for ethanol production: Depolymerization andfermentation optimization," *Bioresource Technology*, p. 125650, 2021.

[25] S. Greses, E. Tomás-Pejó, and C. González-Fernández, "Short-chain fatty acids and hydrogen production in one single anaerobic fermentation stage using carbohydrate-rich food waste," *Journal of Cleaner Production*, vol. 284, p. 124727, 2021.

[26] R. Rashid, I. Shafiq, P. Akhter, M. J. Iqbal, and M. Hussain, "A state-of-the-art review on wastewater treatment techniques: the effectiveness of adsorption method," *Environmental Science and Pollution Research*, vol. 28, no. 8, pp. 9050–9066, Feb 2021.

[27] C. Haringa, W. Tang, A. T. Deshmukh, J. Xia, M. Reuss, J. J. Heijnen, R. F. Mudde, and H. J. Noorman, "Euler-lagrange computational fluid dynamics for (bio)reactor scale down: An analysis of organism lifelines," *Engineering in Life Sciences*, vol. 16, no. 7, pp. 652–663, 2016.

[28] X. Miao, D. Lucas, Z. Ren, S. Eckert, and G. Gerbeth, "Numerical modeling of bubble-driven liquid metal flows with external static magnetic field," *International Journal of Multiphase Flow*, vol. 48, pp. 32–45, 2013.

[29] S. S. Deshpande, L. Anumolu, and M. F. Trujillo, "Evaluating the performance of the two-phase flowsolver interFoam," *Computational Science and Discovery*, vol. 5, p. 014016, 2012.

[30] D. L. Youngs, "Time-dependent multi-material flow with large fluid distortion," in *Numerical Methods for Fluid Dynamics*, K. W. Morton and M. J. Bianes, Eds. Academic Press, New York, 01 1982, pp. 273–285.

[31] L. Li, W. Ding, F. Xue, C. Xu, and B. Li, "Multiscale mathematical model with discrete–continuum transition for gas–liquid–slag three-phase flow in gas-stirred ladles," *JOM*, vol. 70, pp. 2900–2908, 2018.

[32] L. Li and B. Li, "Investigation of bubble-slag layer behaviors with hybrid Eulerian–Lagrangian modeling and Large Eddy Simulation," *JOM*, vol. 68, pp. 2160–2169, 2016.

[33] L. Li, Z. Liu, M. Cao, and B. Li, “Large Eddy Simulation of bubbly flow and slag layer behavior in ladle with Discrete Phase Model (DPM)–Volume of Fluid (VOF) coupled model,” *JOM*, vol. 67, pp. 1459–1467, 2015.

[34] A. Volanschi, D. Oudejans, W. Olthuis, and P. Bergveld, “Gas phase nucleation core electrodes for the electrolytical method of measuring the dynamic surface tension in aqueous solutions,” *Sensors and Actuators B*, vol. 35-36, pp. 73–79, 1996.

[35] H. F. A. Verhaart, R. M. de Jonge, and S. J. D. van Stralen, “Growth rate of a gas bubble during electrolysis in supersaturated liquid,” *International Journal of Heat and Mass Transfer*, vol. 23, no. 3, pp. 293 – 299, 1980.

[36] E. Askari, P. Proulx, and A. Passalacqua, “Modelling of bubbly flow using CFD-PBM solver in OpenFOAM: Study of local population balance models and extended quadrature method of moments applications,” *ChemEngineering*, vol. 2, no. 1, 2018.

[37] H. Liu, L.-m. Pan, and J. Wen, “Numerical simulation of hydrogen bubble growth at an electrode surface,” *The Canadian Journal of Chemical Engineering*, vol. 94, no. 1, pp. 192–199, 2015.

[38] A. Battistella, S. J. G. van Schijndel, M. W. Baltussen, I. Roghair, and M. van Sint Annaland, “On the terminal velocity of single bubbles rising in non-Newtonian power-law liquids,” *Journal of Non-Newtonian Fluid Mechanics*, vol. 278, p. 104249, 2020.

[39] W. A. Al-Masry, “Effect of scale-up on average shear rates for aerated non-Newtonian liquids in external loop airlift reactors.” *Biotechnology and bioengineering*, vol. 62, no. 4, pp. 494–498, feb 1999.

[40] H. Z. Li, “Bubbles in non-Newtonian fluids: Formation, interactions and coalescence,” *Chemical Engineering Science*, vol. 54, no. 13-14, pp. 2247–2254, jul 1999.

[41] R. Darby and R. P. Chhabra, *Chemical Engineering Fluid Mechanics, Third Edition*. CRC Press, 2016.

[42] I. Roghair, M. van Sint Annaland, and J. A. M. Kuipers, “Drag force and clustering in bubble swarms,” *AIChE Journal*, vol. 59, no. 5, pp. 1791–1800, may 2013.

[43] B. Wu, “Cfd simulation of gas and non-newtonian fluid two-phase flow in anaerobic digesters,” *Water Research*, vol. 44, no. 13, pp. 3861–3874, 2010.

[44] X. Frank and H. Z. Li, “Complex flow around a bubble rising in a non-newtonian fluid,” *Phys. Rev. E*, vol. 71, p. 036309, Mar 2005.

[45] J. Liu, C. Zhu, T. Fu, Y. Ma, and H. Li, “Numerical simulation of the interactions between three equal-interval parallel bubbles rising in non-newtonian fluids,” *Chemical Engineering Science*, vol. 93, pp. 55–66, 2013.

[46] S. Radl, G. Tryggvason, and J. G. Khinast, “Flow and mass transfer of fully resolved bubbles in non-Newtonian fluids,” *AIChE Journal*, vol. 53, no. 7, pp. 1861–1878, jul 2007.

[47] L. Zhang, C. Yang, and Z.-S. Mao, “Numerical simulation of a bubble rising in shear-thinning fluids,” *Journal of Non-Newtonian Fluid Mechanics*, vol. 165, no. 11-12, pp. 555–567, 2010.

[48] D. Rodrigue, “A simple correlation for gas bubbles rising in power-law fluids,” *The Canadian Journal of Chemical Engineering*, vol. 80, no. 2, pp. 289–292, apr 2002.

[49] M. Ohta, Y. Yoshida, and M. Sussman, “A computational study of the dynamic motion of a bubble rising in Carreau model fluids,” *Fluid Dynamics Research*, vol. 42, no. 2, p. 025501, 2010.

[50] M. Ohta, S. Kimura, T. Furukawa, Y. Yoshida, and M. Sussman, “Numerical Simulations of a Bubble Rising through a Shear-Thickening Fluid,” *Journal of Chemical Engineering of Japan*, vol. 45, no. 9, pp. 713–720, 2012.

[51] A. R. Premlata, M. K. Tripathi, B. Karri, and K. C. Sahu, “Numerical and experimental investigations of an air bubble rising in a carreau-yasuda shear-thinning liquid,” *Physics of Fluids*, vol. 29, no. 3, p. 033103, 2017.

[52] A. R. Premlata, M. K. Tripathi, B. Karri, and K. C. Sahu, “Dynamics of an air bubble rising in a non-newtonian liquid in the axisymmetric regime,” *Journal of Non-Newtonian Fluid Mechanics*, vol. 239, pp. 53–61, 2017.

[53] K. C. Sahu, “A review on rising bubble dynamics in viscosity-stratified fluids,” *Sādhanā*, vol. 42, no. 4, pp. 575–583, Apr 2017.

[54] A. R. Premlata, M. K. Tripathi, and K. C. Sahu, “Dynamics of rising bubble inside a viscosity-stratified medium,” *Physics of Fluids*, vol. 27, no. 7, p. 072105, 2015.

[55] M. K. Tripathi, K. C. Sahu, G. Karapetsas, and O. K. Matar, “Bubble rise dynamics in a viscoplastic material,” *Journal of Non-Newtonian Fluid Mechanics*, vol. 222, pp. 217 – 226, 2015.

[56] J. Tsamopoulos, Y. Dimakopoulos, N. Chatzidai, G. Karapetsas, and M. Pavlidis, “Steady bubble rise and deformation in newtonian and viscoplastic fluids and conditions for bubble entrapment,” *Journal of Fluid Mechanics*, vol. 601, p. 123–164, 2008.

[57] R. P. Chhabra, “Motion of spheres in power law (viscoinelastic) fluids at intermediate reynolds numbers: a unified approach,” *Chemical Engineering and Processing: Process Intensification*, vol. 28, no. 2, pp. 89 – 94, 1990.

[58] M. W. Baltussen, L. J. H. Seelen, J. A. M. Kuipers, and N. G. Deen, “Direct numerical simulations of gas-liquid-solid three phase flows,” *Chemical Engineering Science*, vol. 100, pp. 293–299, 2013.

[59] M. W. Baltussen, J. A. M. Kuipers, and N. G. Deen, “Direct numerical simulation of effective drag in dense gas-liquid-solid three-phase flows,” *Chemical Engineering Science*, vol. 158, pp. 561–568, 2017.

[60] I. Roghair, M. van Sint Annaland, and J. A. M. Kuipers, “An enhanced front tracking method featuring volume conservative remeshing and mass transfer,” *Progress in Applied CFD*, pp. 59–71, 2015.

[61] I. Roghair, M. van Sint Annaland, and J. A. M. Kuipers, “An improved Front-Tracking technique for the simulation of mass transfer in dense bubbly flows,” *Chemical Engineering Science*, vol. 152, pp. 351–369, 2016.

[62] W. Dijkhuizen, I. Roghair, M. van Sint Annaland, and J. A. M. Kuipers, “DNS of gas bubbles behaviour using an improved 3D front tracking model–Model development,” *Chem. Eng. Sci.*, vol. 65, no. 4, pp. 1427–1437, 2010.

[63] A. Kuprat, A. Khamayseh, D. George, and L. Larkey, “Volume conserving smoothing for piecewise linear curves, surfaces, and triple lines,” *J. Comp. Phys.*, vol. 172, pp. 99–118, 2001.

[64] R. B. Bird, W. E. Stewart, and E. N. Lightfoot, *Transport Phenomena*, revised 2n ed. New York: John Wiley & Sons, 2007.

[65] S. Gabbanelli, G. Drazer, and J. Koplik, “Lattice Boltzmann method for non-Newtonian (power-law) fluids,” *Physical Review E - Statistical, Nonlinear, and Soft Matter Physics*, vol. 72, no. 4, p. 046312, oct 2005.

[66] A. Prosperetti, “Navier-Stokes numerical algorithms for free-surface flow computations: an overview,” *Drop-surface interaction*, vol. 456, pp. 237–257, 2002.

[67] R. Mei, J. F. Klausner, and C. J. Lawrence, “A note on the history force on a spherical bubble at finite Reynolds number,” *Phys. Fluids*, vol. 6, no. 1, pp. 418–420, 1994.

[68] R. P. Chhabra, *Bubbles, Drops, and Particles in Non-Newtonian Fluids, Second Edition*, ser. Chemical Industries. CRC Press, 2006.

[69] B. C. H. Venneker, J. J. Derksen, and H. E. A. van den Akker, “Turbulent flow of shear-thinning liquids in stirred tanks–the effects of reynolds number and flow index,” *Chemical Engineering Research and Design*, vol. 88, no. 7, pp. 827–843, 2010.

[70] A. Battistella, J. P. M. Kooijman, I. Roghair, and M. van Sint Annaland, “Hybrid Front-Tracking and Discrete Bubble Model approach for bubbly flows with a free surface,” in preparation.

[71] N. G. Deen, “An experimental and computational study of fluid dynamics in gas-liquid chemical reactors,” Ph.D. dissertation, Aalborg University Esbjerg, 2001.

[72] P. Shi and R. Rzehak, “Solid-liquid flow in stirred tanks: Euler-euler/RANS modeling,” *Chemical Engineering Science*, vol. 227, p. 115875, 2020.

[73] V. Kannan, P. R. Naren, V. V. Buwa, and A. Dutta, “Effect of drag correlation and bubble-induced turbulence closure on the gas hold-up in a bubble column reactor,” *Journal of Chemical Technology & Biotechnology*, vol. 94, no. 9, pp. 2944–2954, 2019.

[74] L. Gemello, C. Plais, F. Augier, and D. L. Marchisio, “Population balance modelling of bubble columns under the heterogeneous flow regime,” *Chemical Engineering Journal*, vol. 372, pp. 590 – 604, 2019.

[75] C. L. Streett and M. G. Macaraeg, “Spectral multi-domain for large-scale fluid dynamic simulations,” *Applied Numerical Mathematics*, vol. 6, no. 1, pp. 123–139, 1989, special Issue on Spectral Multi-Domain Methods.

[76] K. W. Thompson, “Time-dependent boundary conditions for hyperbolic systems, II,” *Journal of Computational Physics*, vol. 89, no. 2, pp. 439–461, 1990.

[77] T. J. Poinsot and S. K. Lelef, “Boundary conditions for direct simulations of compressible viscous flows,” *Journal of Computational Physics*, vol. 101, no. 1, pp. 104–129, 1992.

[78] C. D. Pruett, T. A. Zang, C.-L. Chang, and M. H. Carpenter, “Spatial direct numerical simulation of high-speed boundary-layer flows part I: Algorithmic considerations and validation,” *Theoretical and Computational Fluid Dynamics*, vol. 7, pp. 49–76, 1995.

[79] D. Darmana, R. L. B. Henket, N. G. Deen, and J. A. M. Kuipers, “Detailed modelling of hydrodynamics, mass transfer and chemical reactions in a bubble column using a discrete bubble model: Chemisorption of CO2 into NaOH solution, numerical and experimental study,” *Chemical Engineering Science*, vol. 62, no. 9, pp. 2556–2575, 2007.

[80] C. W. Hirt and B. D. Nichols, “Volume of fluid (VOF) method for the dynamics of free boundaries,” *Journal of Computational Physics*, vol. 39, no. 1, pp. 201–225, 1981.

[81] A. Asad, C. Kratzsch, and R. Schwarze, “Influence of drag closures and inlet conditions on bubble dynamics and flow behavior inside a bubble column,” *Engineering Applications of Computational Fluid Mechanics*, vol. 11, no. 1, pp. 127–141, 2017.

[82] J. Klostermann, K. Schaake, and R. Schwarze, “Numerical simulation of a single rising bubble by VOF with surface compression,” *International Journal for Numerical Methods in Fluids*, vol. 71, no. 8, pp. 960–982, 2013.

[83] M. van Sint Annaland, N. G. Deen, and J. A. M. Kuipers, “Numerical simulation of gas bubbles behaviour using a three-dimensional volume of fluid method,” *Chemical Engineering Science*, vol. 60, no. 11, pp. 2999–3011, 2005.

[84] A. Battistella, S. S. C. Aelen, I. Roghair, and M. van Sint Annaland, “Euler-Lagrange modeling of bubbles formation in supersaturated water,” *ChemEngineering*, vol. 2, no. 3, 2018.

[85] A. W. Vreman, “An eddy-viscosity subgrid-scale model for turbulent shear flow: Algebraic theory and applications,” *Physics of Fluids*, vol. 16, no. 10, pp. 3670–3681, 2004.

[86] A. Tomiyama, H. Tamai, I. Zun, and S. Hosokawa, “Transverse migration of single bubbles in simple shear flows,” *Chemical Engineering Science*, vol. 57, no. 11, pp. 1849–1858, 2002.

[87] T. R. Auton, “The lift force on a spherical rotational flow,” *Journal of Fluid Mechanics*, vol. 183, pp. 199–218, 1987.

[88] A. Tomiyama, T. Matsuoka, T. Fukuda, and T. Sakaguchi, “A simple numerical method for solving an incompressible two-fluid model in a general curvilinear coordinate system,” in *Multiphase Flow 1995*, 1995, pp. 241–252.

[89] B. P. B. Hoomans, J. A. M. Kuipers, W. J. Briels, and W. P. M. van Swaaij, “Discrete particle simulation of bubble and slug formation in a two-dimensional gas-fluidised bed: A hard-sphere approach,” *Chemical Engineering Science*, vol. 51, no. 1, pp. 99–118, 1996.

[90] Y. Liao and D. Lucas, “A literature review of theoretical models for drop and bubble breakup in turbulent dispersions,” *Chemical Engineering Science*, vol. 64, no. 15, pp. 3389–3406, 2009.

[91] J. Centrella and J. R. Wilson, “Planar numerical cosmology. II - The difference equations and numerical tests,” *Astrophysical Journal Supplement Series*, vol. 54, pp. 229–249, 1984.

[92] S. Balay, S. Abhyankar, M. F. Adams, J. Brown, P. Brune, K. Buschelman, L. Dalcin, A. Dener, V. Eijkhout, W. D. Gropp, D. Karpeyev, D. Kaushik, M. G. Knepley, D. A. May, L. C. McInnes, R. T. Mills, T. Munson, K. Rupp, P. Sanan, B. F. Smith, S. Zampini, H. Zhang, and H. Zhang, “PETSc Web page,” https://www.mcs.anl.gov/petsc, 2019. [Online]. Available: https://www.mcs.anl.gov/petsc

[93] S. Balay, S. Abhyankar, M. F. Adams, J. Brown, P. Brune, K. Buschelman, L. Dalcin, A. Dener, V. Eijkhout, W. D. Gropp, D. Karpeyev, D. Kaushik, M. G. Knepley, D. A. May, L. C. McInnes, R. T. Mills, T. Munson, K. Rupp, P. Sanan, B. F. Smith, S. Zampini, H. Zhang, and H. Zhang, “PETSc users manual,” Argonne National Laboratory, Tech. Rep. ANL-95/11 - Revision 3.13, 2020. [Online]. Available: https://www.mcs.anl.gov/petsc

[94] S. Balay, W. D. Gropp, L. C. McInnes, and B. F. Smith, “Efficient management of parallelism in object oriented numerical software libraries,” in *Modern Software Tools in Scientific Computing*, E. Arge, A. M. Bruaset, and H. P. Langtangen, Eds. Birkhäuser Press, 1997, pp. 163–202.

[95] D. B. Holmes and J. R. Vermeulen, “Velocity profiles in ducts with rectangular cross sections,” *Chemical Engineering Science*, vol. 23, no. 7, pp. 717–722, 1968.

[96] U. Ghia, K. N. Ghia, and C. T. Shin, “High-Re solutions for incompressible flow using the Navier-Stokes equations and a multigrid method,” *Journal of Computational Physics*, vol. 48, no. 3, pp. 387–411, 1982.

[97] G. Liger-Belair, M. Vignes-Adler, C. Voisin, Bertrand Robillard, and P. Jeandet, "Kinetics of Gas Discharging in a Glass of Champagne: The Role of Nucleation Sites," *Langmuir*, vol. 18, no. 4, pp. 1294–1301, 2002.

[98] M. Amon and C. D. Denson, "A study of the dynamics of foam growth: Analysis of the growth of closely spaced spherical bubbles," *Polymer Engineering & Science*, vol. 24, no. 13, pp. 1026–1034, 1984.

[99] M. Pooladi-Darvish and A. Firoozabadi, "Solution-gas drive in heavy oil reservoirs," *Journal of Canadian Petroleum Technology*, vol. 38, no. 4, pp. 54–61, 1999.

[100] L. Liu, W. Cai, Y. Chen, and Y. Wang, "Fluid dynamics and mass transfer study of electrochemical oxidation by CFD prediction and experimental validation," *Industrial & Engineering Chemistry Research*, vol. 57, no. 18, pp. 6493–6504, 2018.

[101] W. A. El-Askary, I. M. Sakr, K. A. Ibrahim, and A. Balabel, "Hydrodynamics characteristics of hydrogen evolution process through electrolysis: Numerical and experimental studies," *Energy*, vol. 90, pp. 722 – 737, 2015.

[102] Z. Yang, X. F. Peng, and P. Ye, "Numerical and experimental investigation of two phase flow during boiling in a coiled tube," *International Journal of Heat and Mass Transfer*, vol. 51, no. 5, pp. 1003 – 1016, 2008.

[103] R. Zhuan and W. Wang, "Simulation on nucleate boiling in micro-channel," *International Journal of Heat and Mass Transfer*, vol. 53, no. 1, pp. 502 – 512, 2010.

[104] Z. L. Yang, T. N. Dinh, R. R. Nourgaliev, and B. R. Sehgal, "Numerical investigation of bubble coalescence characteristics under nucleate boiling condition by a lattice-boltzmann model," *International Journal of Thermal Sciences*, vol. 39, no. 1, pp. 1 – 17, 2000.

[105] J. H. Weijs, J. H. Snoeijer, and D. Lohse, "Formation of surface nanobubbles and the universality of their contact angles: A molecular dynamics approach," *Phys. Rev. Lett.*, vol. 108, p. 104501, Mar 2012.

[106] P. Mandin, J. Hamburger, S. Bessou, and G. Picard, "Modelling and calculation of the current density distribution evolution at vertical gas-evolving electrodes," *Electrochimica Acta*, vol. 51, no. 6, pp. 1140 – 1156, 2005.

[107] T. Nierhaus, H. van Parys, S. Dehaeck, J. van Beeck, H. Deconinck, J. Deconinck, and A. Hubin, "Simulation of the two-phase flow hydrodynamics in an IRDE reactor," *Journal of The Electrochemical Society*, vol. 156, no. 9, pp. P139–P148, 2009.

[108] H. van Parys, S. van Damme, P. Maciel, T. Nierhaus, F. Tomasoni, A. Hubin, H. Deconinck, and J. Deconinck, "Eulerian-lagrangian model for gas-evolving processes based on supersaturation," *WIT Transactions on Engineering Sciences*, vol. 65, pp. 109 – 118, 2009.

[109] S. van Damme, P. Maciel, H. ban Parys, J. Deconinck, A. Hubin, and H. Deconinck, “Bubble nucleation algorithm for the simulation of gas evolving electrodes,” *Electrochemistry Communications*, vol. 12, no. 5, pp. 664 – 667, 2010.

[110] R. Hreiz, L. Abdelouahed, D. Fünfschilling, and F. Lapicque, “Electrogenerated bubbles induced convection in narrow vertical cells: PIV measurements and euler–lagrange CFD simulation,” *Chemical Engineering Science*, vol. 134, pp. 138 – 152, 2015.

[111] D. Jain, N. G. Deen, and J. A. M. Kuipers, “Numerical modeling of carbon dioxide chemisorption in sodium hydroxide solution in a micro-structured bubble column,” *Chem. Eng. Sci.*, vol. 137, pp. 685–696, 2015.

[112] D. Legendre and R. Zevenhoven, “A numerical euler–lagrange method for bubble tower CO2 dissolution modeling,” *Chemical Engineering Research and Design*, vol. 111, pp. 49 – 62, 2016.

[113] S. Mer, O. Praud, H. Neau, N. Merigoux, J. Magnaudet, and V. Roig, “The emptying of a bottle as a test case for assessing interfacial momentum exchange models for euler–euler simulations of multi-scale gas-liquid flows,” *International Journal of Multiphase Flow*, vol. 106, pp. 109 – 124, 2018.

[114] J. Magnaudet and I. Eames, “The motion of high-reynolds-number bubbles in inhomogeneous flows,” *Annual Review of Fluid Mechanics*, vol. 32, no. 1, pp. 659–708, 2000.

[115] M. J. Prince and H. W. Blanch, “Bubble coalescence and break-up in air-sparged bubble columns,” *AIChE Journal*, vol. 36, no. 10, pp. 1485–1499, 1990.

[116] A. Ogata and R. B. Banks, “A solution of the differential equation of longitudinal dispersion in porous media,” Tech. Rep., 1961.

[117] O. R. Enríquez, C. Hummelink, G.-W. Bruggert, D. Lohse, A. Prosperetti, D. van der Meer, and C. Sun, “Growing bubbles in a slightly supersaturated liquid solution,” *Review of Scientific Instruments*, vol. 84, p. 065111, may 2013.

[118] S. F. Jones, G. M. Evans, and K. P. Galvin, “Bubble nucleation from gas cavities - a review,” *Advances in Colloid and Interface Science*, vol. 80, no. 1, pp. 27–50, 1999.

[119] S. G. Bankoff, “Entrapment of gas in the spreading of a liquid over a rough surface,” *AIChE Journal*, vol. 4, no. 1, pp. 24–26, March 1958.

[120] W. Tong, A. Bar-Cohen, T. Simons, and S. You, “Contact angle effects on boiling incipience of highly-wetting liquids,” *International Journal of Heat and Mass Transfer*, vol. 33, no. 1, pp. 91–103, January 1990.

[121] W. Fritz, “Maximum volume of vapor bubbles,” *Physikalische Zeitschrift*, 1935.

[122] H. Mirsandi, W. J. Smit, G. Kong, M. W. Baltussen, E. A. J. F. Peters, and J. A. M. Kuipers, “Bubble formation from an orifice in liquid cross-flow,” *Chemical Engineering Journal*, vol. 386, p. 120902, 2020.

[123] A. Moreno Soto, A. Prosperetti, D. Lohse, and D. van der Meer, "Gas depletion through single gas bubble diffusive growth and its effect on subsequent bubbles," *Journal of Fluid Mechanics*, vol. 831, p. 474–490, 2017.

[124] O. R. Enríquez, C. Sun, D. Lohse, A. Prosperetti, and D. van der Meer, "The quasi-static growth of CO2 bubbles," *Journal of Fluid Mechanics*, vol. 741, 2014.

[125] A. Battistella, I. Roghair, and M. van Sint Annaland, "Experimental study of CO_2 bubble formation on a surface in supersaturated water," in preparation.

[126] P. S. Epstein and M. S. Plesset, "On the stability of gas bubbles in liquid-gas solutions," *The Journal of Chemical Physics*, vol. 18, no. 11, pp. 1505–1509, 1950.

[127] O. R. Enríquez, C. Hummelink, G.-W. Bruggert, D. Lohse, A. Prosperetti, D. van der Meer, and C. Sun, "Growing bubbles in a slightly supersaturated liquid solution," *Review of Scientific Instruments*, vol. 84, no. 065111, 2013.

[128] G. S. Barker, B. Jefferson, and S. J. Judd, "The control of bubble size in carbonated beverages," *Chemical Engineering Science*, vol. 57, no. 4, p. 565 – 573, February 2002.

[129] X. Frank, N. Dietrich, J. Wu, R. Barraud, and H. Z. Li, "Bubble nucleation and growth in fluids," *Chemical Engineering Science*, vol. 62, no. 24, pp. 7090–7097, 2007, 8th International Conference on Gas-Liquid and Gas-Liquid-Solid Reactor Engineering.

[130] E. Dietrich, S. Wildeman, C. W. Visser, K. Hofhuis, E. S. Kooij, H. J. W. Zandvliet, and D. Lohse, "Role of natural convection in the dissolution of sessile droplets," *Journal of Fluid Mechanics*, vol. 794, p. 45–67, 2016.

[131] P. van der Linde, P. Peñas-López, l. Moreno Soto, D. van der Meer, D. Lohse, H. Gardeniers, and D. Fernández Rivas, "Gas bubble evolution on microstructured silicon substrates," *Energy Environ. Sci.*, vol. 11, pp. 3452–3462, 2018.

[132] S. Lubetkin and M. Blackwell, "The nucleation of bubbles in supersaturated solutions," *Journal of Colloid and Interface Science*, vol. 126, no. 2, pp. 610–615, 1988.

[133] G. Van Rossum and F. L. Drake, *Python 3 Reference Manual.* Scotts Valley, CA: CreateSpace, 2009.

[134] C. R. Harris, K. J. Millman, S. J. der Walt, R. Gommers, P. Virtanen, D. Cournapeau, E. Wieser, J. Taylor, S. Berg, N. J. Smith, R. Kern, M. Picus, S. Hoyer, M. H. van Kerkwijk, M. Brett, A. Haldane, J. F. del R'ıo, M. Wiebe, P. Peterson, P. G'erard-Marchant, K. Sheppard, T. Reddy, W. Weckesser, H. Abbasi, C. Gohlke, and T. E. Oliphant, "Array programming with NumPy," *Nature*, vol. 585, no. 7825, pp. 357–362, Sep. 2020.

[135] G. Bradski, "The OpenCV Library," *Dr. Dobb's Journal of Software Tools*, 2000.

[136] S. van der Walt, J. L. Schönberger, J. Nunez-Iglesias, F. Boulogne, J. D. Warner, N. Yager, E. Gouillart, T. Yu, and the scikit-image contributors, "scikit-image: image processing in Python," *PeerJ*, vol. 2, p. e453, 6 2014.

[137] J. Canny, “A computational approach to edge detection,” *IEEE Transactions on Pattern Analysis and Machine Intelligence*, vol. PAMI-8, no. 6, pp. 679–698, 1986.

[138] H. Yuen, J. Princen, J. Illingworth, and J. Kittler, “Comparative study of hough transform methods for circle finding,” *Image and Vision Computing*, vol. 8, no. 1, pp. 71–77, 1990.

[139] A. Buffo, D. L. Marchisio, M. Vanni, and P. Renze, “Simulation of polydisperse multiphase systems using population balances and example application to bubbly flows,” *Chemical Engineering Research and Design*, vol. 91, no. 10, pp. 1859–1875, 2013, the 60th Anniversary of the European Federation of Chemical Engineering (EFCE).

[140] S. Falzone, A. Buffo, M. Vanni, and D. L. Marchisio, “Chapter three - simulation of turbulent coalescence and breakage of bubbles and droplets in the presence of surfactants, salts, and contaminants,” in *Bridging Scales in Modelling and Simulation of Non-Reacting and Reacting Flows. Part I*, ser. Advances in Chemical Engineering, A. Parente and J. De Wilde, Eds. Academic Press, 2018, vol. 52, pp. 125–188.

LIST OF PUBLICATIONS

Journal publications

Battistella, A., Aelen, S.S.C., Roghair, I., van Sint Annaland, M. (2018). Euler–Lagrange modeling of bubbles formation in supersaturated water. *ChemEngineering*, 2(3), 39.

Battistella, A., van Schijndel, S.J.G., Baltussen, M.W, Roghair, I., van Sint Annaland, M. (2020). On the terminal velocity of single bubbles rising in non-Newtonian power-law liquids. *Journal of Non-Newtonian Fluid Mechanics*, 278, 104249.

Battistella, A., Kooijman, J.P.M., Roghair, I., van Sint Annaland, M. (2020). Hybrid Front-Tracking and Discrete Bubble Model approach for bubbly flows with a free surface. *Manuscript in preparation*.

Battistella, A., Roghair, I., van Sint Annaland, M. (2020). Experimental study of CO_2 bubble formation on a surface in supersaturated water. *Manuscript in preparation*.

Conference proceedings

Battistella, A., Aelen, S.S.C., Roghair, I., van Sint Annaland, M. (2017). Large scale modelling of bubble formation and growth in a supersaturated liquid. 12th International Conference on CFD in Oil&Gas, Metallurgical and Process Industries (CFD2017), Trondheim, Norway.

Battistella, A., van Schijndel, S.J.G., Roghair, I., van Sint Annaland, M. (2017). Front-Tracking simulations of bubbles in non-Newtonian fluids. 12th International Conference on CFD in Oil&Gas, Metallurgical and Process Industries (CFD2017), Trondheim, Norway.

Oral & poster presentations

Battistella, A., Roghair, I., van Sint Annaland, M. Multi-scale modeling of bubble coalescence and breakup in heterogeneous bubbly flows. ICMF2016, 22-27 May 2016, Florence, Italy. Oral presentation.

Battistella, A., Roghair, I., van Sint Annaland, M. Large scale CFD modelling of dense bubbly flows. AkzoNobel symposium on Frontiers in Chlorate and Chlor-Alkali Research, 4-5 April 2017, Bordeaux, France. Oral presentation.

Battistella, A., Aelen, S.S.C., Roghair, I., van Sint Annaland, M. Large scale modelling of bubble formation and growth in a supersaturated liquid. CFD2017, 30 May - 1 June 2017, Trondheim, Norway. Oral presentation.

Battistella, A., van Schijndel, S.J.G., Roghair, I., van Sint Annaland, M. Front-Tracking simulations of bubbles in non-Newtonian fluids. CFD2017, 30 May - 1 June 2017, Trondheim, Norway. Oral presentation.

Battistella, A., Aelen, S.S.C., Roghair, I., van Sint Annaland, M. Experimental and numerical study of bubble formation in supersaturated liquids. ISCRE25, 20-23 May 2018, Florence, Italy. Poster presentation.

Battistella, A., Aelen, S.S.C., Roghair, I., van Sint Annaland, M. CFD modeling of bubbly flows: a multi-scale approach. NPS15, 30-31 May 2018, Enschede, the Netherlands. Oral presentation.

Battistella, A., Aelen, S.S.C., Roghair, I., van Sint Annaland, M. Meso-scale simulations of bubble nucleation. Burgers symposium, 5-6 June 2018, Lunteren, the Netherlands. Oral presentation.

Battistella, A., Aelen, S.S.C., Roghair, I., van Sint Annaland, M. Numerical And Experimental Study Of Bubble Formation In Supersaturated Water. CFD2018, 4-7 December 2018, Melbourne, Australia. Oral presentation.

Battistella, A., Kooijman, J.P.M., Roghair, I., van Sint Annaland, M. Front Tracking Of The Free Surface In An Euler-Lagrange Gas-Liquid Model. CFD2018, 4-7 December 2018, Melbourne, Australia. Oral presentation.

Battistella, A., Kooijman, J.P.M., Roghair, I., van Sint Annaland, M. Modeling of the free surface of a Euler-Lagrange gas-liquid model with Front-Tracking. Burgers symposium, 21-22 May 2019, Lunteren, the Netherlands. Oral presentation.

Battistella, A., Aelen, S.S.C., Roghair, I., van Sint Annaland, M. Experimental and Numerical Analysis of CO2 Bubbles Formation in Water. GLS-14, 30 May - 3 June 2019, Guilin, China. Oral presentation.

Battistella, A., Roghair, I., van Sint Annaland, M. Towards large-scale simulations of an industrial fermentor using a Discrete Bubble Model. CFD2020, 12-14 October 2020, Trondheim, Norway. Oral presentation.

ACKNOWLEDGMENTS

An important part of my life has come to an end. While I am glad it is finally over and ended up in this thesis, I cannot stop thinking about all I have learnt and about how much I have grown during this long, difficult, beautiful path called PhD. The negative and positive moments, the enormous stress, the fun times, the many conferences and the strong personal bonds I tied are and will remain part of me forever.

I want to start with thanking my promotor, prof.dr.ir. Martin van Sint Annaland. Martin, I have met you during my MSc thesis and when I thought about doing a PhD, your group was where I wanted to be. I am glad you granted me the opportunity to do this research in the SPI Group. I learnt a lot from you: you are a very precise, methodic, thorough scientist and your attention for details is always incredible. I actually had to learn how to tune it down sometimes, or we could have continued working on this thesis longer than it took! Jokes aside, I admire your dedication and I am grateful for all the help you gave me (especially correcting my Itanglish) throughout these 6 years. I am also very proud that you asked me to teach you something, during our C++ crash course! Thanks a lot for everything and I wish you all the best with the future endeavors of the SPI group.

I would like to also express my gratitude to my daily supervisor and copromotor dr.ir Ivo Roghair. Ivo, thanks a lot for all the bubble related talks. You have a deep knowledge about bubbles especially when it comes to DNS, and I think we both learnt a lot together regarding higher scales (and sparkling water modeling). I not only appreciate you on the bubble side, but it has been fun to work with you and discuss all the nerd computer/Linux related topics. I enjoyed also your way of teaching Numerical Methods. I will always remember your classes, preparing fun assignments and especially the correction of student reports. Thanks for everything!

This project was originally funded by FOM, later rearranged as NWO-I. I would like to thank all the parties involved for the interesting discussions and useful comments at our IPP meetings. Thanks in particular to the industrial partners representatives: Bert Vreman (Nouryon), Dirk van der Plas (Tata Steel), Patrick Wenmakers (DSM), Christoph Dittrich (SABIC) and Peter Veenstra (Shell).

I am grateful to the members of my doctorate committee for accepting to be part of my defense and for taking the time to read and evaluate this dissertation. In particular, thanks to dr.ir. Cees Haringa for hosting me in DSM and to prof.dr. Daniele Marchisio for hosting us (and Maurits) in Torino and for the collaboration.

I would also like to thank the staff members of SMR. Ada and Judith, thanks for all your invaluable help on administrative matters, especially regarding the many students I had. Joost, Herbert, Thijs and Joris, thank you for your help with the bubble nucleation setup. Being myself very inexperienced with experimental setups, you greatly helped me and I appreciate the enormous support you gave me and my students. And I loved the technicians stories and fun moments at the coffee breaks.

The results published in this thesis could not be achieved without the help of the (many) students I had the pleasure to supervise and work with. In particular, I would like to thank Sander, Sebastian, Maarten and Maurits for their MSc thesis work, your contribution to this book has been crucial. Many other projects played an important role as well: Stan, Valen, Claire, Huib, Germain, Mathilde, Zançat, Hendrik, Robbert, Irian, Eline, Egbert and Fabio, thank you, I enjoyed working with all of you!

During my long stay at the TU/e I have met an incredible number of amazing people. I would first like to start with my two office mates. Ramon, you are the most pessimistic, inappropriate and politically incorrect person I know. Yet, I enjoyed every moment you spent with us in the office (and outside)! All the darts (and stupid flash games), the Barcelona trip, the London trip: we had awesome times together, mate. All the best to you, Ninchelle and the little Natalia. Milan, brate moj. You are the chill one, and I guess you had to cope with my talking sometimes. Thanks for all the fun nights, the US trip, the craziness and the deep conversations, your music/movies taste and most of all: the basketball. Your step back has costed me the 2019 STO 1.28 champion title! And my AJs will be haunting you for long. All in all, I could have not had better office mates than you two.

I would like to thank as well all the other friends I made during these years. First of all, a big thank you to the Musketeers. Dario and Francesco, especially during the last couple of years you have been my Italian family in Eindhoven, and that's the reason why you are my paranymphs. Francesco, thanks for all the jokes and also for the serious talks. And especially for your BBQs: you know meat handling like no others. Dario, I enjoyed your company even in a 12 hours trip in a FIAT 500. Multiple times. You are a source of incredible stories, knowledge, science, technology and inappropriate jokes. Brossein, if my heart is an apartment, you know where you are. I am looking forward for your move to Breda! Aitor, I will never forget the Vietnam trip, your sport skills and your Italian skills. And of course, thanks also to the ladies: ML, Valeria, Carmen and Sarah. I survived the pandemic times thanks to all of you (and Bang).

Thanks also to the FIFA nights crew (85C forever in our hearts). Rohit, Vinay, Vishak and Ketemaw thanks for the memorable nights, the fun moments and the serious conversations. Solo, you are an incredible person, yet you cannot lose at FIFA. Thanks for your depth and for coping with my bad jokes. And I wish you and your lovely family all the best. Aditya you are the most brilliant person I know. Thanks for the trips (US above all) and the long deep philosophical discussions. And all the best to you and Medha in your future life.

There are more and more people I would like to thank for being part of my PhD path: Giulia and Maria (grazie per le lunghe chiacchierate, gli sfoghi e tanto gossip); Tim and Evan, my dutch bros and nerd neighbors, also thanks for the trips (Tim, I will never forget Australia, you know why); the serbian gang Ivan and Vladan; the others of the great indian community with Aniruddha, Harshil, Adnan, Satish and Shauvik; the "new guys" Morteza, Leon, Marve and Arvin; the "old guys" Vincenzo, José, Alvaro, Mohammad, Arash H.; and a lot more people including Alexei, Niek, Alba, Nerea, Arash R., Haryo, Max, Maike, Salvatore and others whom I am surely forgetting in this list. A special mention goes to the crazy Erasmus

students generation of 2018, thanks in particular to Luca, Jessica, Francesco Destro, Mikel and Marta.

Me ne andai dall'Italia nel 2012, e molti contatti sono andati persi. Voglio ringraziare una persona in particolare per esserci sempre stata: Bomber, Andre, grazie per tutto il supporto di questi anni e perché ogni volta che ci vediamo e sentiamo é come se ci fossimo parlati il giorno prima. Anche se ci rispondiamo ai messaggi vocali dopo giorni, e se pure il COVID ti ha impedito di venirmi a trovare, grazie di cuore.

Voglio anche ringraziare la mia "seconda famiglia": Caterina, Mauri, Anna, Anita e Gennaro, Mario e Luigino. Grazie di avermi accolto nella famiglia Sgarbossa ed esserci sempre. Siete tutti speciali.

Non sarei la persona che sono adesso senza la presenza, gli insegnamenti e l'affetto della mia famiglia. In tutti questi anni abbiamo avuto alti e bassi, ma voi siete sempre stati al mio fianco e mi avete **sempre** supportato. Zio Massimo, sei la mia ispirazione e, anche se non ho scelto medicina o continuato come professore, sei sempre stato il mio primo motivatore assoluto. E ora possiamo fregiarci del titolo di "Dottore" in due! Un ringraziamento speciale a tutti i miei nonni, anche quelli che non ci sono piú. So che siete tutti fieri di me, e mancate tanto. Barbara, vederti crescere e sbocciare nella bellissima persona che sei adesso mi riempie di gioia. Sono orgoglioso di te. Rimarrai sempre la mia sorellina, e ti auguro tutto il meglio nella tua nuova casetta con Andrea. Mamma e papá, siete e sarete sempre il mio esempio di vita. Mi avete sempre appoggiato e aiutato in ogni decisione, compresa quella di trasferirmi in Olanda, e per questo vi ringrazieró sempre. Mamma, nonostante i nostri caratteracci, mi hai insegnato ad esigere sempre il meglio da me stesso e a non accontentarmi, mai. Papá, mi hai trasmesso la tua tenacia e perseveranza e mi hai insegnato l'onestá. Sei di una forza incredibile e questa tesi é dedicata a te.

E last but not least: Francesca, quando ti ho conosciuta ho capito che sei la mia persona. Mi hai supportato (e sopportato) nei miei momenti piú bui, sei sempre stata al mio fianco, e mi hai dato piú di una spinta per finire questa tesi. Sei una persona meravigliosa e sono felice di aver cominciato questa nuova avventura a Terneuzen assieme a te. E come dimenticare la nostra Stella, la vera principessa del castello! Siete la mia famiglia e non potrei desiderare miglior compagnia in questa straordinaria esperienza che é la vita, dovunque ci porterá.

Alessandro Battistella,
Terneuzen, November 2021.

BIOGRAPHY

Alessandro Battistella was born on the 22nd of April 1990 in Merate, Italy. He completed his high school at the Liceo Scientifico Tecnologico Albert Einstein in Vimercate, Italy, in June 2009. In September 2009, he entered the Bachelor in Chemical Engineering program at the Politecnico di Milano, which he completed in September 2012. Right after, he decided to move to the Eindhoven University of Technology, where he started his MSc program in Chemical Engineering, successfully defending his Master's thesis titled "Membrane Assisted Chemical Looping Reforming process modeling for H2 production" in October 2014. As part of the MSc program, he joined a six month internship at SABIC in Geleen, performing kinetic modeling for a process aimed at LPG and BTX production. In 2015 he concluded his internship and obtained the MSc title with classification "with great appreciation".

In September 2015 Alessandro started his PhD project under the guidance of Prof.Dr.ir. Martin van Sint Annaland and Dr.ir. Ivo Roghair in the Chemical Process Intensification group at the Eindhoven University of Technology. His work was part of the Industrial Partnership Programme i36 Dense Bubbly Flows that is carried out under an agreement between AkzoNobel (now Nouryon), DSM, SABIC, Shell and Tata Steel and the Netherlands Organisation for Scientific Research (NWO). The results of this research are presented in this dissertation.

After his PhD, Alessandro worked until December 2020 as a researcher within the same group at the University of Eindhoven, developing a Discrete Particle Model in C++. Currently, Alessandro holds the position of Senior R&D Engineering Specialist at Dow Chemicals in Terneuzen, the Netherlands.